Electromagnetically Induced Transparency in Optically Trapped Rubidium Atoms

Von der Fakultät Mathematik und Physik der Universität Stuttgart
zur Erlangung der Würde eines Doktors der
Naturwissenschaften (Dr. rer. nat.) genehmigte Abhandlung

Vorgelegt von

Bernd Kaltenhäuser

aus Göppingen

Hauptberichter:	Prof. Dr. Tilman Pfau
Mitberichter:	Prof. Dr. Atac Imamoğlu
Tag der mündlichen Prüfung:	12.04.2007

5. Physikalisches Institut der Universität Stuttgart

2007

Abstract

Within the scope of this work an experiment to cool rubidium atoms down to temperatures in the μK region has been set up. The final goal of this experiment is to use this ultracold rubidium cloud as a high efficiency detector for single photons. This detector will be an important part of a quantum computer, that uses single photons as information carriers [KLM01]. Once the ultracold rubidium cloud reaches the ideal parameters in temperature, density and atom number, the single photons are sent into the atomic cloud, in which they will modify the state of exactly one atom per incident photon. Together with the single photons, a so-called coupling laser will be sent into the atomic cloud to ensure an efficient modification of the atoms. This modification of the atoms will be detected afterwards by fluorescence imaging.

The experimental setup has been used to perform measurements on electromagnetically induced transparency (EIT), an effect that makes otherwise opaque matter transparent to light. This effect can also be used to reduce the group velocity of light.

The main parts of the experimental setup are a vacuum chamber, magnetic coils and several laser systems. The vacuum chamber consists of the main chamber, where the atoms are first evaporated from rubidium dispensers, afterwards trapped magneto-optically and subsequently optically in a dipole laser trap, and a pumping area, where the ultra high vacuum is produced. Several magnetic coils are put around the chamber to produce the required magnetic fields.
The laser system that produces the light to trap and cool the atoms consists of three diode lasers and one tapered amplifier, which are running at a wavelength of 780 nm. A Raman laser system that consists of three diode lasers, running at 795 nm, produces the probe light (that will be used as single photon source) as well as the coupling light.
Furthermore, a CO_2-laser, running at a wavelength of 10.6 μm, produces up to 130 W optical power, which is used to capture the atoms in the dipole trap.

Abstract

In this work, a description of the setup of the vacuum chamber, the magnetic coils and the laser systems will be given.
Furthermore, calculations on single photon detection and measurements on the atomic cloud will be presented. Finally, measurements with the Raman laser system on EIT will be shown.

Up to $1.7 \cdot 10^9$ atoms were captured in the MOT, while about 2 % of them have been transferred into the optical dipole trap.
Using the Raman laser system, EIT has been measured in optically trapped rubidium atoms for the first time. Here, with 4 kHz, the so far narrowest EIT bandwidth in ultracold atoms has been achieved.

Zusammenfassung

Im Rahmen dieser Arbeit wurde ein Experiment zur Kühlung von Rubidiumatomen bis in den μK-Bereich aufgebaut. Das Ziel dieses Experiments ist die Verwendung dieser ultrakalten Atomwolke zur Detektion von Einzelphotonen. Dieser Detektor stellt einen wichtigen Bestandteil eines Quantencomputers dar, der Einzelphotonen als Informationsträger nutzt [KLM01]. Sobald die ultrakalte Atomwolke die idealen Parameter in Temperatur, Dichte und Atomzahl erreicht, werden die Einzelphotonen in die Wolke geschossen, wo sie den Zustand eines Atoms pro eintreffendem Photon verändern. Ein sogenannter Koppellaser wird zusammen mit den Einzelphotonen auf die Wolke geschossen. Dieser sichert eine effiziente Veränderung des atomaren Zustands. Diese Veränderung wird anschließend durch Fluorenszenz detektiert.

Der Aufbau wurde genutzt um Messungen zur elektromagnetisch induzierten Transparenz (EIT), einem Effekt der optisch trübe Materie transparent macht, durchzuführen. Dieser Effekt kann auch genutzt werden, um die Gruppengeschwindigkeit von Licht zu reduzieren.

Die Hauptbestandteile des Experiments sind eine Vakuumkammer, Magnetspulen und mehrere Lasersysteme. Die Vakuumkammer besteht aus einer Hauptkammer, in der die Atome zuerst von Rubidiumdispensern verdampft, dann magneto-optisch und anschließend in einer optischen Dipolfalle gefangen werden, und einem Pumpkreuz, in dem das Ultrahochvakuum erzeugt wird. Mehrere Magnetspulen befinden sich an der Kammer um die erforderlichen Magnetfelder zu erzeugen.

Das Lasersystem, mit dessen Licht die Atome gefangen und gekühlt werden, besteht aus drei Diodenlasern und einem Tapered Amplifier, welche auf einer Wellenlänge von 780 nm laufen. Ein Ramanlasersystem, das aus drei Diodenlasern besteht, welche auf 795 nm laufen, erzeugt sowohl das Licht des Probelasers (welches später als Einzelphotonenquelle benutzt wird) als auch das Licht des Koppellasers.

Des weiteren erzeugt ein CO_2-laser bei einer Wellenlänge von $10.6\,\mu$m bis zu 130 W optische Leistung, welche genutzt wird, um die Atome in einer Dipolfalle zu fangen.

Diese Arbeit enthält eine Beschreibung der Vakuumkammer, der Magnetspulen und der Lasersysteme. Es werden sowohl Messungen zur Atomwolke selbst, als auch Messungen mit dem Ramanlasersystem zur EIT gezeigt.

Bis zu $1.7 \cdot 10^9$ Atome wurden in der MOT gefangen, von denen etwa 2 % in die optische Dipolfalle transferiert wurden. Mit Hilfe des Ramanlasersystems wurde EIT zum ersten Mal in optisch gefangenen Atomen demonstriert. Dabei wurde mit 4 kHz die bisher schmalste EIT Linienbreite in ultrakalten Atomen erreicht.

Eine umfassende Zusammenfassung dieser Arbeit in deutscher Sprache findet sich in Anhang F.

Contents

1. Introduction

1.1 Recent developments leading to this project

Within the last 20 years, great progress was made in the field of atom- and quantum optics. Three of the recent developments in this field are combined to fulfill the goal of this experiment: to build a high efficiency single photon counter. These three developments will be briefly reviewed:

1. Laser cooling
The most popular of these developments were the techniques of laser cooling: in so-called magneto-optical traps, neutral atoms are cooled and trapped at the same time, which was first demonstrated by Steven Chu in 1986 [RPC$^+$87].
This atom trap is able to capture relatively fast atoms and is thus used as the first trap in a trapping sequence, consisting of several traps, being applied after each other. Because the lowest temperature achievable in this kind of trap is in the $10\,\mu$K region, the cold atoms are often transferred into another trap afterwards.
Another method to trap atoms is the optical dipole trap, which uses strong lasers and a tight focus to capture the atoms in a conservative potential. It was also realized for the first time in 1986 by Steven Chu [CBAC86].

2. EIT and STIRAP
Independently from the progress in laser cooling, Harris and co-workers examined a new effect of light-matter-interaction in three-level systems, which is called electromagnetically induced transparency (EIT) in 1989 [HFI90]. This effect shows a complete absence of laser light absorption when a second laser beam, which is resonant on a second transition of the medium, is applied. Furthermore, this effect is accompanied by a greatly enhanced non-linear susceptibility. This gives rise to many further effects as e.g. the slowing and stopping of light. In ultracold atoms, this has first been demonstrated by Hau and co-workers [HHDB99].

The group of Klaas Bergmann investigated EIT in a different way by the usage of molecular beams instead of confined atoms [BTS98]. The movement of the molecules through the Gaussian shaped lasers adds a time-dependence to the intensity of the light-matter-interaction (described by the Rabi-frequency). This leads to a transfer of the photonic state to an internal state of the medium. Because the light-matter-state follows the change in the Rabi-frequency, this effect is called stimulated Raman adiabatic passage (STIRAP). Meanwhile, this effect has also been demonstrated in atoms, where the moving frame of the molecules has been replaced by modulating the laser-intensities adequately.
Liu and co-workers have demonstrated the successful combination of laser cooling with EIT and STIRAP in one experiment [HHDB99, LDBH01].

3. Theory on quantum computation and photon detectors
In 2001, Knill, LaFlamme and Milburn proposed a new quantum computation scheme that uses single photons as information carriers [KLM01]. Such a quantum computer requires only linear optical parts like beam splitters, which makes it very robust against perturbations. The downside of this simple scheme is the necessity of high efficiency single photon sources and counters, which are not yet available. However, lots of research has been performed on high efficiency single photon sources within the last years [KHBR99, MKB$^+$00], but high efficiency single photon counters have not been realized.
In 2002, Atac Imamoğlu [Ima02] and independently James and Kwiat [JK02] proposed that the transfer of light onto an atomic state can be used to build a single photon detector, that has a detection efficiency of more than 99 %. Furthermore, such a detector is able to distinguish between photon number states up to $n \approx 50$.
Besides quantum computation, such a detector can also be used for high efficiency quantum communication [BEKW02, CMJ$^+$06] or a loophole-free test of Bell's inequalities [ADR82].

The detector of Imamoğlu combines the three developments described above in one experiment and is currently being set up at the 5th Institute of Physics at the Universität Stuttgart.
The goal of the experimental setup described in this thesis is the realization of such a high efficiency photon counter.

1.2 Scheme of the experiment

The idea is to capture a cloud of ultracold atoms. Then, together with a coupling laser, the single photons, that shall be counted, are sent into the chamber. The coupling laser ensures that each single photon transfers an atom into a defined state. The transferred atoms are subsequently detected by fluorescence imaging.

As this scheme is very sensitive to polarization, a well defined magnetization axis is needed. This can only be provided by a high and homogeneous magnetic offset field. The only atom trap that can be combined with such a magnetic field is a dipole laser trap, which thus has to be used in the experiment.

As the atoms, which have not been transferred by a single photon also scatter detection light and therefore spoil the detection process, they have to be removed from the trap before the detection. This can be done by applying a strong magnetic gradient, pulling out all atoms, which have been collected in a magnetically sensitive state, while it leaves the atoms, which have been transferred by the single photons to a magnetically neutral state, in the trap for detection.

Finally, the whole detection scheme reads:

1. Atomic cooling
The first step is to capture ultracold rubidium atoms in a ultrahigh vacuum chamber. The atoms are first trapped and cooled in a magneto-optical trap (MOT) before they are transferred into an optical dipole trap, where they are further cooled down and prepared in a defined substate.

2. Adiabatic transfer
Subsequently, the single photons are sent into the cloud. They are accompanied by a coupling laser, which ensures that each single photon transfers one atom into a defined state. Hereby, the laser intensities perform the STIRAP sequence.

3. Removal of unwanted atoms
After this transfer, the atoms that have not been transferred will be removed from the trap by applying a strong magnetic field gradient.

4. The detection process
Then, the transferred atoms will be counted by fluorescence detection.

1.2.1 The idea

Compared to the scheme described above, the initial idea [Ima02] was to capture the ultracold rubidium atoms in a magnetic trap. As will be shown in the next sections, the single photon transfer is very sensitive to the polarizations of the single photons and the coupling laser and a wrong polarization would cause a decrease of the detection efficiency. The polarization purity that can be achieved with polarizing beamsplitter cubes and λ-plates is on the order of 1 ‰ [BHN07], which is sufficient for the proposed experimental scheme. But likewise, the definition of the quantization axis, which is obtained from the magnetic field, must be that pure as well. Because the direction of the magnetic field in a magnetic trap is not homogeneous, there is no quantization axis that is parallel to the wave vector of the light (over the whole size of the cloud) and thus this kind of trap cannot be used.
Additionally, there are always stray fields. These vary from day to day and thus their compensation shielding is extremely complicated if at all fully possible. Hence, a high magnetic offset field is required because here the influence of the stray fields onto the total field is minimized. This high offset field is another reason why a magnetic trap is not suitable, as the confinement in magnetic traps decreases for increasing offset fields [Pri83].

1.2.2 Atomic cooling

The solution is to use an optical dipole trap after the MOT loading phase. This trap creates the confinement of the atoms and an additional high magnetic offset field creates a well defined direction of the quantization axis with respect to the wave vector of the light. In this trap, the atoms are cooled to a very low temperature of $\sim 750\,\mathrm{nK}$ by evaporative cooling. At this point, the density and temperature are just above the critical parameters required for achieving a Bose-Einstein-Condensate (BEC).
Dipole traps can be easily realized at wavelengths around 1064 nm, as this light traverses common optical viewports of vacuum chambers. This light is strongly detuned from the D1 and D2 transition of rubidium and thus the scattering of this light is strongly suppressed. Nevertheless, there are still disturbing scattering events possible, when the intensity is increased accordingly. This leads to the transfer of atoms from the initial ground state to a detectable $|\mathrm{F} = 2\rangle$ ground state. Because already one atom in a wrong state would spoil the whole detection process (a photon would be counted although there wasn't one), a CO_2-laser has to be used in this experiment. Its far infrared light is so far detuned from the D1 and D2 lines that scattering is suppressed to less than 1 photon per second [CRGW03].

As a shortcoming, this light cannot be sent through ordinary glass windows and zinc-selenid (ZnSe) windows have to be used instead.
To enhance the optical density of the ensemble, an elongated atomic cloud will be used. A single beam trap would be ideal for this, but it cannot be used as it is not possible to overlap the single photons with the CO_2-laser because the ZnSe-windows would absorb the single photons. As a solution, a crossed beam geometry has been chosen. The dipole trap beams meet under an angle of 60° and create a slightly elongated cloud. The single photons are then sent along the long axis of the cloud.

As it is not possible to optically pump atoms into state $|a\rangle$ with high efficiency, the atoms are first pumped into state $|m\rangle$ and then transferred to state $|a\rangle$ with a microwave Landau-Zener sweep [RKLK81]. The complete level scheme of the photon detection process is shown in figure 1.1.

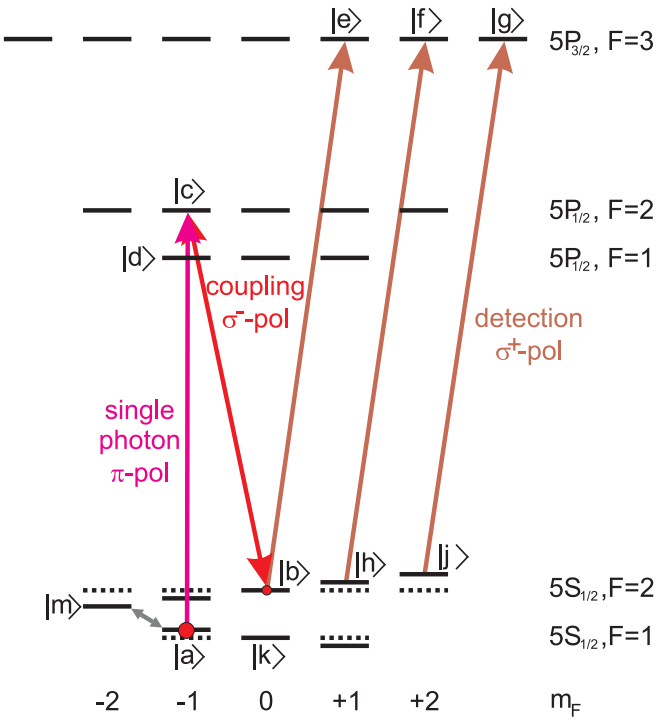

Fig. 1.1: Level scheme of ^{87}Rb, which will be used to detect single photons. All relevant states are shown, including the lasers that couple them to each other during the single photon transfer and the detection afterwards. Furthermore, the microwave transition, which is used at the end of the optical pumping process, is shown as a grey arrow. The D1 line is used for the single photon transfer and the D2 line for the detection process.

1.2.3 Adiabatic transfer

Then, together with a coupling laser, the single photons, which are resonant on the $|a\rangle$–$|c\rangle$ transition, are sent into the cloud. The coupling laser, which is resonant on the $|b\rangle$–$|c\rangle$ transition, ensures that the atoms end up in the defined state $|b\rangle$. To get an efficient transfer, the laser intensities will be modulated to perform a STIRAP-sequence (Stimulated Raman Adiabatic Passage) [BTS98], which is capable of unity transfer efficiency [GRSB90]. It is shown in figure 1.2.

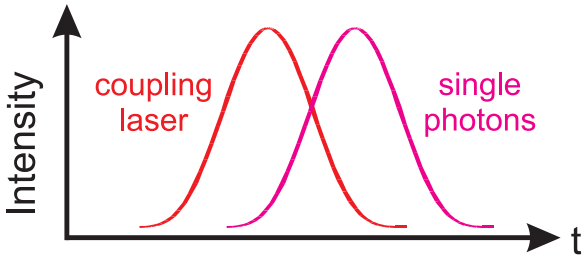

Fig. 1.2: Pulse sequence of the coupling and the probe laser. Here, the probe laser carries the single photons.

In this sequence, the coupling laser is turned on before the single photons arrive to create a quantum interference between two states (e.g. $|b\rangle$ and $|c\rangle$). Then it is slowly turned off while the probe laser (here the single photons) is slowly turned on (and then off again).
The polarizations of the Raman lasers are adjusted to connect the states $|a\rangle$, $|c\rangle$ and $|b\rangle$ with the polarizations shown in figure 1.1. In this configuration, the single photon is π-polarized because the $|a\rangle$–$|c\rangle$ transition has a higher Clebsch-Gordan-coefficient than the $|a\rangle$–$|d\rangle$ transition, which results in a higher optical density for the single photons.

1.2.4 Removal of unwanted atoms

There is another problem with the initial proposal: one detectable atom scatters about 10^4 photons per ms. Due to the solid angle ($\sim$ 1 %) and the detection efficiency ($\sim$ 70 %), about 70 scattered photons will be detected per ms. This is sufficient for single photon detection. But the atoms, which will remain in state $|a\rangle$ will offresonantly scatter the fluorescence light as well. Due to the large detuning (6.8 GHz), the scattering rate at low light intensities is suppressed by a factor of 10^6. Assuming 43000 atoms in this state (see section 8.1), this adds a negligible offset on the order of 0.043 (compared to the light of one atom) to the detection light. Within the detection time of 1 ms, about 430 photons will be scattered by these atoms. Due to the atomic decay, about 215 atoms will end up in an $|F = 2\rangle$ ground state, from where they will be indistinguishable from

the atoms, which have been transferred by single photons. Thus, the fluorescence light will increase exponentially and a single photon detection is not possible. Therefore, the atoms in state $|a\rangle$ have to be removed before the single atom detection process.
This can be done by applying a strong magnetic field gradient parallel to the offset field. In this configuration, the direction of the magnetic field is maintained and the gradient can more easily be achieved. This gradient pulls out all atoms which are not in the magnetically neutral states $|k\rangle$ and $|b\rangle$, in which the atoms are transferred by the single photons. (Due to the quadratic Zeeman effect, these states also become magnetic in very strong fields. But at the field strengths used in this experiment, this does not have to be taken into account.)
For the removal of the atoms, the dipole trap must be shallow enough and so it will be ramped down before the STIRAP.

1.2.5 The detection process

The transferred atoms will afterwards be detected by fluorescence. After few transitions between states $|b\rangle$, $|e\rangle$, $|h\rangle$ and $|f\rangle$, the atoms will end up in state $|j\rangle$ and scatter light on the closed $|j\rangle$–$|g\rangle$ transition, which can be detected with a high efficiency Em-CCD camera [MSK$^+$03, DAK$^+$05, WVS$^+$06]. The intensity of the scattered light is then proportional to the number of atoms in state $|j\rangle$, which is itself proportional to the number of incident single photons. Thus, a quantitative analysis of the scattered light yields the number of incident photons.

1.3 About this thesis

Within the scope of this work, the experiment has been designed and set up. Calculations have been made to determine its optimal parameters. The rubidium atoms have been captured in the MOT and afterwards in a single beam as well as in the crossed beam optical dipole trap. These optically trapped atoms have been used to measure electromagnetically induced transparency with the Raman laser system.
The design, setup and measurements are the content of this thesis.

In part I the required theoretical basics will be shown. As all experiments start with cooling and trapping of atoms, the cooling techniques used in this experiment will be first described in chapter 2. We will then turn the focus onto the optical properties of atoms, first of the simplified two-level atom in chapter 3, then on multilevel atoms in chapter 4.

In part II, the experimental setup will be explained, starting with the vacuum chamber in chapter 5, the magnetic fields in chapter 6 and the laser systems in chapter 7.

In part III, the calculations required for the design of the experiment and the measurements will be shown. They contain the calculations on the single photon detection and electromagnetically induced transparency, provided in chapters 8 and 9, respectively.

Finally, the experimental results will be presented in part IV. They contain the measurements on the magneto-optical trap and the dark MOT (chapter 10), the dipole trap (chapter 11), absorption measurements (chapter 12) and electromagnetically induced transparency (chapter 13).

The next steps of the experiment will be discussed in chapter 14 and additional information will be given in the appendices.

Part I

Theoretical basics

2. Atomic cooling

In this chapter, I will briefly discuss the different cooling techniques of the experiment. It starts with principle light forces, which can be used to build magneto-optical traps and optical dipole traps. These are described subsequently. Furthermore, the quadratic Stark effect will be introduced. This effect is not only necessary for the understanding of the working principle of optical dipole traps, but it is also responsible for limiting the bandwidth of EIT signals.
The chapter will close with basic information on magnetic forces and cold collisions.

2.1 Light forces in two-level-atoms

As it has been shown in [MvdS99], the total light force acting on two-level-atoms can be split into a dissipative spontaneous and a conservative dipole force

$$F = F_{sp} + F_{dip} \, . \tag{2.1}$$

The spontaneous force results from the momentum transfer from the light onto the atoms and the following random decay process. The so-called magneto-optical trap (MOT) is based on this force and sketched in section 2.2.

The dipole force results from the atomic polarizability that yields a dipole moment when atoms are irradiated with offresonant laser beams. The force of a strongly red-detuned focused laser beam can be used to trap ultracold atoms. That kind of trap is called an optical dipole trap and is described in section 2.3.

It is also possible to trap atoms magnetically. As the chamber also provides a magnetic trap, this is sketched in section 2.5.

2.2 Magneto-optical trap

When an atom is exposed to light, it scatters the light of the beam. Every time a photon is absorbed, it transfers its directed momentum onto the atom. As the following emission process has no preferred direction, all the momenta transferred in the emission cancel each other on average out. The resulting force can be used to build a magneto-optical trap. Here, usually 3 orthogonal pairs of counter-propagating circular polarized laser beams meet at the spot where the atoms shall be trapped (see figure 2.1). Due to the Doppler shift of the atoms, they create a velocity-dependent force

$$\vec{F} = -\beta\vec{v}\,, \tag{2.2}$$

where $\vec{v}$ denotes the velocity of the atoms and β is a proportionality factor.

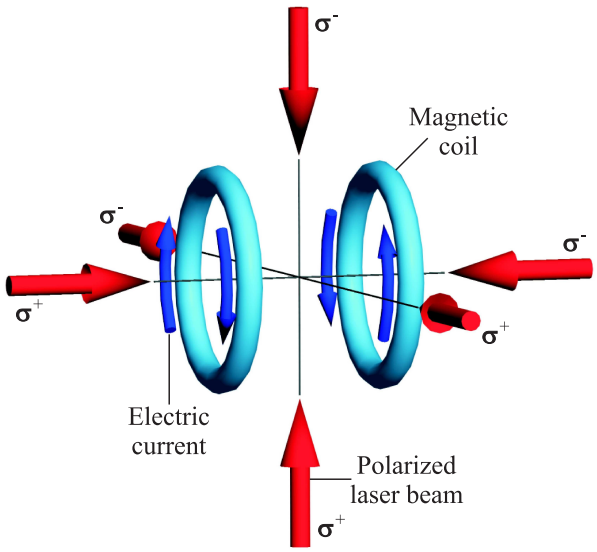

Fig. 2.1: Three-dimensional setup scheme of a MOT. It shows the six polarized laser beams, the magnetic coils and the electric currents which flow through them.

Additionally, two coils in Anti-Helmholtz-configuration create a magnetic quadrupole field. Its Zeeman shift alters the absorbtion probabilities of the 6 laser beams, which results in a spatial confinement of the atoms in space. Together with the velocity dependent force we get a confinement in momentum- and real space

$$\vec{F} = -\beta\vec{v} - \kappa\vec{r}\,, \tag{2.3}$$

where $\vec{r}$ denotes the spatial coordinate and κ is a proportionality factor.

A detailed description of magneto-optical traps is e.g. given in [MvdS99].

2.3 Dipole trap

The most simple optical dipole trap consists of one far red detuned laser that is tightly focused in the trap center [GWO00]. This offresonant laser induces a dipole moment in atoms, resulting in a potential that is given by

$$V = -\frac{1}{2}\alpha \cos^2 \omega t \, E_0^2 \,, \tag{2.4}$$

where $\alpha = \alpha(\omega)$ denotes the atomic polarizability (see section 2.4), ω the laser frequency and E_0 the electric field amplitude of the laser beam. Using the definition of the light intensity

$$I = \frac{1}{2} c \, \varepsilon_0 E_0^2 \tag{2.5}$$

and averaging over the fast oscillations of the light field, which the atoms cannot follow

$$\overline{\cos^2 \omega t}^T = \frac{1}{2} \tag{2.6}$$

we find

$$V = -\frac{1}{2}\frac{\alpha}{c \, \varepsilon_0} I. \tag{2.7}$$

The intensity of a circular Gaussian beam, which is propagating along the ζ-axis, is given by

$$I = \frac{2\,P}{\pi w^2} \, e^{-\frac{2\rho^2}{w^2}}, \tag{2.8}$$

where P denotes the laser power and ρ the radial coordinate. The beam waist w at a distance ζ from the trap center can be obtained from

$$w = w_0 \sqrt{1 + (\zeta/\zeta_0)^2}, \tag{2.9}$$

where w_0 is the beam waist at the trap center and ζ_0 the Rayleigh length

$$\zeta_0 = \frac{\pi w_0^2}{\lambda}. \tag{2.10}$$

Hence, we derive for the potential:

$$V = -\frac{\alpha P}{c \, \varepsilon_0 \pi w_0^2} \frac{1}{(1 + \frac{\zeta^2 \lambda^2}{\pi^2 w_0^4})} \exp\left(-\frac{2\rho^2}{w_0^2 (1 + \frac{\zeta^2 \lambda^2}{\pi^2 w_0^4})} \right) \tag{2.11}$$

For the case $\alpha > 0$, this potential is shown in figure 2.2.

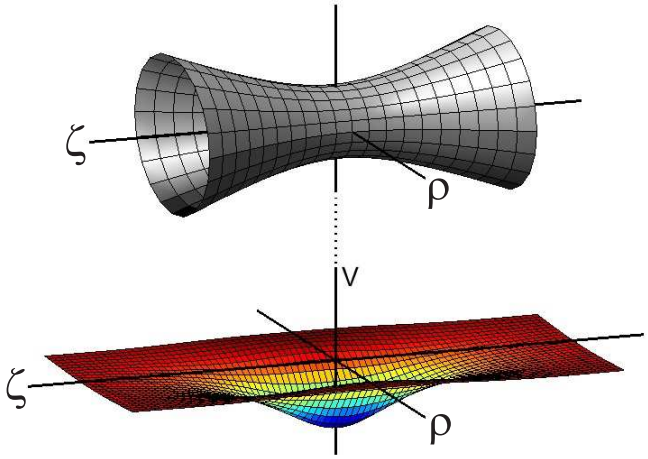

Fig. 2.2: A focused Gaussian beam traveling in the ζ-direction and the potential V of the dipole force created by this beam.

It is convenient to express the potential via trap frequencies for each direction, as it is usually done for the potential of a harmonic oscillator

$$V_{\mathrm{ho}} = \frac{1}{2} m \, \omega_x^2 \, x^2 \,, \tag{2.12}$$

For this, we first evaluate the potential along the respective axis, perform a Taylor expansion afterwards and neglect the lowest order term (the zero-point energy) as well as terms in higher order than 2:

$$\begin{aligned} V_\rho(\zeta = 0) &= -\frac{\alpha P}{\pi c \, \varepsilon_0 w_0^2} \, e^{-\frac{2\rho^2}{w_0^2}} \\ &\approx \frac{2\alpha P}{\pi c \, \varepsilon_0 w_0^4} \, \rho^2 \end{aligned} \tag{2.13}$$

Comparison with the harmonic oscillator (equation 2.12) leads to the radial trap frequency

$$\omega_{\rho,\,\zeta=0} \approx \frac{2\sqrt{\alpha P}}{\sqrt{m \, \pi c \, \varepsilon_0} \, w_0^2} \tag{2.14}$$

where m is the mass of a rubidium atom. Analogous we find the axial trap frequency

$$\omega_{\zeta,\,\rho=0} \approx \frac{\lambda\sqrt{2\,\alpha P}}{\sqrt{m\pi^3 \, c \, \varepsilon_0} \, w_0^3} \,. \tag{2.15}$$

The case of a dipole trap with two beams (crossed beam geometry) is discussed in appendix B.

2.3.1 Density distribution in a dipole trap

The density distribution of an atomic cloud follows a Maxwell-Boltzmann-distribution

$$n(\vec{r}) = n_0 e^{-\frac{U(\vec{r})}{k_B T}}. \tag{2.16}$$

In a dipole trap, the energy $U(\vec{r})$ equals the potential $V(\vec{r})$. For the three dimensions, the distribution in the harmonic regime is defined by the widths σ_i of the cloud. Comparing the two definitions of the distribution (via the widths and via the trapping potential)

$$\begin{aligned} n(\vec{r}) &= n_0 \exp\left(-\frac{m}{2k_B T}(\omega_x^2 x^2 + \omega_y^2 y^2 + \omega_z^2 z^2)\right) \\ &\stackrel{!}{=} n_0 \exp\left(-\frac{1}{2}\left(\frac{x^2}{\sigma_x^2} + \frac{y^2}{\sigma_y^2} + \frac{z^2}{\sigma_z^2}\right)\right) \end{aligned} \tag{2.17}$$

connects the widths with the trapping frequencies by

$$\sigma_i = \frac{1}{\omega_i}\sqrt{\frac{k_B T}{m}}\,; \qquad i = x,\, y,\, z \tag{2.18}$$

The peak density n_0 can be obtained from the integral

$$\begin{aligned} \int n(\vec{r})\, d^3\vec{r} &= N \\ \Longrightarrow \quad n_0 &= \frac{N}{(2\pi)^{3/2}\sigma_x\sigma_y\sigma_z}\,, \end{aligned} \tag{2.19}$$

with N being the total atom number.

2.4 Quadratic ac-Stark effect

In 1967, Sandars has shown that the hyperfine state of an atom contributes to its quadratic electric-field dependence [San67]. These small contributions ($\lesssim 10^{-5}$) are not relevant for capturing atoms in an optical dipole trap, but they have to be considered for an estimation of the minimum achievable EIT line width in optically trapped atoms, as will be shown in chapter 9.

For $F = I + 1/2$ states of hydrogen-like atoms, the polarizability is given by

$$\alpha(\omega) = \alpha_0(\omega) + \alpha_{10}(\omega) + \big(\alpha_{12}(\omega) + \alpha_{02}(\omega)\big)\,\frac{3m_F^2 - (I+\frac{1}{2})(I+\frac{3}{2})}{I(2I+1)} \tag{2.20}$$

and for $F = I - 1/2$ states by

$$\begin{aligned}\alpha(\omega) = \quad & \alpha_0(\omega) - \frac{I+1}{I}\,\alpha_{10}(\omega) + \frac{3m_F^2 - (I^2-\frac{1}{4})}{(I-1)(2I-1)} \\ & \times\left\{\frac{(2I-1)(I-1)}{I(2I+1)}\,\alpha_{12}(\omega) + \frac{(2I+3)(I-1)}{I(2I+1)}\,\alpha_{02}(\omega)\right\}\,.\end{aligned} \tag{2.21}$$

Here, I is the nuclear spin, $\alpha_0(\omega)$ is the familiar polarizability in the absence of hyperfine effects, while $\alpha_{10}(\omega)$, $\alpha_{12}(\omega)$ and $\alpha_{02}(\omega)$ are the contributions from the contact, the spin-dipolar and the quadrupole part of the hyperfine-interaction, respectively. As all polarizabilities depend on the laser frequency, we always have to take the far-offresonant values, as the optical dipole trap is far detuned from resonance.

According to Lipworth and Sandars, α_{12} and α_{02} occur only due to an electric field-induced admixture of the near-lying P-state of the same principle quantum number [LS64]. This allows to express them in terms of experimentally known quantities by

$$\alpha_{12} = 3\,I\,\frac{A_{3/2}\alpha_0}{4\,\Delta W} \tag{2.22}$$

$$\alpha_{02} = \frac{B_{3/2}\alpha_0}{2\,\Delta W}\,, \tag{2.23}$$

where ΔW is the energy difference between the nS and nP states and $A_{3/2}$ and $B_{3/2}$ are the magnetic dipole and electric quadrupole hyperfine constants of the $P_{3/2}$ state, respectively [CAB+68].

Using $\alpha_0 = 7.94 \cdot 10^{-6}\,\mathrm{Hz/(V/m)^2}$, $A_{3/2} = 84.7185\,\mathrm{MHz}$, $B_{3/2} = 12.4965\,\mathrm{MHz}$, $\Delta W = 3.84228 \cdot 10^{14}\,\mathrm{Hz}$ and $I = 3/2$ [Ste02], one finds

$$\alpha_{12} = 1.9695 \cdot 10^{-12}\,\mathrm{Hz}\frac{\mathrm{m}^2}{\mathrm{V}^2} \tag{2.24}$$

$$\alpha_{02} = 1.2912 \cdot 10^{-13}\,\mathrm{Hz}\frac{\mathrm{m}^2}{\mathrm{V}^2}. \tag{2.25}$$

In terms of the equations above, Mowat, who measured the $|\mathrm{F}=1,\, \mathrm{m_F}=0\rangle$–$|\mathrm{F}=2,\, \mathrm{m_F}=0\rangle$ transition in the ground state of rubidium [Mow72], was able to determine

$$\frac{4}{3}\alpha_{10} - \frac{1}{3}\alpha_{12} = 1.227 \cdot 10^{-10}\,\mathrm{Hz}\frac{\mathrm{m}^2}{\mathrm{V}^2}\,, \tag{2.26}$$

which leads to

$$\alpha_{10} = 9.252 \cdot 10^{-11}\,\mathrm{Hz}\frac{\mathrm{m}^2}{\mathrm{V}^2}. \tag{2.27}$$

This shows that the contact interaction (α_{10}) dominates the hyperfine contributions to the quadratic Stark shift.

2.5 Magnetic forces

Due to the Zeeman effect, also magnetic forces can be applied on atoms. The force of a magnetic gradient is given by

$$\vec{F}_y = -m_F g_F \mu_B \frac{d\vec{B}}{dy}\,, \tag{2.28}$$

where m_F denotes the magnetic quantum number of the hyperfine state F with respect to the quantization axis, g_F the Landé-g-factor and μ_B the Bohr-magneton. Such a gradient will e.g. be used to pull unwanted atoms out of the dipole trap.

But it can also be used to form a conservative potential for atoms, which results in a magnetic trap [Pri83]. The chamber provides a so-called QUIC-trap [EBH98], which requires only three magnetic coils. In the harmonic regime, its trap frequencies depend on the gradient and curvature of the magnetic field (denoted in the directions of our setup)

$$\omega_{x,z} = \sqrt{\frac{g_F m_F \mu_B}{m}\left(\frac{B'^2}{B_0} - \frac{B''}{2}\right)} \tag{2.29}$$

$$\omega_y = \sqrt{\frac{g_F m_F \mu_B}{m} B''}\,, \tag{2.30}$$

where B_0 denotes the field offset, B' the gradient in radial direction and B'' the field curvature.

2.6 Cold Collisions

In a MOT, the collisions of cold atoms with each other are not necessary for cooling while they are necessary for evaporative cooling in a dipole trap. But collisions also involve loss mechanisms for trapped atoms. These collisions can be treated quantum mechanically by the well developed scattering theory [BJL+02].

There exist three relevant kinds of collisions: elastic and inelastic collisions, as well as collisions with the background gas.

Elastic collisions can e.g. occur between two trapped atoms. In effect, they lead to a thermalization of the atomic cloud which is very important for the evaporative cooling, which uses the effect of thermalization. These collisions are called good collisions because they don't involve a loss of atoms.

Inelastic collisions also occur between two or more trapped atoms. But contrary to the elastic collisions, these collisions change e.g. the internal state of the atoms. It is possible that the spins of the atoms flip and the energy gained in this process can be transformed into kinetic energy, which causes the atom to leave the trap. Hence, these collisions are called bad collisions.

Another type of bad collisions are collisions between atoms and the background gas (and also collisions between the trapped atoms and atoms from the atom source). Here, it doesn't matter if the collisions are elastic or inelastic. As the background gas atoms are at room temperature, they kick every hit atom out of the trap, whose depth is only $\sim 10^{-5} T_{\mathrm{room}}$. This effect limits the lifetime in the trap, which can be estimated via

$$\tau_D \approx 1.3 \cdot 10^{-8} \, \frac{1}{p} \, \mathrm{mbar} \cdot \mathrm{s} \, , \tag{2.31}$$

where p denotes the pressure in the chamber [MvdS99].

It is obvious that a high ratio between good and bad collisions is needed to cool atoms in a dipole trap efficiently. For example, a ratio of more than 500 is needed for achieving a Bose-Einstein-Condensate (BEC).

3. Two-level atoms

In this chapter, I will first introduce the Rabi-frequency, which is a quantity for the light-matter interaction. It will be described for the cases of single photons, lasers acting on collective atomic states and and Gaussian laser beam acting on Boltzmann-distributed clouds.
The Rabi-frequencies will then be used to describe the light-matter interaction in two-level atoms, which will yield the atomic properties for the passage of light through the medium.

3.1 Single photon Rabi-frequency

Most calculations of the following sections depend on the Rabi-frequency, which is a quantity for the light-matter interaction and shall be introduced here:
if one neglects the zero-point energy of the light field, the interaction Hamiltonian between the light field and the atomic two-state system is given by [Sch01]

$$H_{int} = \hbar\Omega(\vec{r})\left(\hat{\sigma}\hat{a}^{\dagger} + \hat{\sigma}^{\dagger}\hat{a}\right) , \tag{3.1}$$

where $\hat{\sigma}^{\dagger}$ denotes the creation operator of the atomic state. That means, this operator causes an atom to get from the ground into the excited state. As the atom has to absorb light to get into the excited state, this operator always comes together with a destruction operator $\hat{a}$, that takes a photon out of the light field. $\hat{\sigma}$ and $\hat{a}^{\dagger}$ are the corresponding destruction and creation operators.
In equation 3.1,

$$\Omega(\vec{r}) = \frac{|\hat{\vec{d}}\hat{\vec{\epsilon}}|}{\hbar} E_0(\vec{r}) \tag{3.2}$$

denotes the space-dependent Rabi-frequency, with $\hat{\vec{d}}$ being the electric dipole moment operator of the atomic transition (the transition matrix element), $\hat{\vec{\epsilon}}$ the unit polarization vector of the electric field and $E_0(\vec{r})$ the electric field amplitude of the light.

Using the definition of the saturation intensity

$$I_{sat} = \frac{c\,\varepsilon_0 \Gamma^2 \hbar^2}{4|\hat{\vec{d}}\hat{\vec{\epsilon}}|^2} \tag{3.3}$$

and the intensity of the light field

$$I(\vec{r}) = \frac{1}{2} c\,\varepsilon_0 E_0^2(\vec{r})\,, \tag{3.4}$$

equation 3.2 reduces to

$$\Omega(\vec{r}) = \Gamma \sqrt{\frac{I(\vec{r})}{2I_{sat}}}. \tag{3.5}$$

For ^{87}Rb, numerical values of the saturation intensity can be found in [Ste02] for several polarization vectors.
For a Gaussian beam profile the intensity is not homogeneous over the area A of the beam and additionally the intensity of the pulse can be varied with time. For the case of a monochromatic quantized light field, the intensity can be obtained from the normalization integral

$$\int_0^{T_p} \int I(\vec{r})\, dA\, dt = n\,\hbar\omega\ . \tag{3.6}$$

Here, T_p and n denotes the length and the total photon number of the pulse, respectively. The equations above are valid for all quantized light fields, that means also for single photons.

3.1.1 Collective Excitations

Usually, the atoms in an ensemble are treated individually. But quantum mechanically they have to be treated as a collective [Dic54]: when an atom in an ensemble gets excited and it has not been measured which atom it is, the excitation does not correspond to a certain atom – it rather corresponds to a collective excitation of all atoms.
When all N atoms in an ensemble are in the ground state $|\mathrm{g}\rangle$, their collective ground state is given by a superposition of all ground states:

$$|g\rangle = |g,\, g,\, ...,\, g\rangle = |g\rangle_1\, |g\rangle_2 \cdots |g\rangle_N \tag{3.7}$$

If only the first (resp. second) atom is in an excited state $|\mathrm{e}\rangle$, the state of the ensemble is given by:

$$|e,\, g,\, ...,\, g\rangle = |e\rangle_1\, |g\rangle_2 \cdots |g\rangle_N \tag{3.8}$$

$$|g,\, e,\, ...,\, g\rangle = |g\rangle_1\, |e\rangle_2 \cdots |g\rangle_N \tag{3.9}$$

If the atom, that carries the single excitation is not known, the excitation is a symmetric superposition of all possible excited states:

$$|\psi\rangle_e = \frac{1}{\sqrt{N}}\big(|e,\, g,\, ...,\, g\rangle + |g,\, e,\, ...,\, g\rangle + \cdots + |g,\, g,\, ...,\, e\rangle\big)\ , \tag{3.10}$$

where the factor $1/\sqrt{N}$ comes from the normalization of this state. This formula is only valid if all atoms experience the same Rabi-frequency and thus have the same probability to get excited. If each atom i experiences the Rabi-frequency Ω_i, its probability of excitation gets modified. This changes also the superposition of the excited state:

$$|\psi\rangle_e = \frac{1}{\sqrt{\sum_i \Omega_i^2}}\big(\Omega_1|e,\, g,\, ...,\, g\rangle + \Omega_2|g,\, e,\, ...,\, g\rangle + \cdots + \Omega_N|g,\, g,\, ...,\, e\rangle\big)\ , \tag{3.11}$$

with the new normalization constant $1/\sqrt{\sum_i \Omega_i^2}$. The collective dipole operator is given by a sum over the dipole operators of each atom

$$\hat{d} = \hat{d}_1 + \hat{d}_2 + \cdots + \hat{d}_N\ , \tag{3.12}$$

where $\hat{d}_i$ only acts on atom i with the Rabi-frequency

$$\Omega_i = \langle g|\, \hat{d}_i\, |g,\, ...\, e_i,\, ...,\, g\rangle\ . \tag{3.13}$$

This finally leads to the modification of the Rabi-frequency

$$\langle g|\, \hat{d}\, |\psi\rangle_e = \sqrt{\sum_i \Omega_i^2} \tag{3.14}$$

of a collective atomic ensemble and a light field, where only one excitation is possible. For two and more possible excitations the formula has to be modified analogous [TIL03].
If all atoms experience the same Rabi-frequency, formula 3.14 simplifies to

$$\langle g|\, \hat{d}\, |\psi\rangle_e = \sqrt{N}\Omega \tag{3.15}$$

3.1.2 Collective Rabi-frequency in a Boltzmann-distributed cloud

In general, the simplified formulas above are not valid because the laser intensity as well as a cold atomic cloud are Gaussian and Boltzmann-distributed, respectively.

In the harmonic regime, the density of the cloud is given by a Gaussian (see section 2.3.1)

$$n_{3d} = n_0 \exp\left(-\frac{1}{2}\left(\frac{x^2}{\sigma_x^2} + \frac{y^2}{\sigma_y^2} + \frac{z^2}{\sigma_z^2}\right)\right) . \tag{3.16}$$

A laser traveling in positive x-direction "sees" the two-dimensional distribution of the cloud

$$n_{2d}(y,z) = \int_{-\infty}^{\infty} n_{3d}(\vec{r})\, dx = \frac{N}{2\pi\sigma_y\sigma_z} \exp\left(-\frac{1}{2}\left(\frac{y^2}{\sigma_y^2} + \frac{z^2}{\sigma_z^2}\right)\right) . \tag{3.17}$$

In this case, the sum in equation 3.14 has to be replaced by an integral:

$$\langle g|\, \hat{d}\, |\psi\rangle_e = \sqrt{\int_{-\infty}^{\infty}\int_{-\infty}^{\infty} \Omega^2(y,z)\, n_{2d}(y,z)\, dy\, dz} \tag{3.18}$$

This integrates the Rabi-frequency and the probability to find the respective Rabi-frequency over space. As the Rabi-frequency as well as the probability depend on the coordinates y and z, one has to integrate over them.
If we assume the Rayleigh-length of the probe beam to be much larger than the atomic cloud along the x-direction, the intensity of the probe beam is given by

$$I(y,z) = \frac{2\,P}{\pi w_y w_z} \exp\left(-2\left(\frac{y^2}{w_y^2} + \frac{z^2}{w_z^2}\right)\right) , \tag{3.19}$$

where P, w_y and w_z are the power and the beam waists of the laser.
The space-dependent Rabi-frequency is given by

$$\Omega(y,z) = \Gamma\sqrt{\frac{I(y,z)}{2I_{sat}}} \tag{3.20}$$

This leads to the overlap integral between the Gaussian single photon beam and the atomic distribution

$$\begin{aligned}
\Omega_{tot} = \langle g|\, \hat{d}\, |\psi\rangle_e &= \left\{ \int_{-\infty}^{\infty}\int_{-\infty}^{\infty} \frac{\Gamma^2}{2I_{sat}} \frac{2\,P}{\pi w_y w_z} \exp\left(-2\left(\frac{y^2}{w_y^2} + \frac{z^2}{w_z^2}\right)\right) \right. \\
&\quad \left. \times\ \frac{N}{2\pi\sigma_y\sigma_z} \exp\left(-\frac{1}{2}\left(\frac{y^2}{\sigma_y^2} + \frac{z^2}{\sigma_z^2}\right)\right) dy\, dz \right\}^{1/2} \\
&= \Gamma\sqrt{\frac{P\,N}{I_{sat}}} \frac{1}{(4\,\sigma_y^2 + w_y^2)^{1/4}} \frac{1}{(4\,\sigma_z^2 + w_z^2)^{1/4}} .
\end{aligned} \tag{3.21}$$

It can be seen that the collective Rabi-frequency becomes maximal when the beam focus is minimized.

3.2 Description of the two-level atom

The most basic atomic model consists of two levels, which are coupled by a laser. This model is sketched in figure 3.1.

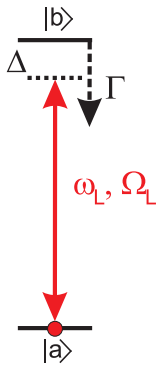

Fig. 3.1: Two atomic levels and the laser, that couples the states. The laser has a frequency ω_L and a Rabi-frequency Ω_L. $|a\rangle$ denotes the ground state, $|b\rangle$ the excited state. The decay rate of the excited state $|b\rangle$ is Γ. In the case shown, the detuning Δ is negative.

For a single two-level atom, I will define the following basis for the states shown in figure 3.1:

$$|a\rangle = \begin{pmatrix} 0 \\ 1 \end{pmatrix}; \qquad |b\rangle = \begin{pmatrix} 1 \\ 0 \end{pmatrix} \tag{3.22}$$

The atomic state $|\psi\rangle$ is then given by

$$|\psi\rangle = c_{|a\rangle}|a\rangle + c_{|b\rangle}|b\rangle = \begin{pmatrix} c_{|b\rangle} \\ c_{|a\rangle} \end{pmatrix} , \tag{3.23}$$

where $c_{|a\rangle}$ and $c_{|b\rangle}$ denote the population amplitudes in the indicated states. Neglecting the movement of the atoms, the Hamiltonian of the combined atom-light system is then the sum of the internal Hamiltonian and the Hamiltonian of the light-matter interaction, represented by the Rabi-frequency Ω

$$\begin{aligned} \frac{\hat{H}}{\hbar} &= \omega_{|a\rangle}\ |a\rangle\langle a| \ + \omega_{|b\rangle}\ |b\rangle\langle b| \\ &+ \ \Omega\ \cos(\omega_L t)\, |a\rangle\langle b| \\ &+ \ \Omega^\star \cos(\omega_L t)\, |b\rangle\langle a| \ . \end{aligned} \tag{3.24}$$

$\hbar\omega_{|a\rangle}$ and $\hbar\omega_{|b\rangle}$ denote the energies of the indicated atomic levels, while ω_L denotes the frequency of the laser. The frequencies are connected with the detuning Δ of the lasers via

$$\omega_L = \omega_{|b\rangle} - \omega_{|a\rangle} + \Delta \ . \tag{3.25}$$

The cosine corresponds to the oscillation of the light wave with the frequency ω_L. Replacing the cosine by exponential functions and combining the equation in a matrix yields

$$\frac{\hat{H}}{\hbar} = \begin{pmatrix} \omega_{|b\rangle} & \frac{1}{2}\Omega^\star(e^{i\omega_L t} + e^{-i\omega_L t}) \\ \frac{1}{2}\Omega(e^{i\omega_L t} + e^{-i\omega_L t}) & \omega_{|a\rangle} \end{pmatrix} . \tag{3.26}$$

The equations can be further simplified by transforming the Hamiltonian into a frame that rotates with the laser frequency via [Hen04]

$$\hat{\tilde{H}} = U^\dagger \hat{H} U - i\hbar U^\dagger \partial_t U . \tag{3.27}$$

The transformation matrices are given by

$$\begin{aligned} U &= \exp\Big\{ + it\omega_L |a\rangle\langle a| \Big\} = \exp\left\{ +it \begin{pmatrix} 0 & 0 \\ 0 & \omega_L \end{pmatrix} \right\} = \begin{pmatrix} 1 & 0 \\ 0 & e^{+i\omega_L t} \end{pmatrix} \\ U^\dagger &= \exp\Big\{ - it\omega_L |a\rangle\langle a| \Big\} = \exp\left\{ -it \begin{pmatrix} 0 & 0 \\ 0 & \omega_L \end{pmatrix} \right\} = \begin{pmatrix} 1 & 0 \\ 0 & e^{-i\omega_L t} \end{pmatrix} \end{aligned}$$

$$\partial_t U = \begin{pmatrix} 0 & 0 \\ 0 & i\omega_L e^{i\omega_L t} \end{pmatrix} \tag{3.28}$$

The entries of these matrices rotate with the laser frequency ω. The first term of the new Hamiltonian thus becomes:

$$\frac{U^\dagger \hat{H} U}{\hbar} = \begin{pmatrix} \omega_{|b\rangle} & \frac{\Omega^\star}{2}(e^{i\omega_L t} + e^{-i\omega_L t}) e^{i\omega_L t} \\ \frac{\Omega}{2}(e^{i\omega_L t} + e^{-i\omega_L t}) e^{-i\omega_L t} & \omega_{|a\rangle} \end{pmatrix} \tag{3.29}$$

Now we expand the terms. The terms containing one '+' and one '−' sign in the exponent cancel down to 1. The other terms rotate with the double frequency $2\,\omega_L$ or $-2\,\omega_L$. We assume that they rotate so fast that they cancel out in average. Furthermore, these terms correspond to improbable two-photon-transitions [Sch01], which is also a justification to neglect them. This is called the rotating wave approximation (RWA) and simplifies the above term to

$$\frac{U^\dagger \hat{H} U}{\hbar} = \begin{pmatrix} \omega_{|b\rangle} & \frac{1}{2}\Omega^\star \\ \frac{1}{2}\Omega & \omega_{|a\rangle} \end{pmatrix} . \tag{3.30}$$

By adding the second term of equation 3.27

$$\frac{-i\hbar U^\dagger \partial_t U}{\hbar} = \begin{pmatrix} 0 & 0 \\ 0 & \omega_L \end{pmatrix} , \tag{3.31}$$

simplifying the equations with help of the detuning (see figure 3.1), taking $\hbar\omega_{|b\rangle}$ as the zero-point energy and adding the atomic decay we find

$$\frac{\hat{\tilde{H}}}{\hbar} = \frac{U^\dagger \hat{H} U - i\hbar U^\dagger \partial_t U}{\hbar} = \begin{pmatrix} -i\frac{\Gamma}{2} & \frac{1}{2}\Omega^\star \\ \frac{1}{2}\Omega & \Delta \end{pmatrix} . \tag{3.32}$$

The atomic populations can then be calculated via the time-dependent Schrödinger-equation

$$\frac{\hat{\tilde{H}}}{\hbar}|\psi\rangle = i\frac{\partial|\psi\rangle}{\partial t} , \tag{3.33}$$

where the wave function $|\psi\rangle$ is given by equation 3.23.

Because not only the atomic populations but also the coherence between them is of interest, we evaluate the behavior of the system with help of the density matrix

$$\hat{\rho} = \begin{pmatrix} \rho_{bb} & \rho_{ba} \\ \rho_{ab} & \rho_{aa} \end{pmatrix} . \tag{3.34}$$

Using the Liouville equation

$$i\,\hbar\,\dot{\hat{\rho}} = \hat{\tilde{H}}\hat{\rho} - \hat{\rho}\hat{\tilde{H}}^\dagger \tag{3.35}$$

and the hermitian conjugated Hamiltonian

$$\frac{\hat{\tilde{H}}^\dagger}{\hbar} = \begin{pmatrix} +i\frac{\Gamma}{2} & \frac{1}{2}\Omega^\star \\ \frac{1}{2}\Omega & \Delta \end{pmatrix} \tag{3.36}$$

yields a linear system of coupled differential equations of first order for the density matrix elements

$$\begin{aligned} \dot{\rho}_{bb} &= -\Gamma\rho_{bb} - \frac{i}{2}(\Omega\rho_{ba} - \Omega^\star\rho_{ab}) \\ \dot{\rho}_{aa} &= -\frac{i}{2}(\Omega\rho_{ba} - \Omega^\star\rho_{ab}) \\ \dot{\rho}_{ba} &= (-\frac{\Gamma}{2} + i\Delta)\rho_{ba} - \frac{i}{2}\Omega^\star(\rho_{aa} - \rho_{bb}) \\ \dot{\rho}_{ab} &= (-\frac{\Gamma}{2} - i\Delta)\rho_{ab} + \frac{i}{2}\Omega(\rho_{aa} - \rho_{bb}) . \end{aligned} \tag{3.37}$$

These equations can also be written as a 2×2 matrix. As the Hamiltonian contains only the decay of the coherences and the populations, the population of the excited state decays but does not end up in the ground state. If one wants to include this, the term $+\Gamma\rho_{bb}$ has to be added to the matrix element of the ground state.

Usually, the Rabi-frequency is real, that means $\Omega = \Omega^\star$. The four equations can be reduced to 3 since

$$\rho_{ba} = \rho_{ab}^\star \tag{3.38}$$

is valid and the system is overdetermined.

Besides the description of the internal atomic states, equations 3.37 can also be used to derive the rate at which a two-level atom scatters light [MvdS99]. This scattering rate reads

$$\gamma_{p_0} = \frac{\Gamma}{2} \frac{I/I_{sat}}{1 + I/I_{sat} + (2\delta/\Gamma)^2} \ , \tag{3.39}$$

where Γ is the natural decay rate, I the light intensity, I_{sat} the saturation intensity and δ the detuning from resonance.

3.3 Optical properties

If the Rabi-frequencies are not time-dependent, the equations 3.37 can be solved analytically by diagonalizing the 2×2 matrix. This can also be done for time-dependent Rabi-frequencies, but then the change in the Rabi-frequency must be so low that the atomic system can follow it adiabatically.
However, the complete analytic solution is too long to be written out here, but it can be approximated when we assume all atoms to be in state $|\mathrm{a}\rangle$, that is $\rho_{aa} \approx 1$. The polarization of the atomic medium is then given by [Zim05]

$$P = n_0 \left[\mu \rho_{ba} + c.c.\right] \ , \tag{3.40}$$

where μ denotes the dipole matrix element of the transition and n_0 the atom number density. From this we get the linear susceptibility of the two-level atom [Zim05, Sut97]

$$\chi_{2\mathrm{l}} = \frac{|\mu|^2 n_0}{\hbar \epsilon_0} \frac{\Delta + i\frac{\Gamma}{2}}{(\frac{\Gamma}{2})^2 + \Delta^2} \ . \tag{3.41}$$

This formula describes the absorptive as well as the dispersive properties of the medium. The transmitted electric field is then given by

$$E_{out} = E_{in} \cdot \exp\left\{ikl\chi_{2\mathrm{l}}/2\right\} \ , \tag{3.42}$$

where l denotes the length of the medium and k the wave number.

The intensity transmission is given by the imaginary part of the susceptibility and the phase shift by the real part of the susceptibility. They are plotted in figure 3.2.

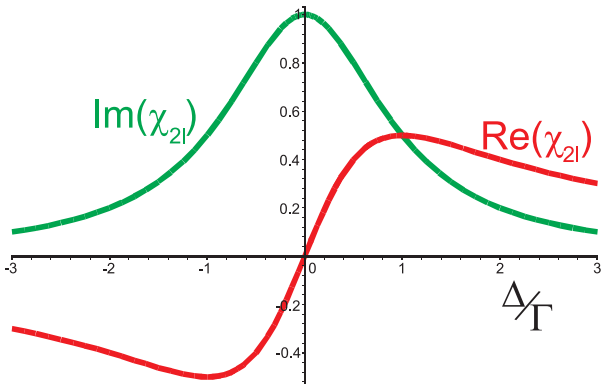

Fig. 3.2: Real and imaginary part of the susceptibility, plotted for $n_0|\mu|^2/\hbar\varepsilon_0 = 1$. On resonance, the absorption is maximal and the phase shift zero. For large detunings, the absorption vanishes together with the phase shift.

The group velocity is associated to the derivative of the refractive index

$$n = \sqrt{1 + \mathrm{Re}\chi_{21}} \tag{3.43}$$

via

$$v_{gr}(\Delta = 0) = \frac{c}{n + \omega_L \frac{dn}{d\omega_L}\Big|_{\Delta=0}} = \frac{c}{1 + \frac{2\omega_L|\mu|^2 n_0}{\varepsilon_0 \hbar \Gamma^2}} , \tag{3.44}$$

where I have used

$$\omega_L = \omega_0 + \Delta \Longrightarrow d\omega_L = d\Delta . \tag{3.45}$$

In a typical atomic cloud, the group velocity is reduced by three orders of magnitude.

4. Multilevel atoms

This chapter deals with multilevel atoms and the properties they provide for the passage of light through the medium. It starts with a survey of effects that are observable in three-levels atoms. The effects are based on the quantum mechanical description of the three-level atom, which will be discussed subsequently. In the following sections, the effects themselves will be discussed. Corrections of the three-level atom are discussed in section 4.7 and the expansion to the second quantization is given in appendix C.

4.1 Three-level phenomena

Contrary to two-level atoms, more physical effects can be observed in three-level-atoms. These effects are e.g. electromagnetically induced transparency (EIT), dark state polaritons (DSPs), stimulated Raman adiabatic passage (STIRAP), coherent population trapping (CPT) and slow and stored light.

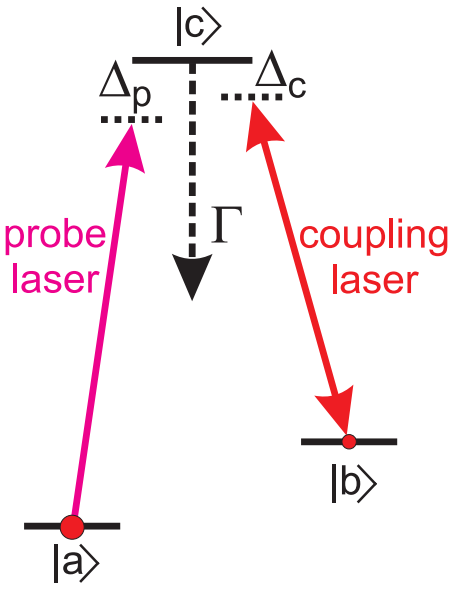

Fig. 4.1: Three atomic levels in Λ-configuration: $|a\rangle$ and $|b\rangle$ denote the ground states, $|c\rangle$ the excited state. The atoms shall be initially in the ground state $|a\rangle$. The probe laser couples states $|a\rangle$ and $|c\rangle$, where the detuning is denoted with Δ_p, while the coupling laser couples states $|b\rangle$ and $|c\rangle$, where the detuning is denoted with Δ_c. The decay rate of the excited state $|c\rangle$ is Γ. In the case shown, the detunings Δ_p and Δ_c are negative.

Most experiments in this field are performed in Λ-type atomic systems (see figure 4.1). Here, two ground states are coupled by two lasers via an intermediate state. The effects can also be observed in three level systems with another arrangement of the internal states (namely the ladder- and V-type systems). Because they are not part of this thesis, I refer to the literature [SZ97].

All the phenomena mentioned above are based on the same principle: the medium is probed with a probe laser that can be absorbed and excite atoms into state $|c\rangle$. The coupling creates a second path to excite atoms. There, atoms can be excited to state $|c\rangle$, then transferred to state $|b\rangle$ and back to state $|c\rangle$ by the coupling laser. As this path allows for a different phase, the lasers can be adjusted to let the two paths destructively interfere. Then, the absorption of the medium is canceled out for the probe laser, which yields complete transparency. This phenomenon is called electromagnetically induced transparency and will be introduced in the following sections. The two destructive paths are shown in figure 4.2.

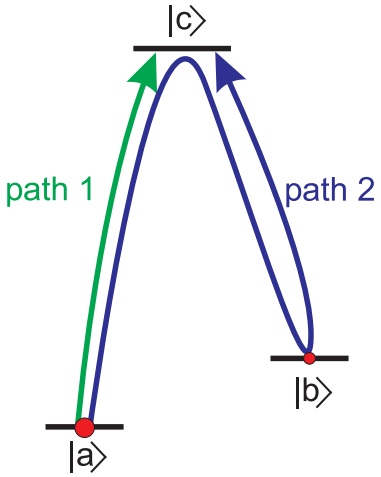

Fig. 4.2: The two possible absorption paths that destructively interfere and create electromagnetically induced transparency.

An important feature of EIT is a strongly reduced group velocity of the probe beam (slowed light). For the slowing process, the phase information of the light is temporarily stored in a collective excitation of the atomic cloud. These excitations can be described by a quasi-particle, the so-called dark state polariton (DSP). The particle nature of DSPs has been demonstrated recently [KW06].

DSPs can be used to store light temporarily: when the intensities of the coupling and the probe laser follow the STIRAP-scheme (see figure 4.3), the probe light gets stored in the atomic cloud, until a second coupling laser transfers the dark state polaritons back to light.

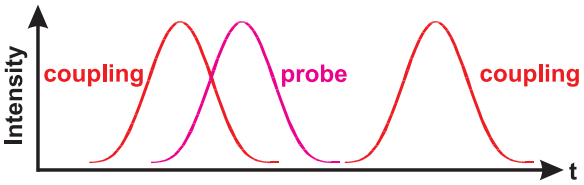

Fig. 4.3: Pulse sequence of the coupling and the probe laser to perform a stimulated Raman adiabatic passage. The second coupling pulse transforms the polaritons back to light.

If strong lasers are used (number of photons ≫ number of atoms), the atomic population can be transferred from state |a⟩ to state |b⟩ with unity efficiency. This is called coherent population trapping (CPT).
All these effects are based on the three-level atom and will be introduced in the following sections.

4.2 3-level-Λ-system

Now, we will derive the time evolution of the three-level-Λ-system in the same way as for the two-level system in section 3.2. For this, I will define the following basis for the states shown in figure 4.1 of a single three-level atom:

$$|a\rangle = \begin{pmatrix} 0 \\ 0 \\ 1 \end{pmatrix}; \qquad |b\rangle = \begin{pmatrix} 0 \\ 1 \\ 0 \end{pmatrix}; \qquad |c\rangle = \begin{pmatrix} 1 \\ 0 \\ 0 \end{pmatrix} \tag{4.1}$$

The atomic state $|\psi\rangle$ is then given by

$$|\psi\rangle = c_{|a\rangle}|a\rangle + c_{|b\rangle}|b\rangle + c_{|c\rangle}|c\rangle = \begin{pmatrix} c_{|c\rangle} \\ c_{|b\rangle} \\ c_{|a\rangle} \end{pmatrix}, \tag{4.2}$$

where $c_{|a\rangle}$, $c_{|b\rangle}$ and $c_{|c\rangle}$ denote the population amplitudes in the indicated states. The Hamiltonian of the combined atom-light system is then the sum of the internal Hamiltonian and the Hamiltonian of the light-matter interaction, given by the probe and the coupling laser, represented by their respective Rabi-frequencies Ω_p and Ω_c

$$\begin{aligned} \frac{\hat{H}}{\hbar} &= \omega_{|a\rangle}\,|a\rangle\langle a| + \omega_{|b\rangle}\,|b\rangle\langle b| + \omega_{|c\rangle}\,|c\rangle\langle c| \\ &+ \Omega_p \cos(\omega_p t)\,|a\rangle\langle c| \\ &+ \Omega_p^\star \cos(\omega_p t)\,|c\rangle\langle a| \\ &+ \Omega_c \cos(\omega_c t)\,|b\rangle\langle c| \\ &+ \Omega_c^\star \cos(\omega_c t)\,|c\rangle\langle b| \,. \end{aligned} \tag{4.3}$$

$\omega_{|a\rangle}$, $\omega_{|b\rangle}$ and $\omega_{|c\rangle}$ denote the energies of the indicated atomic levels, while ω_p and ω_c denote the frequencies of the probe and the coupling laser, respectively (that means $\omega_c \neq \omega_{|c\rangle}$). The frequencies are connected with the detunings Δ_p and Δ_c of the lasers via

$$\begin{aligned} \omega_p &= \omega_{|c\rangle} - \omega_{|a\rangle} + \Delta_p \\ \omega_c &= \omega_{|c\rangle} - \omega_{|b\rangle} + \Delta_c \, . \end{aligned} \tag{4.4}$$

The cosine corrsponds the respective oscillation of the light wave with the frequencies ω_p and ω_c. Replacing the cosine by exponential functions and combining the equation in a matrix yields

$$\frac{\hat{H}}{\hbar} = \begin{pmatrix} \omega_{|c\rangle} & \frac{1}{2}\Omega_c^\star(e^{i\omega_c t} + e^{-i\omega_c t}) & \frac{1}{2}\Omega_p^\star(e^{i\omega_p t} + e^{-i\omega_p t}) \\ \frac{1}{2}\Omega_c(e^{i\omega_c t} + e^{-i\omega_c t}) & \omega_{|b\rangle} & 0 \\ \frac{1}{2}\Omega_p(e^{i\omega_p t} + e^{-i\omega_p t}) & 0 & \omega_{|a\rangle} \end{pmatrix} \, . \tag{4.5}$$

The equations can be further simplified by transforming the Hamiltonian in a frame, that rotates with the frequencies of the two lasers via [Hen04]

$$\hat{\tilde{H}} = U^\dagger \hat{H} U - i\hbar U^\dagger \partial_t U \, . \tag{4.6}$$

The transformation matrices are given by

$$\begin{aligned} U &= \exp\Big\{ it\omega_p |a\rangle\langle a| + it\omega_c |b\rangle\langle b| \Big\} \\ &= \exp\left\{ it \begin{pmatrix} 0 & 0 & 0 \\ 0 & \omega_c & 0 \\ 0 & 0 & \omega_p \end{pmatrix} \right\} = \begin{pmatrix} 1 & 0 & 0 \\ 0 & e^{i\omega_c t} & 0 \\ 0 & 0 & e^{i\omega_p t} \end{pmatrix} \end{aligned}$$

$$\begin{aligned} U^\dagger &= \exp\Big\{ -it\omega_p |a\rangle\langle a| - it\omega_c |b\rangle\langle b| \Big\} \\ &= \exp\left\{ -it \begin{pmatrix} 0 & 0 & 0 \\ 0 & \omega_c & 0 \\ 0 & 0 & \omega_p \end{pmatrix} \right\} = \begin{pmatrix} 1 & 0 & 0 \\ 0 & e^{-i\omega_c t} & 0 \\ 0 & 0 & e^{-i\omega_p t} \end{pmatrix} \end{aligned}$$

$$\partial_t U = \begin{pmatrix} 0 & 0 & 0 \\ 0 & i\omega_c e^{i\omega_c t} & 0 \\ 0 & 0 & i\omega_p e^{i\omega_p t} \end{pmatrix} \tag{4.7}$$

The entries of these matrices rotate with the two laser frequencies ω_p and ω_c. The choice of this base helps to get rid off any terms which contain the ground state

splitting $\omega_{|b\rangle} - \omega_{|a\rangle}$. The first term of the new Hamiltonian thus becomes:

$$\frac{U^\dagger \hat{H} U}{\hbar} = \tag{4.8}$$
$$\begin{pmatrix} \omega_{|c\rangle} & \frac{\Omega_c^\star}{2}(e^{i\omega_c t}+e^{-i\omega_c t})e^{i\omega_c t} & \frac{\Omega_p^\star}{2}(e^{i\omega_p t}+e^{-i\omega_p t})e^{i\omega_p t} \\ \frac{\Omega_c}{2}(e^{i\omega_c t}+e^{-i\omega_c t})e^{-i\omega_c t} & \omega_{|b\rangle} & 0 \\ \frac{\Omega_p}{2}(e^{i\omega_p t}+e^{-i\omega_p t})e^{-i\omega_p t} & 0 & \omega_{|a\rangle} \end{pmatrix} .$$

Now we expand the terms. The terms containing one '+' and one '−' sign in the exponent cancel down to 1. The other terms rotate with the double frequency, e.g. $2\,\omega_p$. We assume that they rotate so fast that they cancel out in average. Furthermore, these terms correspond to improbable two-photon-transitions [Sch01], which also justifies to neglect them. This is called the rotating wave approximation (RWA) and simplifies the above term to

$$\frac{U^\dagger \hat{H} U}{\hbar} = \begin{pmatrix} \omega_{|c\rangle} & \frac{1}{2}\Omega_c^\star & \frac{1}{2}\Omega_p^\star \\ \frac{1}{2}\Omega_c & \omega_{|b\rangle} & 0 \\ \frac{1}{2}\Omega_p & 0 & \omega_{|a\rangle} \end{pmatrix} . \tag{4.9}$$

By adding the second term of equation 4.6

$$\frac{-i\hbar U^\dagger \partial_t U}{\hbar} = \begin{pmatrix} 0 & 0 & 0 \\ 0 & +\omega_c & 0 \\ 0 & 0 & +\omega_p \end{pmatrix} , \tag{4.10}$$

simplifying the equations with help of the detunings (see figure 4.1) and adding the atomic decay we find

$$\frac{\hat{\tilde{H}}}{\hbar} = \frac{U^\dagger \hat{H} U - i\hbar U^\dagger \partial_t U}{\hbar} = \begin{pmatrix} -i\frac{\Gamma}{2} & \frac{1}{2}\Omega_c^\star & \frac{1}{2}\Omega_p^\star \\ \frac{1}{2}\Omega_c & \Delta_c & 0 \\ \frac{1}{2}\Omega_p & 0 & \Delta_p \end{pmatrix} . \tag{4.11}$$

The atomic populations can then be calculated via the time-dependent Schrödinger-equation

$$\frac{\hat{\tilde{H}}}{\hbar}|\psi\rangle = i\frac{\partial|\psi\rangle}{\partial t} , \tag{4.12}$$

where the wave function $|\psi\rangle$ is given by equation 4.2.

Because not only the atomic populations but also the coherence between them is of interest, we evaluate the behavior of the system with help of the density matrix

$$\hat{\rho} = \begin{pmatrix} \rho_{cc} & \rho_{cb} & \rho_{ca} \\ \rho_{bc} & \rho_{bb} & \rho_{ba} \\ \rho_{ac} & \rho_{ab} & \rho_{aa} \end{pmatrix} . \tag{4.13}$$

Using the Liouville equation

$$i\,\hbar\,\dot{\hat{\rho}} = \hat{\tilde{H}}\hat{\rho} - \hat{\rho}\hat{\tilde{H}}^{\dagger} \tag{4.14}$$

and the hermitian conjugated Hamiltonian

$$\frac{\hat{\tilde{H}}^{\dagger}}{\hbar} = \begin{pmatrix} +i\frac{\Gamma}{2} & \frac{1}{2}\Omega_c^{\star} & \frac{1}{2}\Omega_p^{\star} \\ \frac{1}{2}\Omega_c & \Delta_c & 0 \\ \frac{1}{2}\Omega_p & 0 & \Delta_p \end{pmatrix} \tag{4.15}$$

yields a linear system of coupled differential equations of first order for the density matrix elements

$$\begin{aligned}
\dot{\rho}_{cc} &= -\Gamma\rho_{cc} - \frac{i}{2}(\Omega_c\rho_{cb} - \Omega_c^{\star}\rho_{bc}) - \frac{i}{2}(\Omega_p\rho_{ca} - \Omega_p^{\star}\rho_{ac}) \\
\dot{\rho}_{bb} &= -\frac{i}{2}(\Omega_c\rho_{cb} - \Omega_c^{\star}\rho_{bc}) \\
\dot{\rho}_{aa} &= -\frac{i}{2}(\Omega_p\rho_{ca} - \Omega_p^{\star}\rho_{ac}) \\
\dot{\rho}_{cb} &= (-\frac{\Gamma}{2} + i\Delta_c)\rho_{cb} - \frac{i}{2}\Omega_c^{\star}(\rho_{bb} - \rho_{cc}) - \frac{i}{2}\Omega_p^{\star}\rho_{ab} \\
\dot{\rho}_{bc} &= (-\frac{\Gamma}{2} - i\Delta_c)\rho_{bc} + \frac{i}{2}\Omega_c(\rho_{bb} - \rho_{cc}) + \frac{i}{2}\Omega_p\rho_{ba} \\
\dot{\rho}_{ca} &= (-\frac{\Gamma}{2} + i\Delta_p)\rho_{ca} - \frac{i}{2}\Omega_p^{\star}(\rho_{aa} - \rho_{cc}) - \frac{i}{2}\Omega_c^{\star}\rho_{ba} \\
\dot{\rho}_{ac} &= (-\frac{\Gamma}{2} - i\Delta_p)\rho_{ac} + \frac{i}{2}\Omega_p(\rho_{aa} - \rho_{cc}) + \frac{i}{2}\Omega_c\rho_{ab} \\
\dot{\rho}_{ba} &= i(\Delta_p - \Delta_c)\rho_{ba} - \frac{i}{2}(\Omega_c\rho_{ca} - \Omega_p^{\star}\rho_{bc}) \\
\dot{\rho}_{ab} &= i(\Delta_c - \Delta_p)\rho_{ab} + \frac{i}{2}(\Omega_c^{\star}\rho_{ac} - \Omega_p\rho_{cb}) .
\end{aligned} \tag{4.16}$$

These equations can also be written as a 3×3 matrix. As the Hamiltonian contains only the decay of the coherences and the populations, the population of the excited state decays but does not end up in the ground states. If one wants to include this, terms depending on the decay strength of the respective transition have to be added to the matrix elements of the ground states.

In the three-level system, the terms are

$$\dot{\rho}_{aa} = +CG_{ac}^2 \Gamma \rho_{cc} \tag{4.17}$$
$$\dot{\rho}_{bb} = +CG_{bc}^2 \Gamma \rho_{cc} \ , \tag{4.18}$$

where CG_{ac} and CG_{bc} denote the Clebsch-Gordan-coefficients on the indicated transitions.
If a decay of the ground states occurs in the system, additional decay terms have to be added in the same way.
Usually, the Rabi-frequencies are real, that means $\Omega = \Omega^\star$. The nine equations can be reduced to 6 since

$$\rho_{cb} = \rho_{bc}^\star; \qquad \rho_{ca} = \rho_{ac}^\star; \qquad \rho_{ba} = \rho_{ab}^\star \tag{4.19}$$

is valid and the system is overdetermined.
Appendix C shows a derivation of the three-level atom in second quantization. The results show the consistency between the classical three-level atom (shown in this section) and the single photon Rabi-frequency (section 3.1).

4.3 EIT and slow light

If the Rabi-frequencies are time-dependent, the equations above must be solved numerically. This has been done for the calculation of the single photon detection, as it is described in section 8.1.
If the Rabi-frequencies are not time-dependent, the equations can be solved analytically by diagonalizing the 3×3 matrix. This can also be done for time-dependent Rabi-frequencies, but then the change in the Rabi-frequency must be so low that the atomic system can follow it adiabatically.
However, the complete analytic solution is too long to be written out here, but it can be approximated under certain conditions: we assume all atoms to be in state $|\mathrm{a}\rangle$, that is $\rho_{aa} \approx 1$. This can e.g. be achieved by using a strong coupling laser that ensures to pump back all atoms, once they are in state $|\mathrm{b}\rangle$ or the use of very weak probe pulses because few photons cannot transfer many atoms into another state.
The polarization of the atomic medium is then given by [FIM05]

$$P = n_0 \left[\mu_{ac}\rho_{ca} + \mu_{bc}\rho_{cb} + c.c.\right] \ , \tag{4.20}$$

where μ_{ac} and μ_{bc} denote the dipole matrix elements of the respective transition and n_0 the atom number density.

From this we get the linear susceptibility for the probe laser

$$\chi^{(+)} = \frac{|\mu_{ac}|^2 n_0}{\varepsilon_0 \hbar} \times \left[\frac{4\Delta_p(\Omega_c^2 - 4\Delta_p^2 - \gamma^2)}{|\Omega_c^2 + (\Gamma + i2\Delta_p)(\gamma + i2\Delta_p)|^2} + i \frac{8\Delta_p^2\Gamma + 2\gamma(\Omega_c^2 + \gamma\Gamma)}{|\Omega_c^2 + (\Gamma + i2\Delta_p)(\gamma + i2\Delta_p)|^2} \right] . \tag{4.21}$$

The (+) indicates, that this formula will later be used for σ^+-polarized light. Furthermore, I have assumed that the coupling laser is always on resonance ($\Delta_c = 0$). Γ denotes the decay rate from the intermediate state, while γ is the decay rate between the two ground states, which corresponds to spin-changing collisions between the atoms as well as collisions with the background gas (which had been neglected so far). The real and imaginary part of the susceptibility are plotted in figure 4.4.

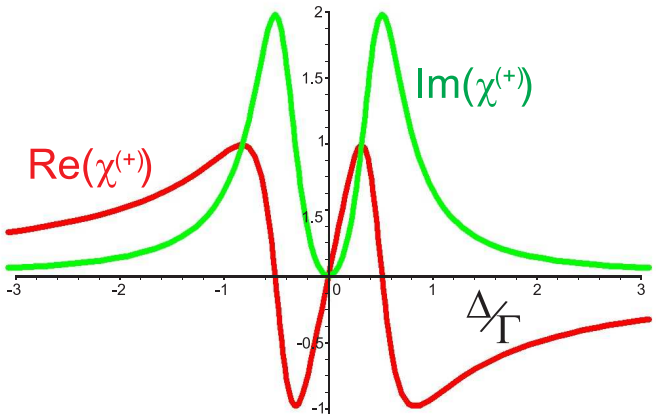

Fig. 4.4: Real and imaginary part of the susceptibility, plotted for $n_0|\mu_{ac}|^2/\hbar\varepsilon_0 = 1$, $\gamma = 0$ and $\Omega_c = \Gamma$. Under these conditions, the absorption cancels completely out on resonance. Independent from the conditions, the phase shift is always zero on resonance.

This formula describes the absorptive as well as the dispersive properties of the medium for the probe laser. The transmitted electric field is then given by

$$E_{out} = E_{in} \cdot \exp\left\{ikl\chi^{(+)}/2\right\} , \tag{4.22}$$

where l denotes the length of the medium and k the wave number. The relative intensity transmission (including the phase of the transmitted light) is then given by

$$T_r = \frac{E_{out}^2}{E_{in}^2} = \exp\left\{ikl\chi^{(+)}\right\} . \tag{4.23}$$

For a vanishing ground state decay rate and a non-vanishing coupling laser Rabi-frequency the medium becomes fully transparent on resonance ($\Delta_p = 0$).
To specify a transparency width it is convenient to approximate the transmission as a Gaussian around $\Delta_p = 0$

$$\mathrm{Re}\{T_r\} \approx \exp\left\{-\frac{\Delta_p^2}{\sigma_p^2}\right\} , \tag{4.24}$$

whose width is defined as

$$\sigma_p = \sqrt{\frac{\varepsilon_0\hbar}{|\mu_{ac}|^2 n_0 k l}} \sqrt{\frac{\Omega_c^4 + \gamma^2\Gamma^2 + 2\Omega^2\gamma\Gamma}{8\Gamma - 2\gamma(4\Gamma^2 - 8\Omega_c^2 + 4\gamma^2)/(\Omega_c^2 + \gamma\Gamma)}} \tag{4.25}$$

and reduces for a negligible decay rate γ to

$$\sigma_p = \frac{\Omega_c^2}{2}\sqrt{\frac{\varepsilon_0\hbar}{2\Gamma|\mu_{ac}|^2 n_0 k l}} . \tag{4.26}$$

The group velocity is associated to the derivative of the refractive index

$$n = \sqrt{1 + \mathrm{Re}\chi^{(+)}} \tag{4.27}$$

via

$$v_{gr}(\Delta_p = 0) = \frac{c}{n + \omega_p \frac{dn}{d\omega_p}\Big|_{\Delta_p=0}} = \frac{c}{1 + \frac{2\omega_p|\mu_{ac}|^2 n_0\, k l}{\Omega_c^2 \varepsilon_0 \hbar}} , \tag{4.28}$$

where I have used

$$\omega_p = \omega_0 + \Delta_p \Longrightarrow d\omega_p = d\Delta_p . \tag{4.29}$$

Comparison with equation 4.26 finally connects the group velocity with the experimental approachable magnitudes σ_p and l:

$$v_{gr} = \frac{c}{1 + \frac{c\,\Omega_c^2}{4\,l\,\sigma_p^2\,\Gamma}} \tag{4.30}$$

Therefore, the rapid change in the refractive index explains the strong reduction of the group velocity in EIT. Contrary to the two-level atom, it can theoretically be reduced to zero (for a vanishing decay rate γ).

4.3.1 EIT in the experiment

To reveal the dispersive properties of the medium, some σ^--polarized light is mixed to the otherwise σ^+-polarized probe beam. The relative electric field amplitude is denoted with a and thus the intensity admixture with a^2. Behind the atomic cloud, both polarizations are rotated to have the same linear orientation, so that they can interfere behind a polarizing beamsplitter. This setup is sketched in figure 4.5.

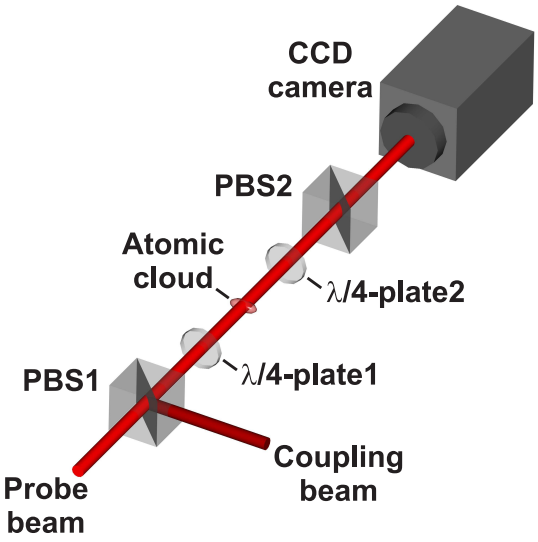

Fig. 4.5: Setup for revealing the dispersive properties of the medium. The probe and the coupling laser are overlapped in a polarizing beamsplitter (PBS). With the following $\lambda/4$-plate the polarizations of the pulses are adjusted before they enter the cloud. With the second $\lambda/4$-plate the polarizations are turned again to separate the probe from the coupling beam in the following polarizing beamsplitter. Due to lenses (not shown in the picture), the cloud is imaged onto a high efficiency CCD camera.

Due to birefringence in the optical viewports of the vacuum chamber, the σ^--polarized beam collects an additional phase ϕ relative to the σ^+-polarized beam. The total electric field acting on the atoms can then described by

$$\begin{aligned} |E_{in}|^2 &= |E_{in,\sigma^+} + E_{in,\sigma^-}|^2 \\ &= |(1-a)E_0 + aE_0 \exp\{i\phi\}|^2 \\ &= E_0^2 \left(1 - 2a + 2a^2 + 2a(1-a)\cos\phi\right) . \end{aligned} \tag{4.31}$$

As a high magnetic offset field is applied during these measurements, the atoms experience a large Zeeman-shift. Therefore, the σ^--polarized beam does not fulfill the Raman-condition and thus its susceptibility can be described by the two-level atom. As can be seen in figure 4.6, one has to sum over the susceptibilities of all four independent two-level systems, that can interact with the beam.

Due to the large detuning from resonance, absorption can be neglected ($< 0.04\,\%$ in our system), but the phase shift can become considerable.

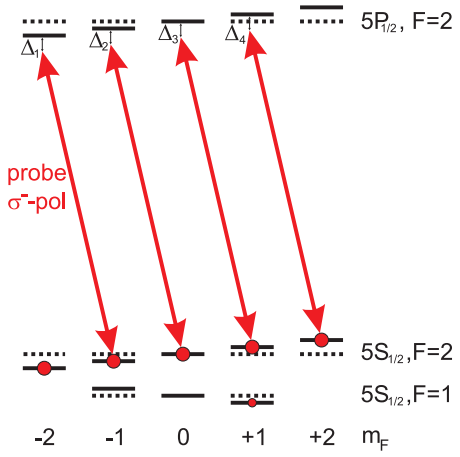

Fig. 4.6: Level scheme for the σ^--polarized component of the probe light: the detunings of the respective transitions j are marked as Δ_j. The dotted lines indicate the unshifted atomic levels and the solid lines the Zeeman-shifted levels.

The susceptibility of the σ^--polarized beam on one transition is given by equation 3.41 and therefore the susceptibility of all transitions becomes

$$\chi^{(-)} = \sum_{j=1}^{4} \frac{|\mu_j|^2 \, n_{0j}}{\hbar\epsilon_0} \, \frac{\Delta_j + i\frac{\Gamma}{2}}{(\frac{\Gamma}{2})^2 + \Delta_j^2} \, . \tag{4.32}$$

Here, n_{0j} are the population densities in the respective ground states, μ_j the dipole matrix elements and Δ_j the detunings relative to the respective transition, while the decay rate Γ is the same for all of them. The detunings Δ_j depend on the Zeeman shift of the atomic levels as well as on the probe detuning Δ_p.
The electric output field is then given by

$$\begin{aligned}
|E_{out}|^2 &= |E_{out,\sigma^+} + E_{out,\sigma^-}|^2 \\
&= \Big| E_{in,\sigma^+} \exp\{i\chi^{(+)} kl/2\} \\
&\quad + E_{in,\sigma^-} \exp\{i\chi^{(-)} kl/2\} \Big|^2 \\
&= \Big| (1-a) E_0 \exp\{i\chi^{(+)} kl/2\} \\
&\quad + a E_0 \exp\{i\phi\} \exp\{i\chi^{(-)} kl/2\} \Big|^2 \\
&= a^2 \exp\{-\mathrm{Im}\chi^{(-)} kl\} E_0^2 \\
&+ (1-a)^2 \exp\left\{ -\mathrm{Im}\chi^{(+)} kl \right\} E_0^2 \\
&+ 2a(1-a) \exp\left\{ -\left(\mathrm{Im}\chi^{(-)} + \mathrm{Im}\chi^{(+)}\right) kl/2 \right\} \\
&\quad \times \cos\left\{ \phi + \left(\mathrm{Re}\chi^{(-)} - \mathrm{Re}\chi^{(+)}\right) kl/2 \right\} E_0^2 \, .
\end{aligned} \tag{4.33}$$

It can be seen that the first two terms of equation 4.33 describe the usual transmission spectrum, described by the respective susceptibility, while the last term is responsible for the interference and results in the appearance of the dispersive properties of the medium.
Together with equations 4.21, 4.31 and 4.32, this yields the total transmission through the medium via

$$T_r(\Delta_p) = \frac{|E_{out}|^2}{|E_{in}|^2} \ . \tag{4.34}$$

Because we are probing the sample with relatively short pulses, the pulse length limits the minimal EIT bandwidth. The intensity of the Gaussian pulses is defined as

$$I(t) = I_0 \exp\left\{-\frac{t^2}{\tau^2}\right\} \ , \tag{4.35}$$

where τ denotes the Gaussian pulse length. To include this limitation, we first Fourier-transform the Gaussian pulse into frequency space (denoted by Δ)

$$F(\Delta) = \int_{-\infty}^{+\infty} I(t) \exp\left\{i2\pi\Delta\, t\right\} dt = I_0\sqrt{\pi}\tau \exp\left\{-\pi^2\tau^2\Delta^2\right\} \ , \tag{4.36}$$

and then carry out the convolution integral between this Fourier transformed pulse and the transmission (equation 4.34), which finally yields the transmission through the cloud:

$$T_{r,\,pulse}(\Delta_p) = \int_{-\infty}^{+\infty} T_r(\Delta') F(\Delta_p - \Delta')\, d\Delta' \tag{4.37}$$

Unfortunately, there exists no analytic solution to this integral. Thus, the integral has to be evaluated numerically, as it has been done in chapter 9.

4.4 Dark state polaritons and stored light

As mentioned above, mapping of light onto a collective atomic state, is accompanied by the creation of a quasi-particle, which is called a dark state polariton (DSP). Because the dynamics of these DSPs are not part of this thesis, I refer to the literature [FL00], [FYL00] and [FL02].
Here it shall be noted that the photonic state can be completely mapped onto the spin wave and afterwards transformed into light again. This can be used to store photons temporarily and transform them back to photons afterwards. However, due to short coherence times in atomic ensembles, the lifetimes of DSPs are still very short ($< 1\,\mathrm{ms}$) and long time storage of light is not yet achievable. The storage of light has first been demonstrated experimentally in a cloud of ultracold sodium atoms [LDBH01].

4.5 Coherent Population Trapping

Using strong lasers, where the number of photons exceeds the number of atoms, the complete population of an atomic ensemble can be transferred from one state to another. If this is done coherently, it is called coherent population trapping. To explain this effect, it is convenient to introduce the so-called dressed states. Assuming two-photon-resonance $\Delta_c = \Delta_p = \Delta$, we can define the two mixing angles θ and ϕ via

$$\tan(\theta) = \frac{\Omega_p}{\Omega_c} \tag{4.38}$$

$$\tan(2\phi) = \frac{\sqrt{\Omega_p^2 + \Omega_c^2}}{\Delta}\,. \tag{4.39}$$

Using these mixing angles, we can define new states, which are the eigenstates of the coupled atom-light system:

$$\begin{aligned} |\Psi^+\rangle &= \sin(\theta)\sin(\phi)|a\rangle + \cos(\theta)\sin(\phi)|b\rangle + \cos(\phi)|c\rangle \\ |\Psi^0\rangle &= \cos(\theta)|a\rangle - \sin(\theta)|b\rangle \\ |\Psi^-\rangle &= \sin(\theta)\cos(\phi)|a\rangle + \cos(\theta)\cos(\phi)|b\rangle - \sin(\phi)|c\rangle\,. \end{aligned} \tag{4.40}$$

Because $|\Psi^0\rangle$ doesn't contain any admixture of the excited state $|\mathrm{c}\rangle$, the atom does not scatter any light when being in this state. Thus, $|\Psi^0\rangle$ is a dark state.

As has been shown in [AT55], the states $|\Psi^\pm\rangle$ are shifted by the energy

$$\hbar\omega^\pm = \frac{\hbar}{2}\left(\Delta \pm \sqrt{\Delta^2 + \Omega_p^2 + \Omega_c^2}\right) \tag{4.41}$$

relative to the state $|c\rangle$, which is equivalent to an Autler-Townes-Splitting.

For further simplification we assume also one-photon-resonance $\Delta = 0$ (as we have done before) and get $\phi = \pi/4$.
Now we assume a strong coupling laser and a weak probe laser ($\Omega_c \gg \Omega_p$), which finally reduces equations 4.40 to

$$\begin{aligned} |\Psi^+\rangle &\approx \frac{1}{\sqrt{2}}(|b\rangle + |c\rangle) \\ |\Psi^0\rangle &\approx |a\rangle \\ |\Psi^-\rangle &\approx \frac{1}{\sqrt{2}}(|b\rangle - |c\rangle) \ . \end{aligned} \tag{4.42}$$

Now one can see, that the pure atomic state $|a\rangle$ is identical to the dark state $|\Psi^0\rangle$. Hence, all atomic population will be transferred into this state. An example for this is shown in figure 4.7.

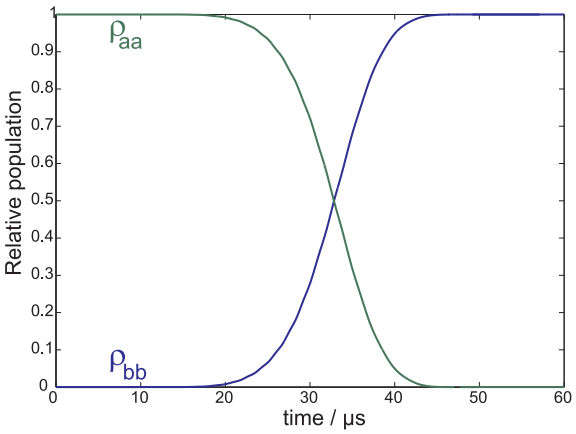

Fig. 4.7: Adiabatic transfer between two atomic states. ρ_{aa} equals the population in the first state, ρ_{bb} the population in the final state. The plot is created with maximum Rabi-frequencies of $\Omega_p = 2\pi \cdot 1.5 \cdot 10^6$ Hz and $\Omega_c = 2\pi \cdot 2.4 \cdot 10^6$ Hz.

If the laser intensities are varied until the opposite case is reached at $\Omega_p \gg \Omega_c$, the systems ends in the state

$$\begin{aligned} |\Psi^+\rangle &\approx \frac{1}{\sqrt{2}}(|a\rangle + |c\rangle) \\ |\Psi^0\rangle &\approx |b\rangle \\ |\Psi^-\rangle &\approx \frac{1}{\sqrt{2}}(|a\rangle - |c\rangle) \ . \end{aligned} \tag{4.43}$$

Thus, the atomic population has been transferred from state $|a\rangle$ to state $|b\rangle$. If this is done so slowly that the atoms can adiabatically follow the change in the light intensities [OHE84], it is a coherent process and therefore called coherent population trapping.

4.6 Stimulated Raman Adiabatic Passage

In section 4.5 we have assumed that there is enough light to transfer all atoms to the dark state. But this process can also be performed with weak laser pulses. Then, only some atoms will be transferred to the other state, but the complete photonic state can be mapped onto an atomic state.
This can be done when the laser intensities perform the STIRAP sequence, which is shown in figure 4.8.

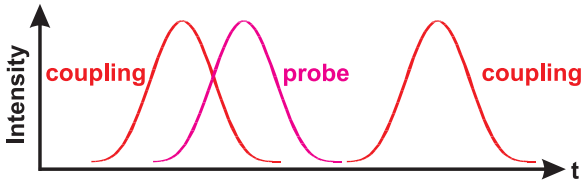

Fig. 4.8: The counterintuitive STIRAP pulse sequence of the coupling and the probe laser. Furthermore, the second coupling laser is shown. This additional pulse can be used to transfer the dark state polariton back to light.

Here, it is assumed that the atoms are initially in state $|a\rangle$, which is a dark state for the coupling laser. Nevertheless, the coupling laser is turned on first to ensure that the atoms stay permanently in the dark state. While it is slowly turned off, the probe laser is turned on and off again. The pulses are assumed to be Gaussian, which can e.g. be approximated as $\sin^4$-pulses [FSB97]. These are not infinitely long and resemble Blackman pulses [KC92]. An additional coupling laser pulse can be used to transfer the DSPs, which have been created in this process, back to light. This has first been experimentally demonstrated in cold molecules [GRSB90].

As mentioned before, the laser intensities have to be changed slowly. For a given pulse length $T_p \approx 4\tau$ (with τ being defined in equation 4.35), the adiabatic criterion is given by [KGHB89]

$$\sqrt{\Omega_c^2 + \Omega_p^2} \cdot T_p \overset{!}{\gg} 1 \,, \tag{4.44}$$

where Ω_c and Ω_p denote the maximum values of the respective Rabi-frequencies. The efficiency of this process can theoretically reach unity.

4.7 4-level atoms and offresonant scattering

In section 4.1, the level scheme of an atom was approximated with three levels. Of course, a real atom has far more states and some of these are also coupled to the laser fields. Figure 4.9 shows an example of further states, coupled by the probe and the coupling laser.

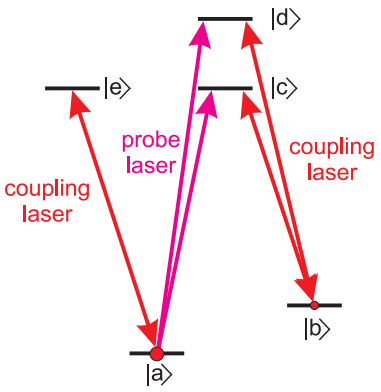

Fig. 4.9: Three atomic levels in Λ-configuration. Furthermore, the disturbing levels $|d\rangle$ and $|e\rangle$ are shown. The probe laser also couples to state $|d\rangle$, the coupling laser to states $|d\rangle$ and $|e\rangle$.

In this case, the Hamiltonian and density matrix can be extended to include these states. But the numerical calculation time for time-dependend Rabi-frequencies increases quadratically with the number of states. Instead, it is possible to assume the disturbance due to these levels to be small and calculate them seperately:
if the state $|c\rangle$ (figure 4.9) corresponds to the $|5P_{1/2}, F = 1\rangle$ state of rubidium 87, state $|d\rangle$ corresponds to the same magnetic substate of the $|5P_{1/2}, F = 2\rangle$ state. This state is then approximately 800 MHz detuned and scattering due to it can in EIT be neglected. But in a single photon detection scheme, the low scattering rate can become relevant. In this case it is possible to assume the perturbation of this transition on the other transitions to be small and calculate the scattering rate of the $|a\rangle$–$|d\rangle$ transition with the two-level approximation (see equation 3.39).

The level $|e\rangle$ in figure 4.9 corresponds to a different magnetic substate of the same excited state as $|c\rangle$. For EIT this can also be neglected because the detuning of this transition is usually very large. For single photon detection, this can again become important: the coupling laser can pump atoms on this transition to an undesirable ground state. As above, the scattering rate of this transition can then be calculated with the two-level approximation (see equation 3.39).

Part II

Experimental setup

5. Vacuum chamber

Using experimental values of previous experiments on optically trapped rubidium atoms [CRGW03], calculations on single photon detection were made before designing the chamber. These calculations showed the feasibility of the experiment and the chamber could then be designed to match the following demands:
For an optimimal transfer of the single photons onto the atomic state, a high Rabi-frequency is required. For a given atomic density, the Rabi-frequency and thus the transfer efficiency increase for an increasing optical path length through the cloud (see equation 3.21). This can be achieved by sending the laser along the long axis of an elongated cloud.
Furthermore, a high and homogeneous magnetic offset field must be applied during the optical pumping and the single photon transfer. This allows one to address the magnetic sublevels and defines a homogeneous quantization direction for the light vector.
Additionally, the unwanted atoms in the trap have to be removed with a magnetic field gradient. According to section 2.3.1 and appendix B, a higher atomic density can be obtained in a deeper trap for a given atom number. As a higher gradient can pull the atoms out of a deeper trap, the gradient should be as strong as possible.

It will be shown in the following sections how these requirements were accomplished in the design of the chamber. Figure 5.1 shows an evolution of the chamber design.

5.1 Dipole trap beams

A single beam dipole trap creates an elongated cloud, but then the single photons laser would have to be overlapped with the CO_2-laser, which is not possible because the ZnSe lenses and windows would absorb the single photons. But an elongated cloud can also be created in a crossed beam geometry. If the two beams meet under an angle of e.g. 60°, the cloud has a lower aspect ratio than in the single beam trap but a higher than in the perpendicular geometry.

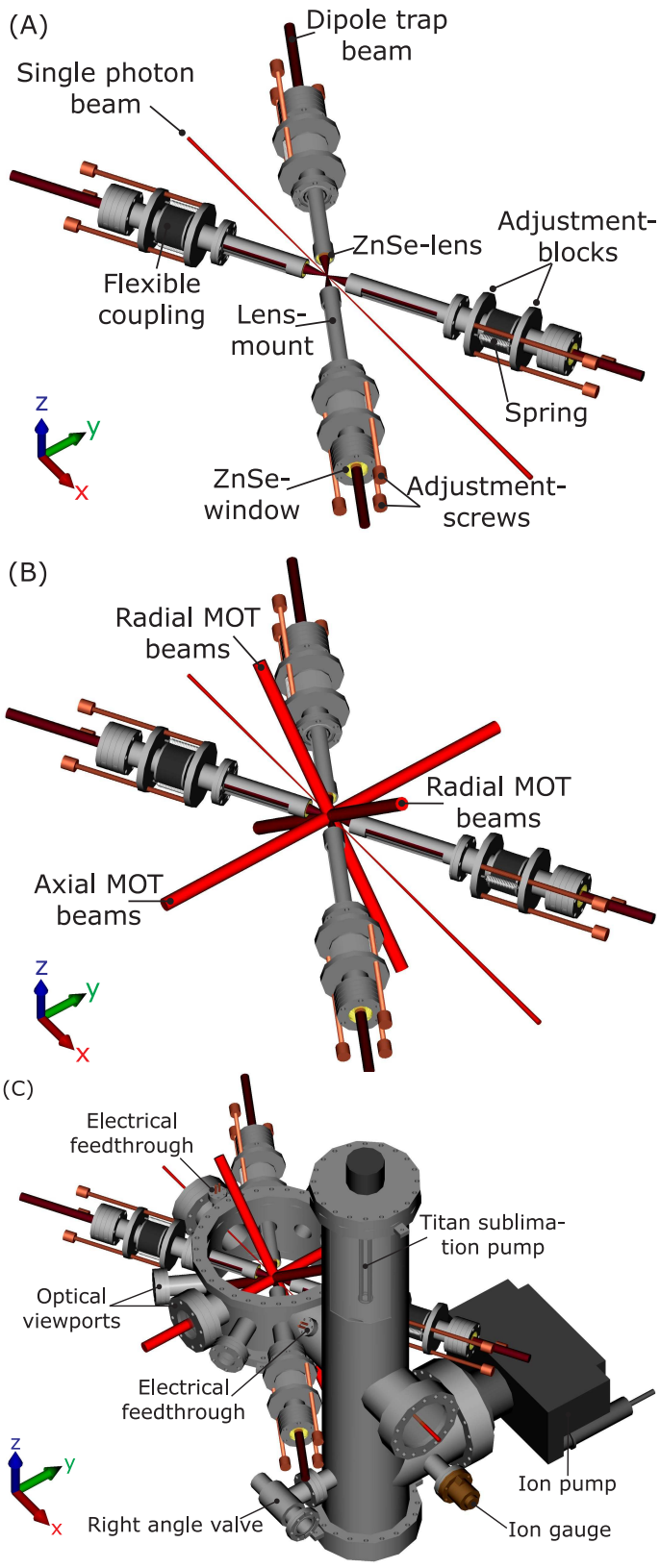

Fig. 5.1: The evolution of the vacuum chamber design:

(A) The first design step starts with the CO_2-laser beams and the path of the single photon.

(B) Subsequently, the optical access for the MOT beams is reserved. The radial and axial MOT beams refer to the orientation of the magnetic quadrupole field (created by the coils shown in figure E).

(C) Then, necessary viewports and the main chamber, which is circular around the z-axis, are put around the trap center and the pumping cross is attached to them.

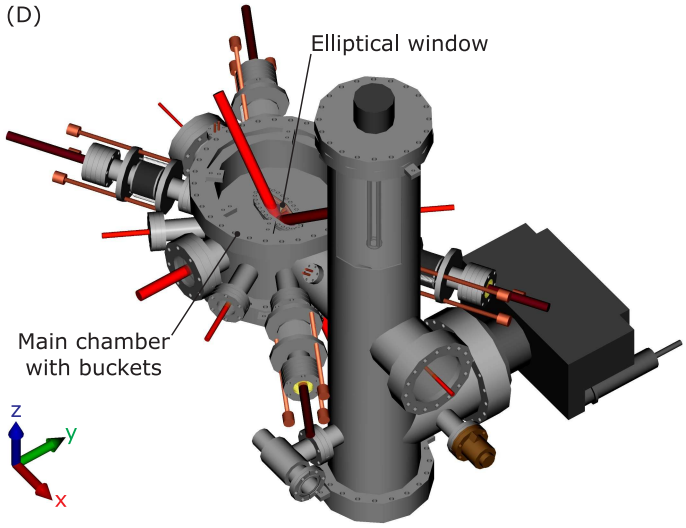

(D) The buckets and elliptical windows are mounted to the chamber.

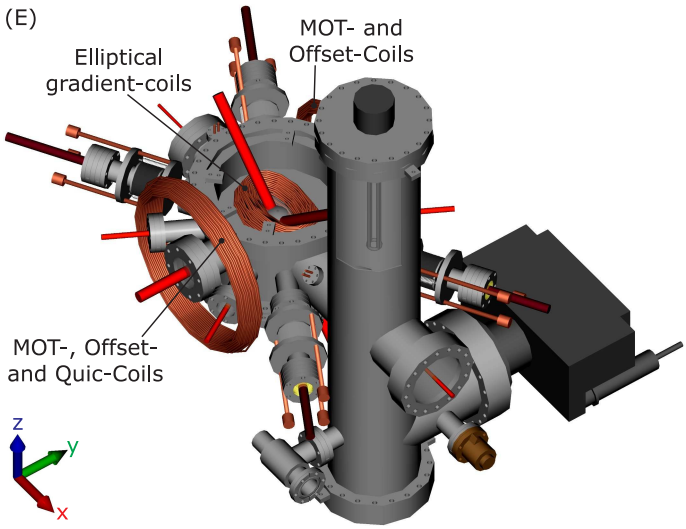

(E) The magnetic coils are attached to the chamber.

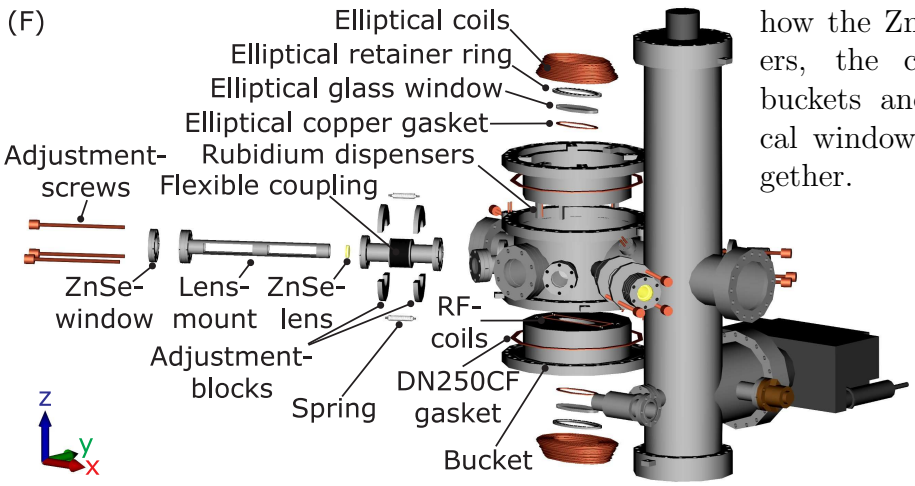

(F) An exploded view of the chamber. It shows how the ZnSe lens holders, the chamber, the buckets and the elliptical windows are put together.

As the ZnSe lenses must be very close to the trap center to focus the dipole trap beams tightly (due to the large wavelength) and thus block other optical ports, the design of the chamber starts with the light course of the CO_2-laser.
For the path of the single photon beam that leads through the space between the two lenses, we will reserve an angle of $\sim 2 \cdot 7° = 14°$. Since the ZnSe lenses require a mounting device, some additional space ($2 \cdot 3°$) will be lost. When we assume an angle of $2 \cdot 30° = 60°$ between the two CO_2-laser beams, we get an opening angle for the CO_2-laser beams of $\sim 2 \cdot 20°$, which equals a ratio between the lens diameter and the focusing length of $\sim 2/3$. If the angle between the CO_2-laser beams is increased, the ratio between the diameter of the ZnSe lens and its focusing length can be increased. This leads to larger trap frequencies, but also lowers the aspect ratio of the cloud. If the angle between the CO_2-laser beams is decreased, the ratio between the diameter of the ZnSe lens and its focusing length must be decreased. This leads to a larger aspect ratio of the cloud, but also lowers the trap frequencies. Hence, the choice of 60° states a good compromise. The opening angle can be achieved with a lens diameter of 25.4 mm (=1 inch) and a focusing length of 38.1 mm (=1.5 inch). Because the two CO_2-laser foci must be aligned exactly and vacuum chambers cannot be produced that precisely, the ZnSe lenses must be attached to a movable mount that can be adjusted from outside the chamber. These mounts are shown in figure 5.1 A: the mount is welded to a double-sided DN 40CF flange. On its inside, this flange is screwed on a flexible coupling (bellow), which will be mounted on the chamber. Three adjustment screws in a rectangular alignment can be used to move the lens inside the vacuum, while two strong springs between the adjustment blocks (squeezed on the bellows) create the required stability. The springs, which are not shown in the figure, are streched parallel to the adjustment screws. The vacuum is maintained by ZnSe windows, which are screwed on the outside of the lens mount. The assembly of all these parts can be seen in figure 5.1 F.

5.2 MOT beams

Although there is enough space for the tightly focused single photon beam between the ZnSe lenses, there isn't enough space for sufficiently large MOT beams. The only remaining axis in this plane is orthogonal to the single photon beam. These MOT beams, which are referred to as axial beams, are shown in figure 5.1 B. Then, the radial beams must be orthogonal to the axial beams, with the maximum angle of 45° between them and the single photon beam. The ZnSe lenses are then still a limiting factor for the size of the MOT beams ($\varnothing \approx 2\,\text{cm}$).

5.3 Viewports and pumping cross

Now, the viewports, through which the single photon and the axial MOT beams enter the chamber can be placed (figure 5.1 C). Because there is enough space, DN 63CF flanges can be used. The least used port (exit window of the single photon beam) will be used to attach the pumping cross and thus the remaining space in the mayor plane can be filled up with DN 35CF viewports. These viewports can e.g. be used to image the cloud onto a CCD camera. The angle between any of the twelve viewports is 30°.
The pumping cross consists of 160 mm tubing, which is connected to the main chamber via 120 mm tubing, to ensure a proper pumping cross section. A larger cross section would hinder the radial MOT beams from entering the chamber. The top part of the pumping cross contains a titanium sublimation pump (Varian TSP cartridge filament source), which is far enough away to prevent sputtering titanium on the viewports. An ion pump (Varian starcell 75) and an ion gauge (Varian UHV-24 Nude Bayard-Alpert) are attached to a tubing that is placed rectangular on the bottom of the main pumping tubing to avoid getting damaged by sputtering titanium. The optical access to the chamber is given by a DN 100CF viewport.
At the bottom of the pumping cross is a right angle valve to attach a turbomolecular pump. Remaining space along the connection between the pumping cross and the main chamber as well as the space between the main chamber and the viewport for the single photon beam were filled up with DN 16CF flanges. They are used for electrical feedthroughs that are connected to the rubidium dispensers and the RF coils in the chamber.

5.4 Elliptical windows and magnetic coils

To seal the main chamber along the z-axis, two buckets will be put into the main chamber (see figures 5.1 A and 5.1 E and section 5.5). The buckets contain an elliptical viewport, which must be very close to the trap center to provide a large solid angle, from which the fluorescence light of the single atoms will be collected. To provide optical access for the radial MOT beams, this viewport has to be large along the x-axis (figure 5.1 E).
To perform the required $\Delta m_F = +1$ transition, the single photon and the coupling laser must be orthogonal to each other. It is possible to use the states $|5P_{1/2}, F = 1, m_F = -1\rangle$, $|5P_{1/2}, F = 2, m_F = -1\rangle$, $|5P_{1/2}, F = 1, m_F = 0\rangle$ and $|5P_{1/2}, F = 2, m_F = 0\rangle$ as the intermediate state. As the Clebsch-Gordan-coefficient is highest for the $|5S_{1/2}, F = 1, m_F = -1\rangle$–$|5P_{1/2}, F = 2, m_F = -1\rangle$ transition, the $|5P_{1/2}, F = 2, m_F = -1\rangle$-state will be used as intermediate state.

This ensures the maximum possible optical density for the single photon (the coupling laser intensity can simply be increased). To use these transitions, the single photon laser beam must be π-polarized, while the coupling laser is σ^--polarized.
Thus, the coils, which create the magnetic offset field, must be placed to create the field along the y-axis (figure 5.1 E). These coils can also be used to create the quadrupole field for the MOT. The chosen position is the closest one to the trap center, as all possibly closer positions are blocked by viewports. An additional coil is attached to the MOT coil in the foreground (QUIC-coil, see section 6.4).
Because it is easiest to apply a gradient along an offset field (instead of orthogonal to it), the gradient coils can be put into the buckets. This is also the place, where they can get closest to the trap center and create the highest possible gradient. The part of the coils, which runs parallel to the x-axis is then responsible for producing the gradient along the y-direction. To increase the gradient, this part of the coils must then be close to the trap center, while the other part must be far away to provide optical access for the radial MOT beams.
This leads to elliptical coils, which are put on top and around an elliptical window. Futhermore, the elliptical coils have to 'open' under an angle of 45° from inside to outside while viewed from the bottom of the bucket to the top of the coils. In other words, they are wrapped around the 45° MOT beams.

5.5 Buckets

Figure 5.2 shows a bucket from the bottom side: the rubidium dispensers, which contain solid rubidium (that is evaporated by electric heating and used as the atomic source), are screwed onto mounts, which are welded on the upper of the two buckets. Furthermore, there are several mounting brackets (semicircle-shaped metal rings with $r = 2\,\mathrm{mm}$) welded on the inner sides of the buckets. These are used to mount RF-coils and the supply lines of the rubidium dispensers, as it is shown for one of the dispensers. The RF-coils (two on the upper and two on the lower bucket in Helmholtz-configuration) might for example be used for evaporative cooling in the Quic trap (see sections 2.5 and 6.4).

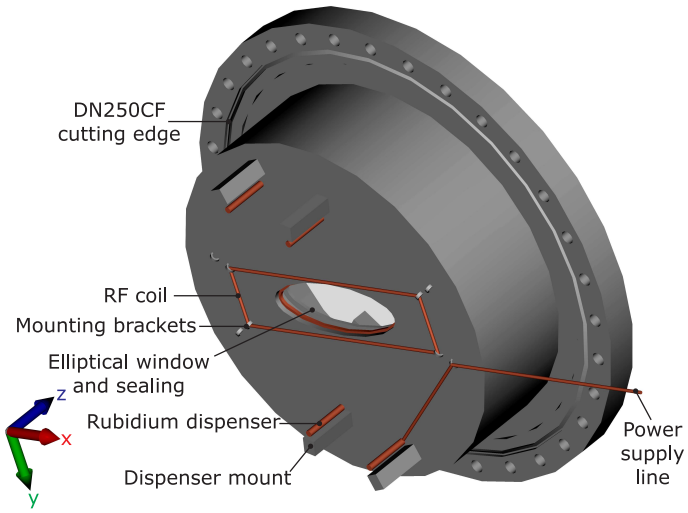

Fig. 5.2: Bottom view of a bucket. The rubidium dispensers, the RF coils and one supply line can be seen. When the buckets are mounted to the chamber, the distance between their bottoms is 36 mm.

The assembly of the bucket and the chamber can be seen in figure 5.1 F.

5.6 Elliptical sealing

Only for circular CF flanges, high vacuum sealings are commercially avaible. The buckets already provide an elliptical analogon to a CF flange cutting edge (custom made by TRINOS, the company that welded the whole chamber). Hence, an elliptical copper sealing had to be made, as it has been described in [NK94]. This sealing uses a copper ring, which is flat on one side and has a cutting edge on the other side. Here, the CF cutting edge is pressed into the flat side of the copper ring and the glass window is pressed onto the cutting edge of the copper ring.
But this works only with small radii [Pet05, Ada06]. Furthermore, the elliptical copper rings had to be milled instead of turned. This resulted in tiny scratches, which were perpendicular to the copper cutting edge and a minimum vacuum pressure of 10^{-6} mbar could be produced (with the turbo-molecular pump). To bypass this problem, a new kind of copper sealing had to be made. This is sketched in figure 5.3.
The semi-major axis of the elliptical window is 52 mm and the semi-minor axis 21.9 mm to leave space between the window and the slightly larger containing ring (52.1 mm and 22.1 mm, respectively). The window is made of anti-reflex coated BK7 glass and only 6 mm thick (this is the minimum thickness required to prevent the glass from breaking). 52 M4-screws are distributed around the ring to allow for smooth tightening.

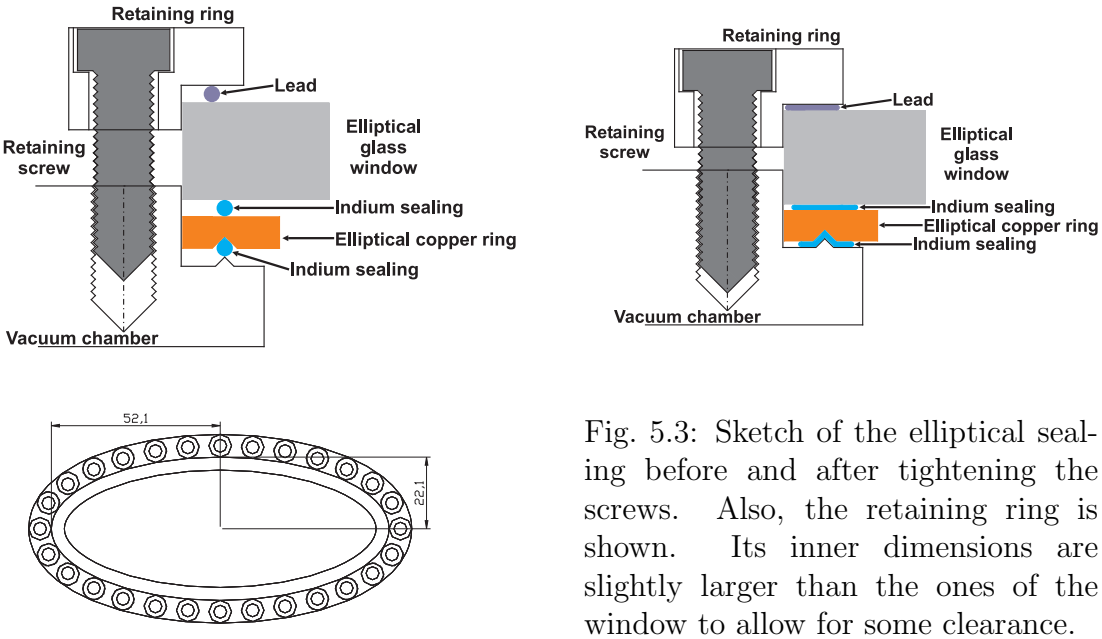

Fig. 5.3: Sketch of the elliptical sealing before and after tightening the screws. Also, the retaining ring is shown. Its inner dimensions are slightly larger than the ones of the window to allow for some clearance.

A main part of the sealing is a copper ring with a triangular goose, that is slightly larger than the CF cutting edge on the vacuum chamber. It has to be larger to ensure that the cutting edge does not hit the copper ring. This would cause leaks for low clamping forces.

We place an indium ring into the goose and a second one on the other side of the copper sealing. After slowly tightening the screws in a crossed pattern to a maximum of 2 Nm, the first indium ring seals between the copper ring and the chamber, the second one between the copper ring and the window. The lead ring (modulus of elasticity $E \sim 18\,\mathrm{GPa}$) compensates local variations in the clamping force.
The advantage of this method is that the cutting does not have to be pressed into relatively hard copper ($E \sim 117\,\mathrm{GPa}$). Instead, we only have to squeeze the soft indium ring ($E \sim 10\,\mathrm{GPa}$).

Using a helium leakage tester, we measure leakage rates of $10^{-10}\,\mathrm{mbar \cdot l/s}$ for each of the two elliptical windows at our UHV chamber. After baking the chamber for three weeks at 150°C (higher temperatures are not possible as the indium sealing melts at 157°C), we pump with an ion pump (Varian starcell 75) and a titanium sublimation pump (Varian TSP cartridge filament source) and measure a pressure of $10^{-10}\,\mathrm{mbar}$ with an ion gauge (Varian UHV-24 Nude Bayard-Alpert). Together with the pumping cross-section of the chamber, this pressure also corresponds to a leaking rate of $10^{-10}\,\mathrm{mbar \cdot l/s}$ and supports the helium-measured leaking rate.

5.7 Framework

As can be seen in figure 5.4, the whole chamber is finally supported by a framework of aluminium bars and breadboards. These are used to mount optics, the magnetic coils, the CCD cameras and supply lines around the chamber.

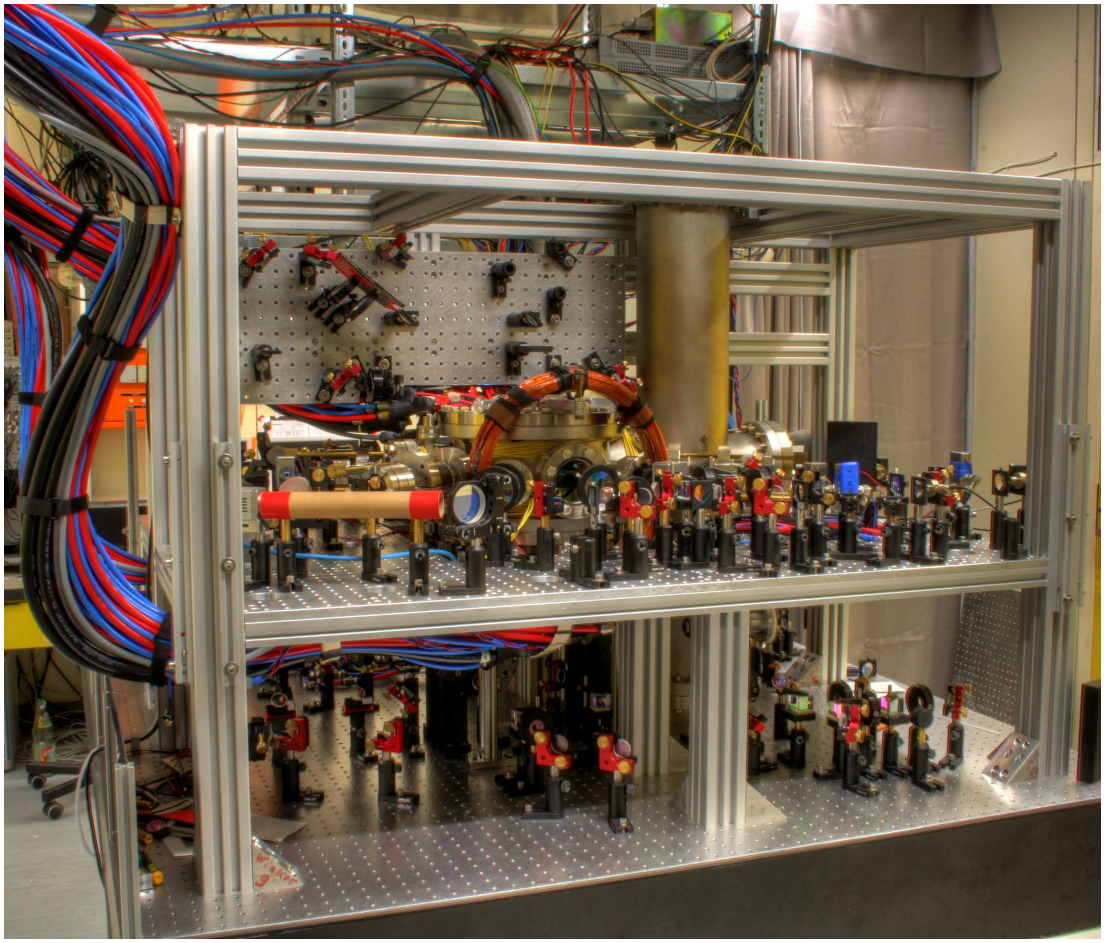

Fig. 5.4: Picture of the final chamber. An aluminium framework, that holds all the optics, is placed around the chamber.

6. Magnetic fields

In this chapter, the details of the magnetic coils and the fields produced by them will be given. This includes the field for operating the MOT, the offset field for the single photon detection, the magnetic gradient for pulling the atoms out of the dipole trap and the field for capturing the atoms magnetically in the Quic trap.

All magnetic coils have been wound with hollow copper wire, whose inner tube is used for water cooling. The outer wire diameter is 3 mm and the inner one 1.5 mm. Because the water flow gets too low to cool the coil sufficiently after about 7 windings, the coils consist of several sub-coils. While the electric current runs serial through all sub-coils (to ensure a stable current and field), the water flows parallel through the sub-coils. The coils are designed to carry maximum currents of 250 A. With a voltage of 60 V (maximum of the power supplies, type Lambda/Emi ESS60-250), a current of 170 A could be achieved. At these operating conditions, the temperature in the coils increases to a maximum of 60°C (at a water pressure of ~ 5 bar and a water temperature of ~ 12°C). The currents are all switched with IGBTs (switching time < 1 ms). The direction of the currents in the individual coils can be seen in figures 6.1 and 6.2.

6.1 MOT field

The magnetic field gradient for the MOT is created by the two MOT coils (which are also used for the offset field), shown in figures 5.1 E, and 6.1. Their average radius is 149 mm and their average distance from the trap center 152 mm. With the maximum current of 170 A, the gradient at the trap center is 16.9 G/cm along the y-axis and 8.45 G/cm along the x- and z-axes.

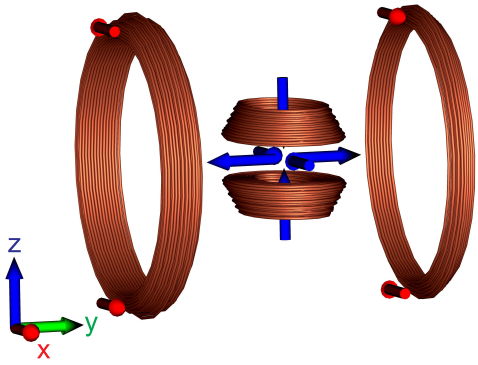

Fig. 6.1: The direction of the electric currents for creating the magnetic quadrupole field required for the MOT is shown with red arrows, the direction of the magnetic field in the trap center with blue arrows. It can be seen that the coil on the left contains more windings. The additional windings can be used to enhance the confinement in the Quictrap (see sections 2.5 and 6.4).

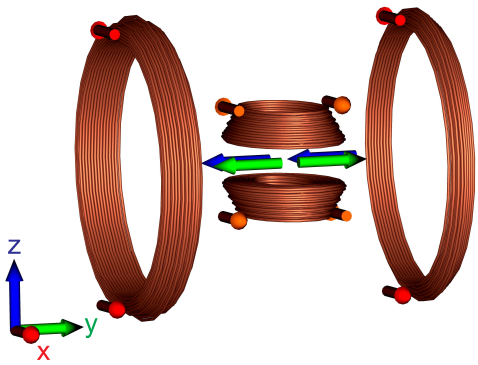

Fig. 6.2: The direction of the electric currents for creating the magnetic offset field is shown with red arrows, the direction of the magnetic offset field in the trap center with blue arrows. The currents for creating the magnetic gradient (see section 6.3) are shown with brown arrows and its field with green arrows. The resulting field is shown in figure 6.3.

6.2 Offset field

A high and homogeneous magnetic offset field is required for optical pumping and the single photon transfer. This offset field is created by the same coils as used for the MOT. The current direction of the coil in the foreground (figures 5.1 E, and 6.2) flows in the same direction as for the MOT, while the current direction in the other one is switched. The chosen offset field of 100 G can be obtained with a current of 102 A. With the maximum current of 170 A, the offset field can be increased up to 167 G. Due to the size of the coils, the curvature of the field and the change in the field direction are negligible over the size of the cloud.

6.3 Gradient field

To pull the atoms out of the optical dipole trap, a strong magnetic gradient is required. This gradient must be applied parallel to the magnetic offset field. It is created by the elliptical coils, shown in figures 5.1 E and 6.2. With the maximum current of 170 A, the gradient at the trap center is 380 G/cm.

The absolute value of the magnetic field is shown in figure 6.3 with an offset field of 100 G.

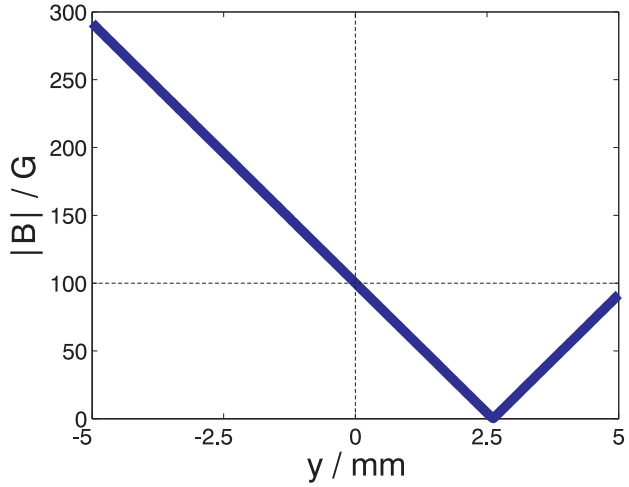

Fig. 6.3: The gradient, that pulls the atoms out of the trap. The atoms are collected in the field minimum, that is 2.5 mm away from the trap center. Once the field is switched off, the atoms are lost.

Figure 6.4 shows the potential for magnetically neutral atoms in the crossed dipole trap (see section B) with an optical power of 570 mW (see section 8.1) in each beam, as well as the potential for atoms in the $|5S_{1/2}, F = 1\, m_F = -1\rangle$ state in the same dipole trap with applied magnetic field gradient. It can be seen that the magnetic potential opens the trap and the atoms get lost.

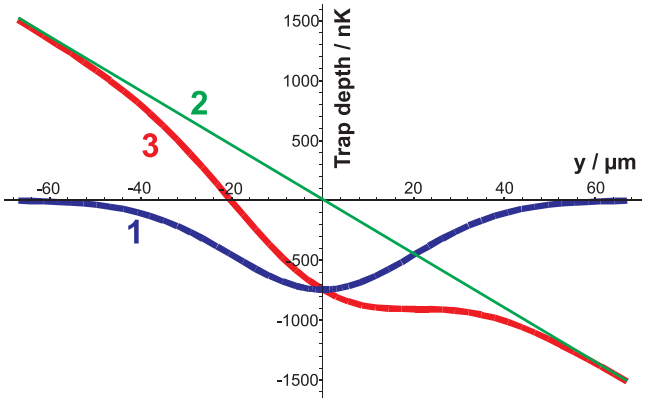

Fig. 6.4: Potential for magnetically neutral (1, blue) and magnetically sensitive (3, red) atoms and the magnetic gradient field (2, green). The neutral atoms remain in the dipole trap, the sensitive ones are pulled out of it.

6.4 Quic trap

The experiment also provides a magnetic trap. Due to the existing coils, the so-called Quic-trap [EBH98] has been chosen. Here, the opposing coils create a quadrupole field and the field of a third coil, that is arranged orthogonal to the others, is slowly increased to transfer the atoms into a Ioffe-type trap [Pri83]. To create the quadrupole field, the elliptic gradient coils are used in anti-Helmholtz configuration, as they are used for pulling the atoms out of the dipole trap (see figure 6.2 and section 6.3). The dipole coil on the left (figure 6.2) can be used as the third coil. As the dipole coil is the limiting factor for the trap, an additional coil has been mounted on it. Then, the maximum current of 170 A can be sent through the double coil and keep up with a current of 30 A through the much stronger elliptical coils. The field created by this setup is shown in figure 6.5.

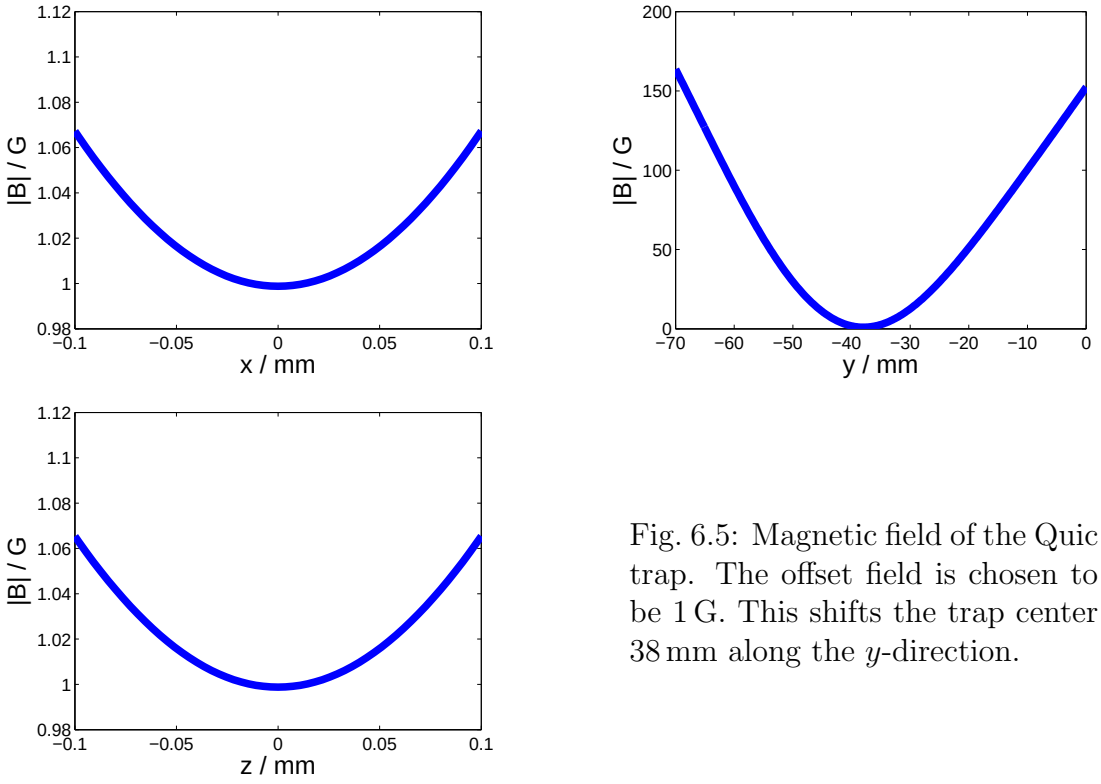

Fig. 6.5: Magnetic field of the Quic trap. The offset field is chosen to be 1 G. This shifts the trap center 38 mm along the y-direction.

With these currents, the trap frequencies are $\nu_x = 34\,\mathrm{Hz}$, $\nu_y = 5\,\mathrm{Hz}$ and $\nu_x = 33\,\mathrm{Hz}$. Especially the trap frequency in y-direction is very low and it should be noted that this kind of trap was only included to make the chamber more flexible for further experiments.

7. Laser systems

Here, all relevant information on the setup of the MOT and repumping laser system, the Raman laser system and the CO_2-laser system will be given.

7.1 MOT and repumping laser system

The laser system for operating the MOT consists of two individual laser systems, one for the MOT transistion and one for the repumping transition. They connect the $|F = 2\rangle$ ground state, respectively the $|F = 1\rangle$ ground state with the excited $|5P_{3/2}\rangle$ states. As there is enough optical power available, the lasers are also used for the optical pumping, absorption imaging and the single atom detection. These laser systems are shown in figure 7.1.

The setup for both laser systems is similar: a weak part is split from the main beam of a grating-stabilized diode laser (M1, M2). This part enters a rubidium vapor cell. The signal behind the cell is used for stabilizing the laser. The setup of such a cell can be found in [PFL+03].
Another weak part is split up for analyzing the beam in a wavemeter and a Fabry-Pérot-interferometer.

Subsequently, both lasers enter an acousto-optical modulator (AOM) in double-pass configuration. This AOM (Crystal Technology) has a very large bandwidth of $\pm 50\,\mathrm{MHz}$ and allows for a wide detuning of the beam without moving it.

After these AOMs, the beam of the MOT laser system injects a tapered amplifier (TA) while the beam of the repumping system seeds another diode laser. The advantages of the tapered amplifier are its enhanced optical power (we use it at $600\,\mathrm{mW}$) and its wide frequency spectrum.

The amplified beams finally pass through $\lambda/2$-plates and polarizing beam-splitter cubes (PBS). These split up the beams for the different tasks, like e.g. the optical pumping. The single beams pass through AOMs, before they are fed

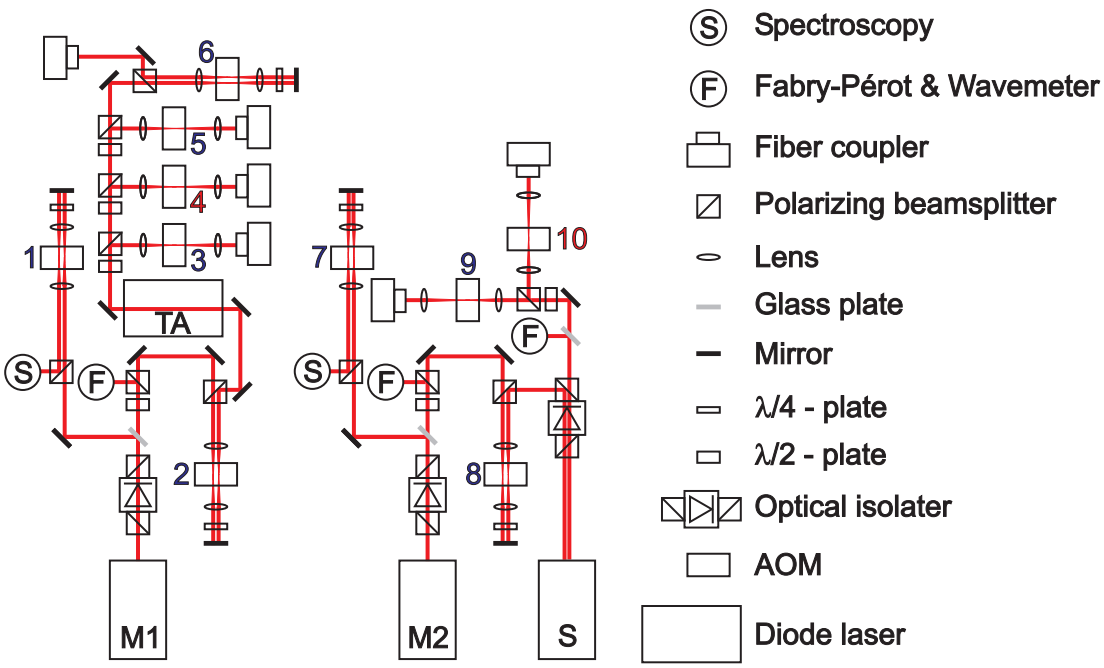

Fig. 7.1: Schematic of the MOT (left) and the repumping laser system (right), consisting of the respective master lasers M1 and M2, the tapered amplifier (TA) and the slave laser S. AOM 3 switches the light that can be used for taking absorptive pictures of the cloud, AOM 4 switches the light for optical pumping, AOM 5 the light for operating the MOT and AOM 6 the light for the single atom detection. AOM 9 switches the repumping light for operating the MOT and AOM 10 the repumping light for the optical pumping. The frequencies of the AOMs are:

$f_1 = +105\,\mathrm{MHz}$; $f_2 = +200\,\mathrm{MHz}$; $f_3 = +140\,\mathrm{MHz}$; $f_4 = -80\,\mathrm{MHz}$;
$f_5 = +140\,\mathrm{MHz}$; $f_6 = +160\,\mathrm{MHz}$; $f_7 = +105\,\mathrm{MHz}$; $f_8 = +200\,\mathrm{MHz}$;
$f_9 = +60\,\mathrm{MHz}$; $f_{10} = -130\,\mathrm{MHz}$

into optical fibres, which bring them to the experiment. All AOMs have different frequencies, depending on the required frequency of the respective beam and are used for switching the lasers. Figure 7.2 shows a picture of the laser systems, while the optical path of the lasers at the experiment is sketched in figure 7.4.

7.2 Raman laser system

The Raman laser system is used for measurements on electromagnetically induced transparency and will be used for the single photon detection. As no deterministic

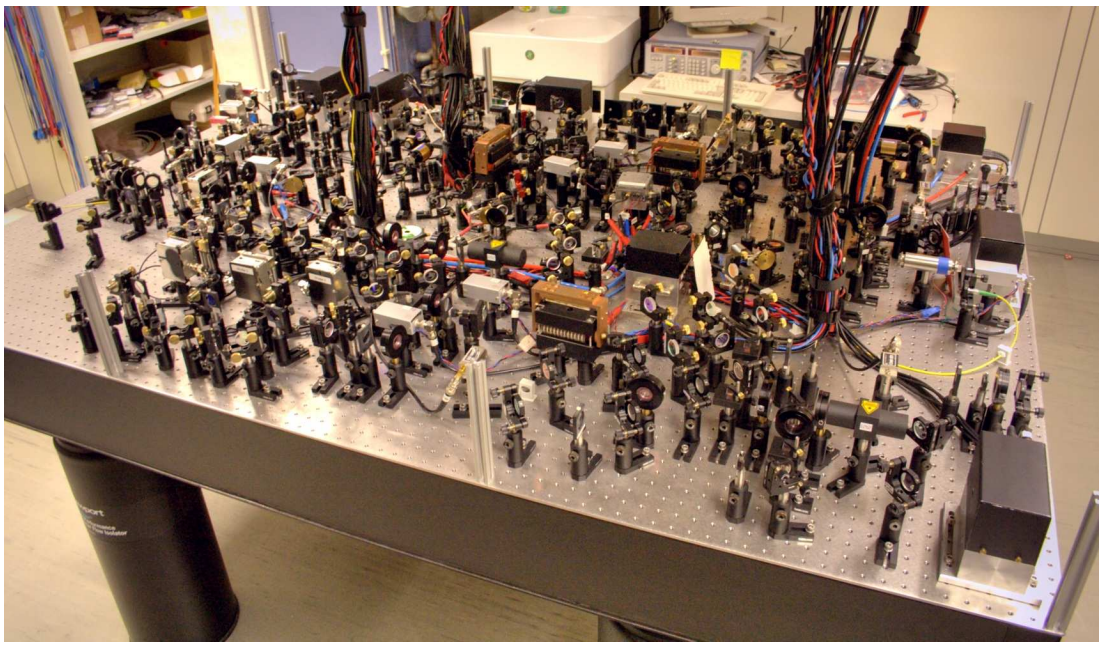

Fig. 7.2: Picture of the laser systems. The laser system for operating the MOT is in the foreground of the picture, the repumping laser system on the right in the background and the Raman laser system is on the left in the background.

single photon source is available, the single photons will be created by decreasing the power of the probe beam, which yields Poisson-distributed pulses (see appendix E). To perform a Raman transition in ultracold atoms, the difference in the two laser frequencies must be stable within the kHz-range because the ground states have very narrow linewidths.

The stable frequency difference of 6.8 GHz is created by passing the light through a 1.7 GHz AOM in quad-pass configuration (see figure 7.3):
the light of a grating-stabilized master laser (same spectroscopy as in the MOT laser system) passes through a Faraday isolator and subsequently through a polarizing beamsplitter cube and an AOM at 1.7 GHz. The light is reflected after it passes through a $\lambda/4$-plate and is thus reflected at the PBS. Due to the low efficiency of the AOM ($\sim 8.5\,\%$ in the single pass), only $160\,\mu$W laser power is left. Thus, the light is amplified by injecting a slave laser. The light of this laser goes exactly in the opposite direction of the first beam. Thus, it passes twice through the 1.7 GHz AOM, and is reflected at the beamsplitter cube of the Faraday isolator. This light has been shifted -6.8 GHz relative to the light of the master laser and is used to inject a second slave laser. The light of the second slave laser and the zeroth order of the master laser beam at the 1.7 GHz AOM are used as slave- and coupling laser, respectively.

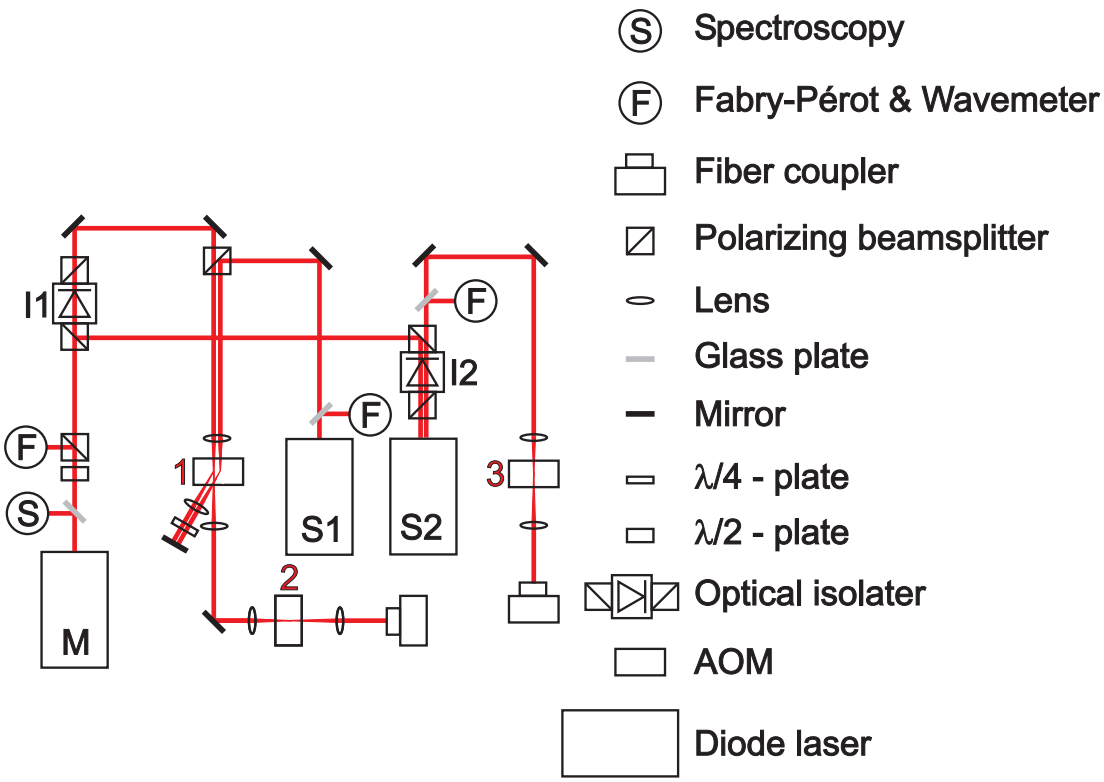

Fig. 7.3: Schematic of the Raman laser system, consisting of the master laser M, the intermediate slave S1 and the final slave S2. The frequencies of the AOMs are $f_1 = -1.709\,\text{GHz}$ and $f_2 = f_3 = -91\,\text{MHz}$ for the single photon detection, while the latter one is $f_2 = f_3 = +91\,\text{MHz}$ for the EIT measurements.

For switching them, the beams pass through AOMs, before they are fed into optical fibres, that transfer the light to the optical table. The radio frequency of these two AOMs comes from the same driver to ensure the high frequency stability. The optical path of the probe and coupling lasers at the experiment is sketched in figure 7.4.

7.3 CO_2-laser system

A Coherent GEM 100L CO_2-laser, that produces up to 130 W is used to create the optical dipole trap. Its beam is split into two equal parts for the crossed dipole trap. Each of the beams passes through an AOM, that is used to control the intensity of the beam. Subsequently, the beams are expanded to a diameter of 16 mm before they enter the chamber. Each AOM needs an RF power of 30 W. This power heats up the AOM and when the RF power is ramped down

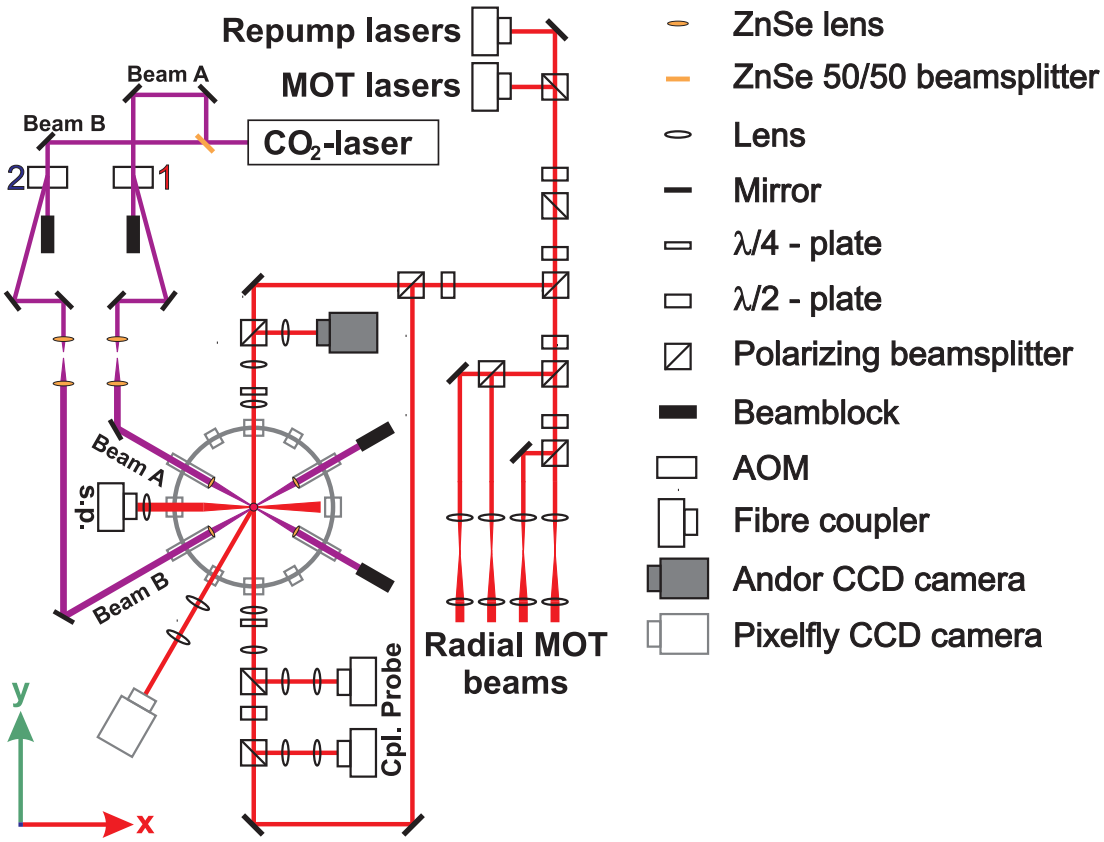

Fig. 7.4: Schematic of the CO_2-laser system and the setup for measurements around the chamber. It can be seen how the MOT lasers, the coupling and the probe laser are overlapped. Furthermore, the future path of the single photon (s.p.) is shown. The frequencies of the AOMs in the CO_2 beams are $f_1 = +30/+50\,\mathrm{MHz}$ and $f_2 = -30/-50\,\mathrm{MHz}$. They have an opposing algebraic sign to prevent interference effects in the dipole trap.

to decrease the laser intensity, the AOM cools down and the beam moves. To overcome this shortcoming, a second frequency with 50 MHz is added to the used frequency of 30 MHz. This created an additional beam behind the AOM, which can be neglected, as it is blocked. Using an electronic circuit, the power of the second frequency is adjusted to keep the total RF power constant at 30 W. Then, the beam does not move when the power is reduced.

7.4 Setup for the measurements

Figure 7.4 also shows the complete laser setup around the chamber in 2 dimensions and the radial MOT beams, which are sent under an angle of 45°

into the chamber (see figure 5.1 B). It is also shown how the probe and the coupling laser are overlapped with the MOT beams to ensure the respective polarizations. A high efficiency Em-CCD camera (Andor iXon) is used to perform absorption measurements of the cloud, using the Raman laser system. λ-plates and polarizing beamsplitter cubes are used to ensure that only the desired lasers arrive at the camera. Using the lenses, the cloud is imaged onto the camera.

Analogously, lenses are used to image the cloud onto a CCD camera (PCO Pixelfly), which is used for fluorescence measurements of the cloud.

As the single photons will need to be π-polarized, they will enter the chamber along the x-direction. The directions are the same as in figures 5.1.

Before the MOT lasers, which are overlapped with the repumping lasers, enter the chamber, they are expanded to a diameter of 10 mm, with a power of 20 mW in each beam. The overlapped repumping laser beams have an intensity of 1 mW each.

Part III

Calculations

8. Single Photon Detection

After the vacuum chamber and thereto fitting magnetic coils had been designed, precise calculations on single photon detection could be made. The properties of the atomic cloud, that were expected due to the design of the chamber, were used to perform these calculations, which are presented in this chapter.

For the single photon detection process, we continue sticking to single photon Fock states and neglect states with two or more photons, as they can in principle be calculated the same way.

There are then two different efficiencies in the single photon detection process:

- a single photon arrives, but is not detected (η_{1pd})
- no photon arrives but the detector counts one (η_{0pd})

The first case can occur if the single photon transfer is insufficient η_{ipt}, the single photon has the wrong polarization η_{wp}, the single atom changes its state due to a collision when the other atoms are pulled out of the trap η_{col}, if the single atom decays into the wrong state during its detection process η_{ws} or if the single atom is lost due to the finite lifetime η_{lt} in the trap.

$$\eta_{1pd} = (1 - \eta_{ipt}) \cdot (1 - \eta_{wp}) \cdot (1 - \eta_{col}) \cdot (1 - \eta_{ws}) \cdot (1 - \eta_{lt}) \tag{8.1}$$

The second case can occur when an atom is initially in a magnetic $|\mathrm{m_F} = 0\rangle$ substate $\eta_{m_F 0}$ or gets there by scattering light of the coupling laser η_{cls}

$$\eta_{0pd} = (1 - \eta_{m_F 0}) \cdot (1 - \eta_{cls}) \ . \tag{8.2}$$

8.1 Adiabatic transfer

The scheme of the adiabatic transfer is shown in figure 8.1. Here, the atoms have all been collected in the $|5\mathrm{S}_{1/2}, \mathrm{F} = 1, \mathrm{m_F} = -1\rangle$ state. The Rabi-frequency for

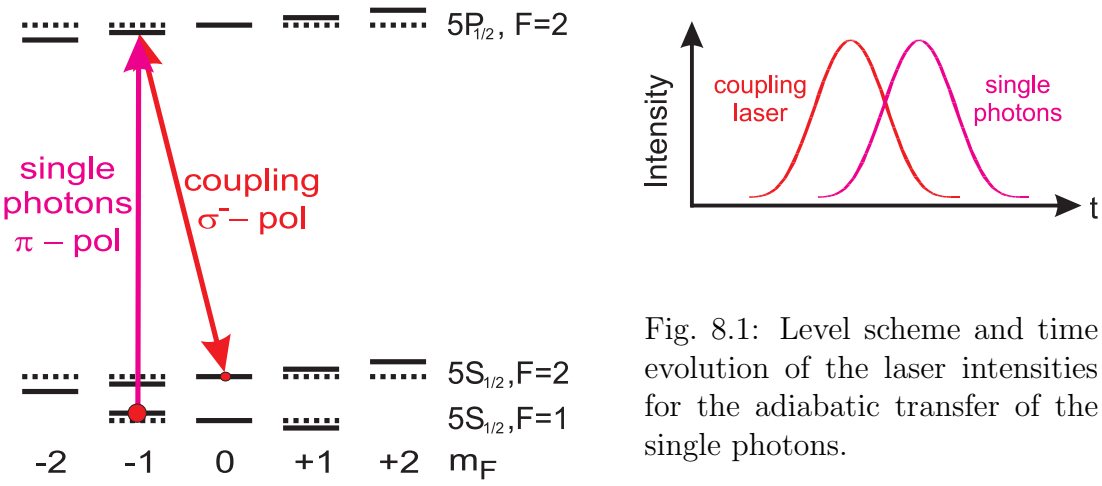

Fig. 8.1: Level scheme and time evolution of the laser intensities for the adiabatic transfer of the single photons.

the adiabatic passage can be obtained from equation 3.21. The time evolution of the probe laser power is approximated via

$$P_p(t) = P_{p0} \sin^8\left(\frac{(t-\tau)}{T_p}\,\pi\right) , \tag{8.3}$$

because then the Rabi-frequency is approximated with a $\sin^4$-function [FSB97] that begins at $t = \tau$ and ends at $t = T_p - \tau$ Relatively to the coupling pulse, the probe pulse is delayed by the time constant τ.
According to equation 3.6, the normalization constant is given by

$$\int_{\tau}^{\tau+T_p} P_p(t)\,dt = \frac{35}{128}\,T_p P_{p0} \stackrel{!}{=} n\,\hbar\omega , \tag{8.4}$$

where we now choose $n = 1$. This means the pulse shall contain exactly one photon.
Hence, we finally get for the Rabi-frequency (equation 3.21)

$$\begin{aligned} \Omega_p(t) &= \Gamma\sqrt{\frac{P_p(t)\,N}{I_{sat}}}\,\frac{1}{(4\,\sigma_y^2 + w_y^2)^{1/4}}\,\frac{1}{(4\,\sigma_z^2 + w_z^2)^{1/4}} \\ &= \sin^4\left(\frac{(t-\tau)}{T_p}\,\pi\right)\Gamma\sqrt{\frac{128}{35}\,\frac{\hbar\omega N}{T_p\,I_{sat}}}\,\frac{1}{(4\,\sigma_y^2 + w_y^2)^{1/4}}\,\frac{1}{(4\,\sigma_z^2 + w_z^2)^{1/4}} . \end{aligned} \tag{8.5}$$

The two pulses shall be equally long and their length, the maximum coupling Rabi-frequency and the time delay τ are varied to obtain the highest efficiency. According to the literature, the Rabi-frequencies should have the same magnitude and the optimal time delay is $\tau = 0.2\,T_p$ [FSB97]. Thus, we will start the

calculations with these assumptions.

We will now estimate the size of the cloud via the maximum trapping potential that allows for magnetic pulling of the atoms.
As shown in section 6.3, the maximal achievable magnetic gradient is 380 G/cm. This gradient can pull atoms in the $|\mathrm{m_F} = -1\rangle$ state with maximum force of $F_{magn} = 1.76 \cdot 10^{-23}$ N (equation 2.28). Given a crossed dipole trap under an angle of $2\,\varphi = 60°$ and a beam waist of $35\,\mu$m, a numerical evaluation of equation B.13 shows that this magnetic gradient can pull atoms out of a trap with a maximum of 570 mW power in each beam.

Under these conditions, the trap depth is $V = 1.03 \cdot 10^{-28}$ J (equation B.12). Due to collisions, the temperature in the trap converges to a temperature T. This temperature is connected to the trap depth by

$$T = \frac{1}{\eta}\frac{V}{k_B}, \tag{8.6}$$

where the ratio η in a dipole trap is typically $\eta = 10$ [LRW96, OGGT01]. This yields a temperature $T = 750$ nK.
Finally, the distribution widths are given by equations 2.18, B.10 and B.11:

$$\begin{aligned} \sigma_y &= 5.35\,\mu\mathrm{m} \\ \sigma_z &= 4.64\,\mu\mathrm{m} \end{aligned} \tag{8.7}$$

The beam waist of the single photon laser is assumed to be $w_y = w_z = 10\,\mu$m (a value that can be achieved easily) and the saturation intensity for the single photon transition (see figure 8.1) is [Ste02]

$$I_{sat} = \frac{4}{3} \cdot 4.484\,\frac{\mathrm{mW}}{\mathrm{cm}^2}\ , \tag{8.8}$$

where the factor 4/3 reflects the ratio of the squared Clebsch-Gordan-coefficients of the transitions $|5\mathrm{S}_{1/2},\ \mathrm{F} = 2,\ \mathrm{m_F} = 2\rangle$–$|5\mathrm{P}_{1/2},\ \mathrm{F} = 2,\ \mathrm{m_F} = 2\rangle$ and $|5\mathrm{S}_{1/2},\ \mathrm{F} = 1,\ \mathrm{m_F} = -1\rangle$–$|5\mathrm{P}_{1/2},\ \mathrm{F} = 2,\ \mathrm{m_F} = -1\rangle$.

To calculate the number of atoms with equation 2.19, we assume an atomic density of $n_0 = 1.2 \cdot 10^{13}\,\mathrm{cm}^{-3}$ [CRGW03], which yields $N = 4.3 \cdot 10^4$.

Hence, we can calculate the single photon Rabi-frequency

$$\Omega_p(t) = \sin^4\left(\frac{(t-\tau)}{T_p}\,\pi\right) \cdot 6.6 \cdot 10^4 \sqrt{\frac{1}{T_p/s}} \cdot \frac{1}{s}\ , \tag{8.9}$$

where the pulse length T_p is the parameter that will be varied in the calculations. The atomic populations were then calculated with equations C.4. The additional state

$$\dot{\rho}_{decay} = +\Gamma \rho_{cc} \tag{8.10}$$

was added to the system. This state collects all population that decays due to spontaneous emission from the excited state.
Figure 8.2 shows an example of a successful single photon transfer.

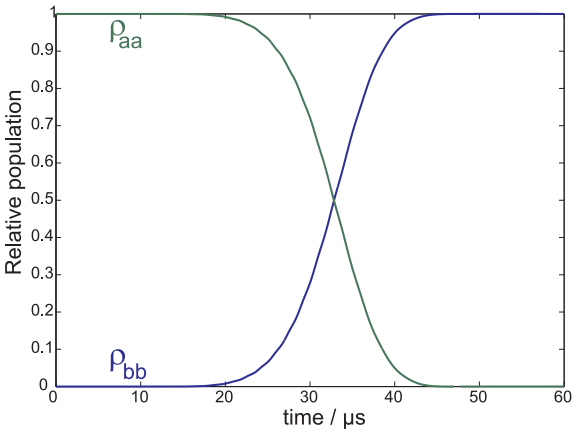

Fig. 8.2: Single photon passage in the adiabatic regime. The probability to transfer the single photon is close to unity. ρ_{aa} equals the population in the collective ground state, ρ_{bb} the population in the collective single excitation state. The Rabi-frequency of the coupling laser is $\Omega_c = 1.6\,\Omega_p$ and the pulse length is $50\,\mu$s.

Using $\Omega_p = 2\pi \cdot 1.5 \cdot 10^6\,\mathrm{Hz}$, the adiabatic criterion (equation 4.44)

$$\sqrt{\Omega_c^2 + \Omega_p^2} \cdot T_p \overset{!}{\gg} 1\ . \tag{8.11}$$

yields 750, which is much larger than 1. This results in a very high transfer efficiency, which is the population in state $|\psi\rangle_\mathrm{e}$ (the collective single excitation state) after the transfer. Here, it is 99.99 %.
The result of the simulations is shown in figure 8.3. Here, the transfer efficiency is plotted in dependence of the coupling laser Rabi-frequency and the pulse length.

In general, the efficiency increases for longer pulses, which comes from the adiabatic criterion. To show this, we approximate $\Omega_c \sim \Omega_p$, extract $\Omega_p \sim 1/\sqrt{T_p}$ from equation 8.9 and get

$$\sqrt{\Omega_c^2 + \Omega_p^2} \cdot T_p \sim \sqrt{2\,T_p}\ . \tag{8.12}$$

This shows that the adiabatic criterion gets more satisfied for longer pulses. On the other hand, shorter pulses are desirable because of collisional loss mechanisms that have not been included in the calculation.

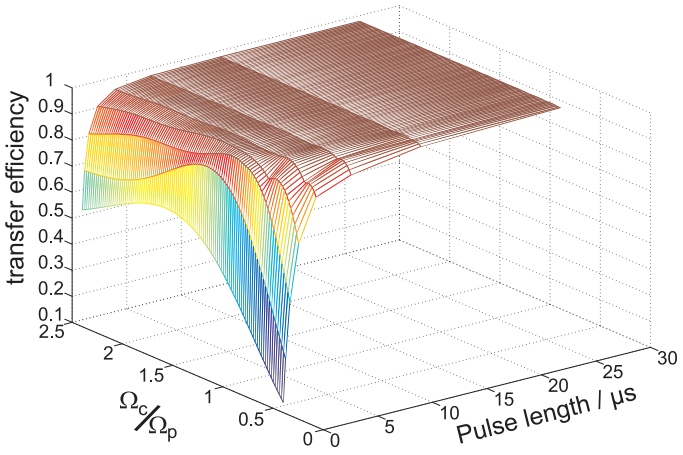

Fig. 8.3: Transfer-efficiency for single photons, depending on the pulse length and the Rabi-frequency of the coupling laser. The latter one is given in units relative to the Rabi-frequency of the single photon Rabi-frequency.

Additionally, the transfer efficiency depends on the Rabi-frequency of the coupling laser. This can also be seen for shorter pulses in figure 8.3. The transfer efficiency shows maxima around $1 \leq \Omega_c/\Omega_p \leq 1.6$. But especially for short pulses and low coupling Rabi-frequencies, it does not show a simple monotonic increasing and afterwards decreasing function. This occurs because in the non-adiabatic regime the transfer gets superimposed with Rabi-oscillations of the population. An example for this is shown in figure 8.4.

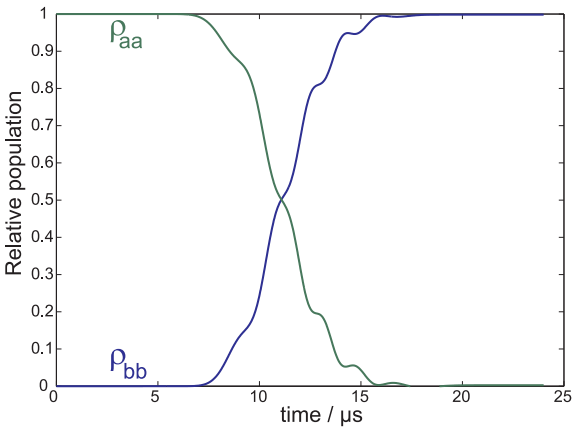

Fig. 8.4: Single photon passage in the non-adiabatic regime. The population transfer is incomplete and the non-adiabaticity can be also seen in the oscillations in the population. The Rabi-frequency of the coupling laser is $\Omega_c = 0.7\,\Omega_p$ and the pulse length is $20\,\mu$s. The transfer occurs earlier than in the adiabatic regime because here the coupling laser Rabi-frequency drops faster below a limit where the velocity of the transfer suddenly increases.

Here, the adiabatic criterion (equation 4.44) yields 390. Due to the large value ($\gg 1$), the transfer efficiency is very high (99.8 %) but on the other hand it is still too low to suppress the superimposed Rabi-oscillations.

The numerical simulations showed an optimum in the time delay between the two pulses of $\tau = 0.2$, which agrees with the values given in the literature [FSB97].

The influence on the adiabatic passage due to the $|5P_{1/2}, F = 1, m_F = -1\rangle$ state can be neglected here. On the one hand, this level is detuned 800 MHz from one-photon-resonance and thus the absorbtion as well as the adiabatic passage via this level are strongly suppressed. Additionally, the ratio between passage and absorbtion is strongly enhanced [JK02], which also results in a successful passage.

As the result of these calculations, we note the probability for an inefficient photon transfer $\eta_{ipt} = 10^{-4}$.

8.2 Polarization dependence

The linear polarization of the single photons should be oriented parallel to the magnetic field. But due to imperfect optical devices, there is always a small admixture of orthogonal, linear polarized light, that splits up into σ^- and σ^+.

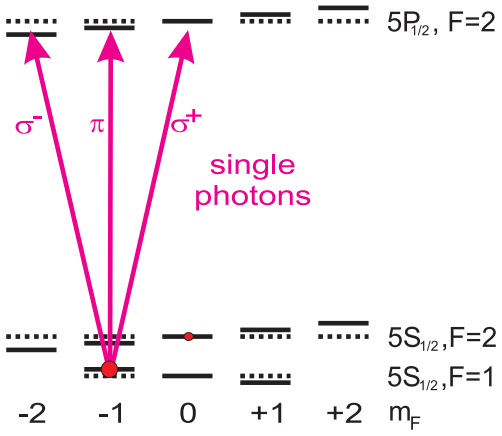

Fig. 8.5: Polarization splitting of the single photons. The wrong polarizations drive different transitions and are detuned from resonance.

Although there is a Zeeman shift of the other levels, there is a non-negligible chance that the photon gets absorbed.
If the polarization of the single photon is σ^-, the atom cannot decay into a magnetically neutral ground state and would be pulled out of the trap when the magnetic gradient is applied. This would imply a loss of the single photon.

If the polarization is σ^+, the absorption probability can be assumed to be unity because of the high optical density and the low detuning of 24 MHz. Then,

due to the Clebsch-Gordan-coefficients, the chance to end up in a magnetic ground state is 2/3, while it is 1/3 to end up in one of the desired magnetically neutral states.
Finally, these factor must be multiplied with the probability of finding the photon in the wrong polarization, which we assume to be 1 ‰, as this is the purity that can be achieved with polarizing beamsplitter cubes [BHN07]

$$\eta_{wp} = \left(\frac{1}{2} + \frac{1}{2}\frac{2}{3}\right) \cdot 1\,‰ = 0.8\,‰ \; . \tag{8.13}$$

8.3 Collisions

Directly after the adiabatic passage, the magnetic gradient will be applied to pull the unwanted atoms out of the dipole trap. During this process, a collision between such an atom and the desired single atom can occur. Due to the low temperature of 750 nK, we have to consider only elastic s-wave collisions.
If we assume to have the atom at the edge of the cloud (which we set to infinity) and must drag all atoms along, the number of these collisions is given by

$$N_{col} = \int_{-\infty}^{\infty} n(\vec{r})\sigma_{sc}\, dy \; , \tag{8.14}$$

where $n(\vec{r})$ denotes the atomic density and σ_{sc} the scattering cross section. For low temperatures (only s-wave collisions), the latter one is given by $\sigma_{sc} = 4\pi a^2$. (As the single atom is in a different magnetic substate, the additional factor of 2 for indistinguishable bosons does not have to be included.) Here, a denotes the scattering length, which is $a = 109\, a_0$ in the case of rubidium-87 and a_0 denotes the Bohr radius.
The atomic density along the y-direction at $x = z = 0$ is given by

$$n(\vec{r}) = n_0 \exp\left(-\frac{y^2}{\sigma_y^2}\right) \; . \tag{8.15}$$

Assuming a density of $1.2{\cdot}10^{13}\,\mathrm{cm}^{-3}$ and a width of $\sigma_y = 5.35\,\mu$m (see section 8.1), we get

$$N_{col} = 0.048 \; . \tag{8.16}$$

As the magnetic gradient is able to pull the atoms out of the trap, the magnetic energy gained by an atom is large enough to kick the single atom by a collision out of the trap. To circumvent this problem, the magnetic gradient can be ramped up slowly. The atoms will then be pulled slowly out of the trap and if a collision

occurs, the transferred kinetic energy will not be large enough to kick the single atom out of the trap. This could only happen if many collisions occur.
As also the spin-changing collisions [BMV96] and the low three-body collision rate [SGOD+99] are strongly suppressed, the collisions with the unwanted atoms can be neglected ($\eta_{col} \approx 0$).

8.4 Single atom detection

As shown in figure 8.6, the single atom is initially in state $|b\rangle$ and has to be pumped into state $|j\rangle$, from there it can scatter light on the closed $|j\rangle$–$|g\rangle$ transition. The excited states for optical pumping are all $|F = 3\rangle$ states and thus the atom cannot decay into an $|F = 1\rangle$ ground state and get lost. But the atom can offresonantly get excited to an $|F = 2\rangle$ state and then decay to an $|F = 1\rangle$ ground state. To avoid this case, an additional repumping laser must be used:

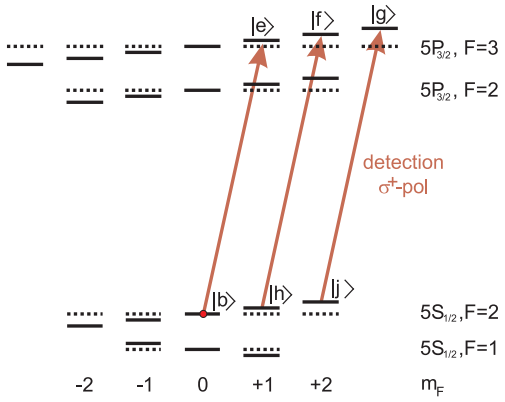

Fig. 8.6: Level scheme of the single atom detection. The atom is initially in state $|b\rangle$ and will be transferred to state $|j\rangle$, from where it can scatter light on the closed $|j\rangle$–$|g\rangle$ transition.

Due to the Clebsch-Gordan-coefficients [Ste02], after scattering 4 photons at low intensity, the probability to be in state $|j\rangle$ is 69 % (where we neglect the strongly suppressed σ^--polarized light admixture in the otherwise σ^+-polarized light). Thus, we will use this rather conservative number to approximate an average number of 2 scattered photons on the $|b\rangle$–$|e\rangle$ transition and 2 on the $|h\rangle$–$|f\rangle$ transition.

For the single atom detection, the magnetic offset field at 100 G will be used. When we tune the detection light to resonance on the $|j\rangle$–$|g\rangle$ transition, the detuning is −49 MHz on the $|b\rangle$–$|e\rangle$ transition and +270 MHz on the $|b\rangle$–$|5P_{1/2}, F = 2\, m_F = 1\rangle$ transition, while it is +2 MHz on the $|h\rangle$–$|f\rangle$ transition and +317 MHz on the $|h\rangle$–$|5P_{1/2}, F = 2\, m_F = 2\rangle$ transition [BR31, Ste02].

The ratio between the respective $|F' = 3\rangle$ and $|F' = 2\rangle$ transition is given by equation 3.39 and yields 3.3 % for the $|b\rangle$–$|e\rangle$ transition and $2 \cdot 10^{-4}$ for the $|h\rangle$–$|f\rangle$ transition. To calculate the total loss probability we note that the probability to decay into an $|F = 1\rangle$ ground state is 50 % for each decay. Thus, we finally get

$$\eta_{ws} = 3.3\,\% \; . \tag{8.17}$$

This rate is too high for high efficiency photon counting and an additional, well polarized repumping laser must be used. It causes

$$\eta_{ws} \approx 0 \; . \tag{8.18}$$

8.5 Lifetime

It is possible that the single atom gets lost due to a background collision during its detection. If we assume a lifetime of $\tau_{lt} = 5\,\mathrm{s}$ and a detection time of $T_{det} = 10\,\mathrm{ms}$, the probability to loose the atom in this time is given by

$$\eta_{lt} = \exp(-T_{det}/\tau_{lt}) = 2 \cdot 10^{-4}; \, . \tag{8.19}$$

Hence, we finally get for the achievable single photon detection efficiency (equation 8.1)

$$\begin{aligned} \eta_{1pd} &= (1 - \eta_{ipt}) \cdot (1 - \eta_{wp}) \cdot (1 - \eta_{col}) \cdot (1 - \eta_{ws}) \cdot (1 - \eta_{lt}) \\ &= 99.9\,\% \; . \end{aligned} \tag{8.20}$$

8.6 Optical pumping

Before the adiabatic passage is performed, all atoms must be pumped into the $|5S_{1/2}, F = 1, m_F = -1\rangle$ state. Because there exists no excited state which provides a closed transition to this ground state, it is not possible to pump into this state with high efficiency. Thus, the atoms will be collected in the $|5S_{1/2}, F = 2, m_F = -2\rangle$ state and then transferred to the $|5S_{1/2}, F = 1, m_F = -1\rangle$ state with a microwave Landau-Zener sweep [RKLK81]. This sweep will exchange the populations of the two states with high efficiency. The remaining population can be neglected because only the population in the two $|m_F = 0\rangle$ states disturbs the single photon detection. This pumping scheme is shown in figure 8.7.

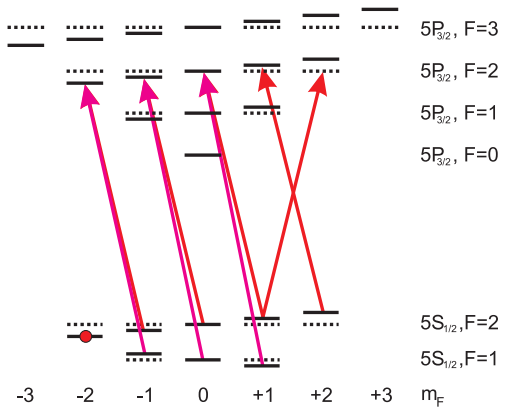

Fig. 8.7: Level scheme for the optical pumping. The pumping is mainly done via the $F' = 2$ states. But due to the required very high population purity, all levels have to be taken into account. Furthermore, as an example, the σ^+-admixture is shown for one transition.

To simulate the optical pumping, a rate equation system for the eight magnetic ground states had to be solved. Here, the change in the population of a state is proportional to the scattering rate of the light that pumps its population away. Additionally, this pumped population ends up in another state (defined by the Clebsch-Gordan-coefficients) and one has to find the steady state solution.

For simplicity it was assumed that the light is applied with one frequency and the resulting detuning on each transition was considered. This is a conservative estimate because the frequency of the monochromatic light can be changed within the pumping sequence and thus the efficiency can be further increased.
For the calculation we have assumed a σ^+-polarized intensity admixture of 1 ‰ [BHN07] to the otherwise σ^--polarized light.

The assumed intensity on the MOT transition is $0.22 \cdot I_{sat}$ and the one on the repumping transition $4 \cdot I_{sat}$.
Normalized to a total population of 43000 atoms (see section 8.1), the rate equations revealed a population of 10^{-3} atoms in the $|5S_{1/2}, F = 1, m_F = 0\rangle$ state and a population of $5 \cdot 10^{-3}$ atoms in the $|5S_{1/2}, F = 2, m_F = 0\rangle$ state.

Thus, we get a probability to detect a photon although none arrived of

$$\eta_{m_F 0} = 6 \cdot 10^{-3} \, . \tag{8.21}$$

Most of the remaining population is caught in the $|5S_{1/2}, F = 2, m_F = -2\rangle$ state. The only other significant population of 25 atoms ends in the $|5S_{1/2}, F = 2, m_F = -1\rangle$ state. But this can be neglected, as the atoms will also be pulled out of the trap with the magnetic gradient.

The pumping time was 10 ms, which is necessary to reach the steady state solution. As this is a rather long time for optical pumping, the pumping sequence can already be applied during the evaporative cooling in the dipole trap.

The detuning on the MOT transition was −314 MHz, relative to the unshifted $|F = 2\rangle$–$|F' = 3\rangle$ transition, while the detuning on the repumping transition was −179 MHz, relative to the unshifted $|F = 1\rangle$–$|F' = 1\rangle$ transition. It should be noted that the population in the magnetically neutral states can be further lowered, when the detuning is not held constant but modified in a ramping sequence. The simulation showed that the population in the magnetically neutral states can be further lowered when microwave radiation is applied between the two $|m_F = 0\rangle$ ground states during the optical pumping process.

8.7 Offresonant scattering

The σ^--polarized coupling laser interacts not only on the $|5S_{1/2}, F = 2, m_F = 0\rangle$–$|5P_{1/2}, F = 2, m_F = -1\rangle$ transition. It also couples the $|5S_{1/2}, F = 1, m_F = -1\rangle$ ground state, in which the atoms are collected, with the excited state $|5P_{1/2}, F = 2, m_F = -2\rangle$. Due to the large detuning of 6.8 GHz, the influence on the adiabatic passage can be neglected. The atoms, which are excited, decay back to a ground state with $m_F < 0$ and are thus magnetically pulled out of the trap afterwards.

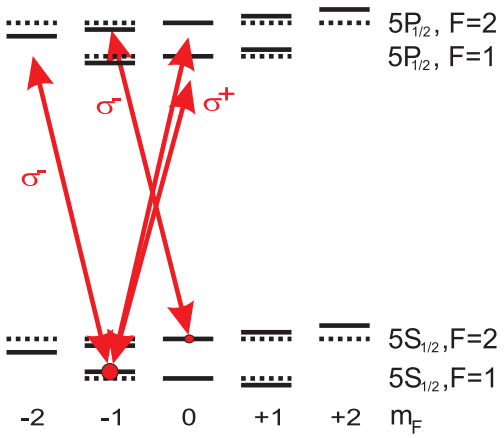

Fig. 8.8: The excited states, which are coupled to the populated ground state by the σ^+-polarized part of the coupling laser. Furthermore, the intended transition with the σ^--polarized part is shown. The detunings are indicated by arrows that don't hit the respective levels.

But the coupling laser also has a small admixture of σ^+-polarized light. This couples the $|5S_{1/2}, F = 1, m_F = -1\rangle$ ground state, in which the atoms are collected, with the excited states $|5P_{1/2}, F = 1, m_F = 0\rangle$ and $|5P_{1/2}, F = 2, m_F = 0\rangle$. These states can decay into the magnetically neutral ground states $|5P_{1/2}, F = 2, m_F = 0\rangle$ and $|5P_{1/2}, F = 1, m_F = 0\rangle$. Integrating in time over the scattering rate (equation 3.39) and using the Rabi-frequency, atom number and pulse length given in section 8.1, the Clebsch-Gordan-coefficients for the respective transitions [Ste02] and assuming a σ^+ intensity admixture of

1 ‰ [BHN07], we find that the coupling pulse transfers $2.9 \cdot 10^{-4}$ atoms (normalized to 43000 atoms) into each of the two magnetically neutral ground states. This yields an efficiency of

$$\eta_{cls} = 5.8 \cdot 10^{-4}. \tag{8.22}$$

Hence, we finally get for the efficiency of not detecting an absent photon

$$\eta_{0pd} = 99.3\,\% \; . \tag{8.23}$$

As the coupling laser also couples the $|5S_{1/2}, F = 2, m_F = -2\rangle$–$|5P_{1/2}, F = 2, m_F = -1\rangle$ transition, one has to ensure that this ground state gets fully emptied by the microwave sweep.

9. Electromagnetically Induced Transparency

As we have measured EIT in optically trapped rubidium atoms, I will discuss in this chapter, how narrow the EIT bandwidth can get in such a system.

The bandwidth (transparency width) is responsible for the velocity of slowed light as well as for the maximum possible storage time of stopped light and thus it is the most interesting EIT quantity.
As has been shown in section 4.3, the transmission spectrum depends on the density and length of the cloud, the polariton loss due to collisions, the length of the probe pulse, the Rabi-frequency of the coupling laser and the probe laser detuning.

For the cloud, we will take the values necessary for the single photon detection (see chapter 8): the length of the cloud is given by twice its width, $l = 2\,\sigma_y = 10.7\,\mu$m and the atomic density is $n_0 = 1.2 \cdot 10^{13}\,\mathrm{cm}^{-3}$.

In a chamber with ultra high vacuum, the lifetime of a cold cloud can be several seconds [CRGW03]. Therefore, we will assume a conservative collisional decay rate of $\gamma = 1\,$Hz. This rate limits the pulse length: if longer pulses are used, the polaritons would decay before they could be read out. Therefore, I will choose the total pulse length (equation 8.3) to match the collisional decay rate, that is $T_p = 1\,$s, which equals $\tau = 0.25\,$s in equation 4.35. Then it is unlikely to get unity transparency, but still enough signal to keep the photon number low.

To estimate the required coupling laser Rabi-frequency, we assume to detect 20 % of the initial photons of the probe beam (due to insufficient transparency and detection efficiency). If we want to detect at least 30 photons, we need the statistics of many experiments to measure an EIT spectrum, but this can be done experimentally.
The assumption of 150 probe photons leads to maximum probe laser Rabi-frequency of $\Omega_p = 64.9\,$kHz (equation 8.5). Thus, we estimate the required coupling laser Rabi-frequency via $\Omega_c = 1.6 \cdot \Omega_p = 104\,$kHz (see section 8.1).

To get a first result, we assume the coupling laser to be resonant ($\Delta_c = 0$) and get from equation 4.25 the width of the EIT resonance

$$\sigma_p = 24.3\,\mathrm{Hz}\ , \tag{9.1}$$

where the transparency on resonance is $T = 0.88$.

Using these values in equations 4.36 and 4.37 leads to

$$\begin{aligned} T_{r,\,pulse}(\Delta_p) &= 0.88\,\pi\,\tau \int_{-\infty}^{+\infty} e^{-\Delta'^2/\sigma_p^2}\, e^{-\pi^2\tau^2(\Delta_p-\Delta')^2}\, d\Delta' \\ &= 0.879\, e^{-\Delta_p^2/(24.3\,\mathrm{Hz})^2}\ . \end{aligned} \tag{9.2}$$

This shows that the pulse length is not a limiting factor in this regime.

The probe laser detuning can be zero if we simply tune the laser to resonance. But the two involved atomic ground states experience different quadratic Stark shifts (see section 2.4), depending on their position in the trap. If an atom is at the edge of the trap, the quadratic stark shift of both levels is zero. At the trap center, their shift is given by equations B.12, 2.20 and 2.21.
For a narrow bandwidth EIT measurement, we choose the states $|5S_{1/2},\ F = 2,\ m_F = -1\rangle$ and $|5S_{1/2},\ F = 1,\ m_F = 1\rangle$ as they shift equally in the same direction in the linear Zeeman effect, which decreases magnetic broadening due to inhomogeneities in the magnetic offset field.

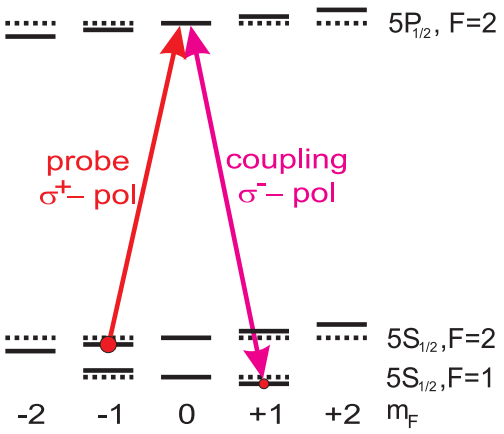

Fig. 9.1: Level scheme for a narrow bandwidth EIT-measurement.

At an offset field of 100 G, the different quadratic Stark shift of these states is $\Delta_{qss} = 27.4\,\mathrm{Hz}$.

Then, as a conservative estimate we assume to have the atoms equally distributed over all possible values $0 \leq \Delta_{qss} \leq 27.4\,\mathrm{Hz}$. Therefore we can average over all possible transfer functions, which yields the final result

$$\sigma_{min} = 25.5\,\mathrm{Hz}\ . \tag{9.3}$$

It should be noted that the assumed values, especially the low photon number at the relatively long pulse length, are experimentally demanding. Also, the two lasers must be very stable, which means the relative drift to each other must be much less than 25.5 Hz.

In a magnetic trap, the quadratic Zeeman shift is analogous to the quadratic Stark shift of the dipole trap. For a typical magnetic trap [Pri83, MAvD$^+$96], the maximal difference in the shift is $\Delta_{qzs} \approx 20\,\mathrm{Hz}$. Thus, the minimum achievable linewidth is comparable to the one in a dipole trap. But in a magnetic trap the field is not homogeneous and thus it is not possible to clearly address the different magnetic substates of the medium.

In special vapor cells, containing an additional buffer gas that reduces spin-changing collisions between the atom, the narrowest EIT lines at widths of $\sim 30\,\mathrm{Hz}$ have been measured [BNWM97, ENH00]. Here, one is not limited by pulse lengths and very low Rabi-frequencies can be used.

Part IV

Experimental Results

10. Magneto-optical trap and Dark MOT

For loading the magneto-optical trap (MOT), a rubidium dispenser with an electric current of 5.6 A was used. The optical power in each of the MOT beams was 20 mW on the MOT transition and 1 mW on the repumping transition. Furthermore, a magnetic gradient of $\sim 11.9\,\mathrm{G/cm}$ (depending on the following sequence) was applied during the 2 seconds long MOT phase.

The measurements were performed with the time-of-flight method (TOF). Here, a picture of the free-falling cloud is taken after several time steps, where a new cloud has to be prepared for each measurement. As the momentum distribution of the atoms is transformed into a spatial distribution during the expansion, one can estimate the temperature of the cloud by its expansion rate. The pictures were taken with the fluorescence method, where the camera collects light that is emitted by the cloud when it is illuminated with resonant light. Here, two pictures have to be taken: one with the atoms and one without the atoms. The latter one is used to determine the ambient background and is subtracted from the first one. The calibration of the imaging system is used to determine the size of the cloud while the amount of collected light reveals the number of atoms. Combining these quantities finally yields the density in the cloud.
Up to $\sim 1.7 \cdot 10^9$ atoms at temperatures of $\sim 400\,\mu\mathrm{K}$ could be captured in the MOT.

Since the atoms in the MOT are too hot to be transferred into the dipole trap, a dark MOT phase [CRGW03] has to be applied on the atoms.
During this dark MOT phase (DM), which is applied for 17 ms, the frequency of the cooling light for operating the MOT was detuned $-100\,\mathrm{MHz}$ from resonance. Furthermore, the repumping power was reduced to 1 % of its value. Because of this, the atoms scatter less photons and thus their temperature decreases significantly. As one also looses confinement in real space, a portion of the atoms is lost. To reduce this loss, the magnetic gradient is ramped up to its maximum value of $16.9\,\mathrm{G/cm}$.

The atom number was then reduced to $9.3 \cdot 10^8$ and the density was $n_0 = 1.4 \cdot 10^{12}\,\mathrm{cm}^{-3}$. This high density could only be achieved because the dipole trap had been turned on already. The temperature of the ensemble was again determined with the time-of-flight method. Figure 10.1 shows the time evolution of the cloud radius in two dimensions.

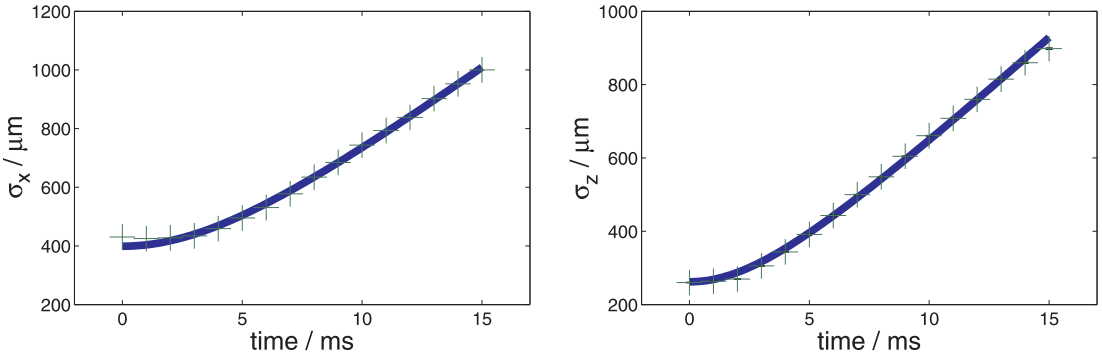

Fig. 10.1: Expansion of the free-falling dark MOT cloud in x- and z-direction. The green crosses indicate the measured data points, while the blue line is fitted into them.

Here, the ensemble is in thermal equilibrium and the obtained temperatures are $T_x = 40\,\mu\mathrm{K}$ and $T_z = 37\,\mu\mathrm{K}$. The measured size of the captured cloud was $\sigma_x = 400\,\mu\mathrm{m}$ and $\sigma_z = 260\,\mu\mathrm{m}$.
Figure 10.2 shows a fluorescence picture of the dark MOT.

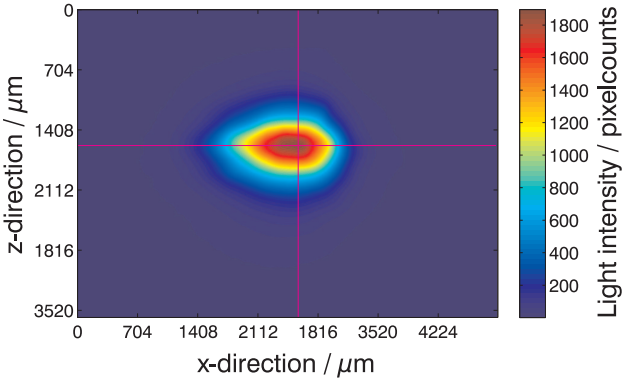

Fig. 10.2: A fluorescence picture of the cloud after the dark MOT sequence. It contains $9.3 \cdot 10^8$ atoms. Areas with a higher atomic density scatter more light and are indicated red in the miscolored picture.

11. Dipole Trap

The dipole trap (DT) was already turned on during the MOT and DM phases. After the DM phase, the MOT lasers were turned off and up to $3.4 \cdot 10^7$ atoms could be captured in the DT. The atom number was also determined by taking fluorescence pictures.

As the frequency range of the Raman laser system is limited, the Stark shift of the dipole trap must be used to shift the atomic levels into resonance with the Raman lasers. For performing the EIT measurements at an offset field of 100 G, the optical power in each CO_2-laser beam had to be reduced from the maximum of 42 W to 13.1 W (see chapters 12 and 13). Thus, I will present the cloud parameters for this optical power.

Figure 11.1 shows the time evolution of the cloud radius in two dimensions. The data was taken 30 ms after the DM was turned off. Then, the plain evaporation (see section 11.1) had not yet stopped, but that didn't affect the EIT measurements.

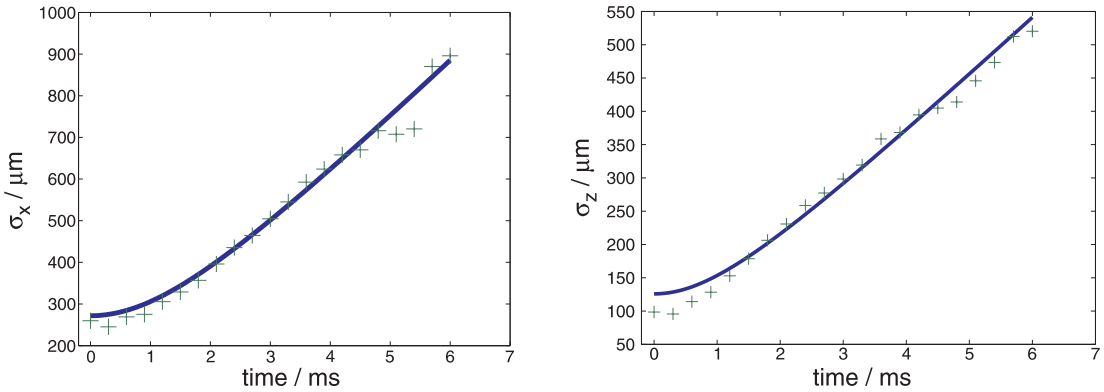

Fig. 11.1: Expansion of the free-falling dipole trap cloud in x- and z-direction.

The temperature obtained from the expansion at large radii yields $T_x = 200\,\mu$K and $T_z = 80\,\mu$K. This shows clearly that the cloud is not in thermal equilibrium.

The collision rate is given by

$$\Gamma_{col} = n_0 \, \sigma_{sc} \, v \ , \tag{11.1}$$

where v denotes the average velocity of the atoms and $\sigma_{sc} = 8\pi a^2$ denotes the scattering cross section. The latter one includes a factor of 2, corresponding to the indistinguishability of bosons. Here, a denotes the scattering length, which is $a = 109\, a_0$ in the case of rubidium-87 and a_0 denotes the Bohr radius.
Using an average temperature

$$T_{av} = \left\{ T_x \, T_z^2 \right\}^{1/3} = 109\, \mu K \ , \tag{11.2}$$

we get an average velocity of

$$v = \sqrt{\frac{3 k_B T_{av}}{m}} = 0.18\, \mathrm{m/s}. \tag{11.3}$$

Together with the measured density of $n_0 = 2.3 \cdot 10^{11}\, \mathrm{cm}^{-3}$, this yields a collision rate of

$$\Gamma_{col} = 32\, 1/\mathrm{s} \ . \tag{11.4}$$

As about 3 collisions per atom are necessary to bring the cloud into thermal equilibrium, the thermalization time is about $\tau_{therm} \approx 100\, \mathrm{ms}$. Due to the lifetime of 770 ms, this collision rate is too low for effective evaporation. Thus, the transfer from the DM to the DT has to be modified. By changing the parameters of the DM phase, the density in the DT can be enhanced by accepting a lower number of atoms.
The achieved optical densities (see chapters 12 and 13) were sufficient for measuring narrow bandwidth EIT, but they will not be sufficient for the single photon detection (see chapter 8). Thus, a higher number density has to be achieved before the cooling sequence can be started.
The measured radii of the cloud were $\sigma_x = 272\, \mu\mathrm{m}$ and $\sigma_z = 126\, \mu\mathrm{m}$. A fluorescence picture of the dipole trap is shown in figure 11.2.

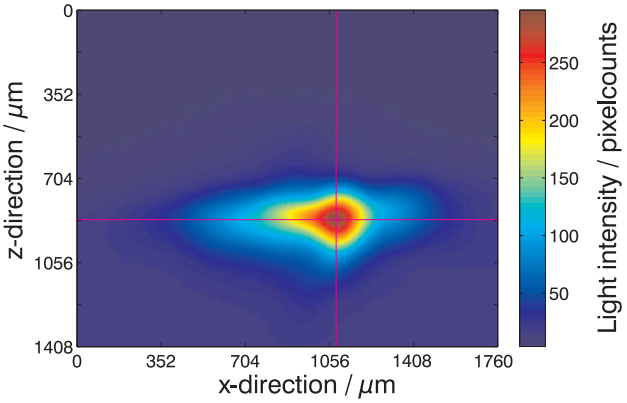

Fig. 11.2: A fluorescence picture of the dipole trap sample. It contains $3.4 \cdot 10^7$ atoms. Contrary to the picture of the dark MOT sample, a part of the total picture is enlarged here.

11.1 Lifetime

The lifetime in the dipole trap has been measured for the two possible single beam traps as well as for the crossed beam dipole trap. Here, the maximum optical power of 42 W in each beam could be used. The time evolution of the atom number is shown in figure 11.3.

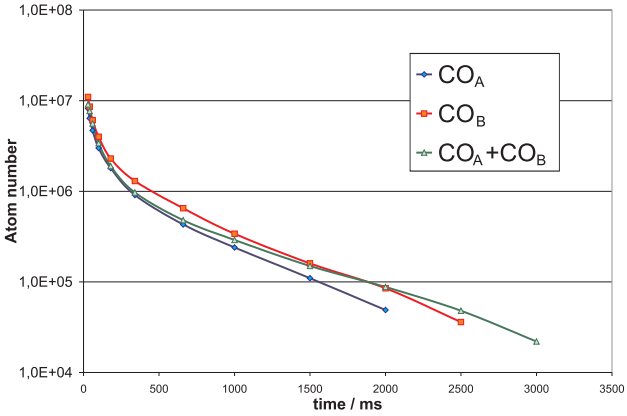

Fig. 11.3: Semilogarithmic plot of the atom number in the dipole trap. The plain evaporation takes place within the first 600 ms. After that, an exponential fit to the data yields the lifetime of the ensemble and the pressure in the chamber.

Due to the logarithmic scale it can be seen that initially the atom number decreases very fast until it reaches an exponential decay. The initial decay is attributed to plain evaporation. It results from the fact that the dipole trap is initially filled up to the edge. Then, the hottest atoms can gain enough energy to leave the trap in a collision until a ratio between the trap depth and the temperature of $\eta \approx 10$ (see section 8.1) is reached. As the trap depth is $V = 4.4\,\mathrm{mK}$ (see section 12.1) and the average temperature (equation 11.2) after 660 ms is $T_{av} = 350\,\mu\mathrm{K}$, this ratio is experimentally confirmed.
30 ms after loading the dipole trap, the atomic density is $n_0 = 1.6 \cdot 10^{11}\,\mathrm{cm}^{-3}$ and the average temperature $T_{av} = 570\,\mu\mathrm{K}$. Using equations 11.1 and 11.3, we get a collision rate of

$$\Gamma_{col} = 54\,1/\mathrm{s}\,, \tag{11.5}$$

which is large enough to perform the plain evaporation within 660 ms.

The subsequently following decay is exponential and yields the lifetime τ in the trap via

$$N(t) = N_0\, e^{-t/\tau}\,. \tag{11.6}$$

This exponential curve was fitted to the data points past 660 ms (to ensure that the plain evaporation had finished). The lifetimes in the single beam trap were $\tau_A = 670\,\mathrm{ms}$ and $\tau_B = 630\,\mathrm{ms}$, while the lifetime in the crossed beam trap was

$\tau_{CB} = 770\,\text{ms}$. This corresponds to the fact that the crossed beam trap is deeper than the single beam traps and an atom has to gain more energy to leave the trap.

As the exponential decay corresponds to collisions with the background gas, the pressure in the chamber is given by (see section 2.6)

$$p \approx 1.3 \cdot 10^{-8} \frac{1}{\tau_D/[s]}\,\text{mbar}\,. \tag{11.7}$$

Using the lifetime in the crossed beam dipole trap, this yields a pressure of

$$p \approx 1.7 \cdot 10^{-8}\,\text{mbar}\,. \tag{11.8}$$

This pressure is two magnitudes higher than the pressure obtained from the Ion gauge and the leak test (see section 5.6). Since the dispensers evaporate the rubidium into the main chamber, the pressure there is higher than at the pumping cross. Also, some of the evaporated rubidium atoms hit the cloud directly, that means without having any collisions with other atoms or the chamber. The collisions between these atoms and the captured atoms lead to lower lifetimes, which results in an supposed higher pressure.
The same effect occurs due to heating mechanisms in the dipole trap. When atoms in the dipole trap heat up, e.g. due to fluctuations in the light intensity (parametric heating), some of the hot atoms leave the trap, which also results in an supposed higher pressure.
To reduce the collisions with atoms from the rubidium dispensers, many experiments use lower currents through the dispensers or use the dispensers in a pulsed mode [FGHZ98, GP03]. Initially, this results in longer MOT loading times (up to 30 s) and nevertheless lower atom numbers. But the reduced background collision rate finally leads to higher atom numbers after forced evaporation.
In this experiment, high cw currents were used because this yields an initially higher optical density while the disadvantage of the higher pressure did not influence the experiment since forced evaporation couldn't be performed due to low number densities in the dipole trap.

12. Absorption Measurements

For the absorption measurements, the laser passes through the atomic cloud to the camera, which is placed behind the cloud. Three pictures have to be taken: one with the atoms (A), one without the atoms and the laser turned on (B) and a last one with the laser turned off (C). The last one is used to determine the ambient background and is respectively subtracted from the other two. These pictures are then divided through each other: $(A-C)/(B-C)$. This yields the transmission through the cloud via

$$T = 1 - \frac{A-C}{B-C} \tag{12.1}$$

and therefore the optical density

$$OD = -\log_{10} T \, . \tag{12.2}$$

This signal can be combined with the calibration of the CCD camera to obtain the atom number of the cloud [KDSK99]. For the measurements, the probe laser of the Raman laser system was used.
Lenses were adjusted to image the cloud onto the CCD camera (see figure 7.4). As described by Marte [Mar03], it is possible to adjust the imaging lenses by taking absorbtion pictures at several lens positions: depending on the lens position and the laser detuning, a focused or expanded image of the cloud will be recorded.

For measuring the absorption spectra, the atoms were captured in the crossed beam dipole trap with 13.1 W in each beam. In this trap, the atoms experience a position-dependent potential and thus a position-dependent Stark shift on their levels.
To get rid of this shift, the dipole trap must be turned off before the absorption picture is taken. Figure 12.1 shows such an absorption spectrum of the optically trapped ensemble.

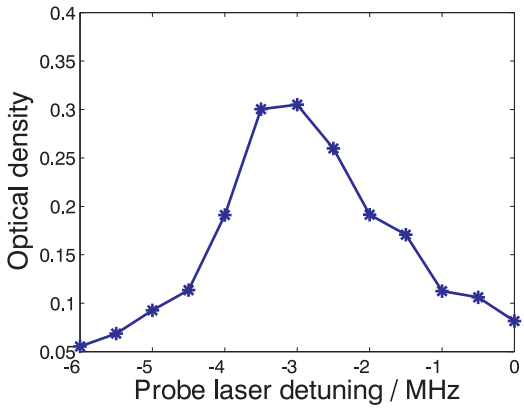

Fig. 12.1: An absorption spectrum of the optically trapped cloud. It has been taken 30 ms after the DM was turned off. Then, the plain evaporation had just finished. The probe laser is applied for 200 μs.

12.1 Stark shift

As the atoms in the dipole trap experience a position-depended Stark shift, it is possible to measure this shift by taking absorption spectra while the dipole trap is turned on.

The energy distribution in the dipole trap is given by the Boltzmann function. In terms of the frequency shift it reads

$$N(\nu) = p\frac{E_\nu}{{E_T}^{3/2}}e^{-\frac{E_\nu}{E_T}} \ . \tag{12.3}$$

Here, $E_\nu = h(\Delta\nu - \nu_0)$ denotes the energy of an atom and $E_T = k_B T$ the temperature of the cloud. p, ν_0, $\Delta\nu$ and T are the parameters, that were fitted to the data. Hereby, ν_0 denotes the Stark shift of the trap. Figure 12.2 shows the excited state, that is subject to this distribution.

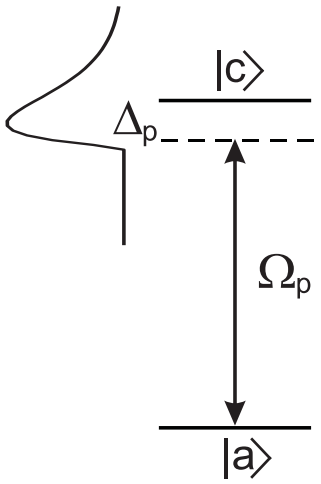

Fig. 12.2: The Stark shift effects the ground as well as the excited state. The frequency distribution is shown along the excited state, where the ground state has been set as reference. Ω_p denotes the Rabi-frequency of the probe laser and Δ_p its detuning from resonance.

Figure 12.3 shows an example of a measurement in the single beam dipole trap for three different powers in the CO_2-laser.

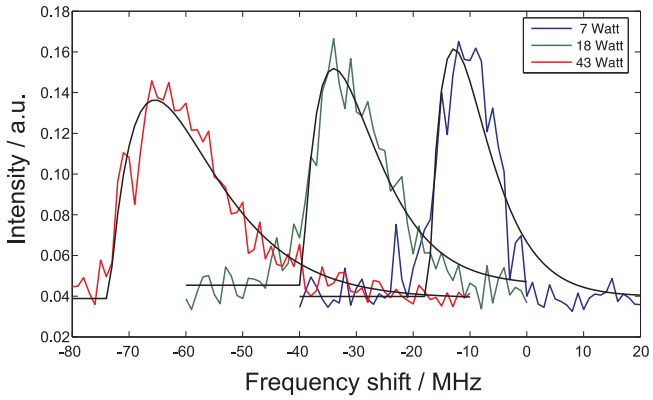

Fig. 12.3: Three absorption spectra in the single beam optical dipole trap. The colored curves show the measured data and the black lines the fitted theory curves. The blue curve corresponds to a laser power of 7 W, the green curve to a laser power of 16 W and the red one to a laser power of 43 W.

It can be seen that the Stark shift on the atomic levels increases for higher laser powers.

Since the EIT measurements were taken in the crossed dipole trap, the Stark shift was quantitatively measured therein. Figure 12.4 shows this measurement for several different powers in the CO_2-laser.

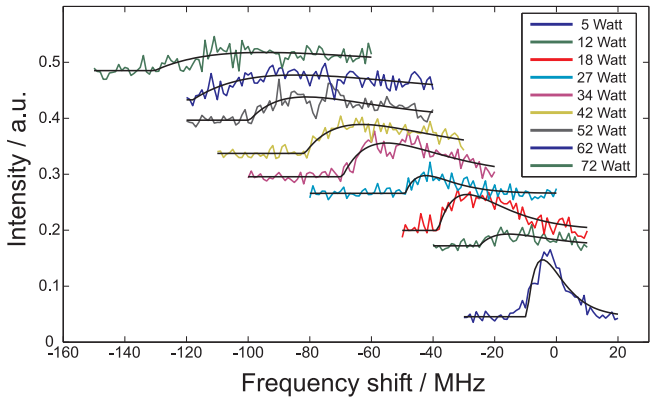

Fig. 12.4: Measurement of the Stark shift in the crossed beam optical dipole trap. For a better survey, the different measurements have been shifted along the y-axis. Since the optical density is subject to fluctuations, the peaks have a different relative intensity.

The parameter ν_0 determines the maximum frequency shift in the dipole trap and reflects the dipole potential, given by equation B.12

$$|V(x=0,\, y=0,\, z=0)| = \frac{2\alpha P}{\pi c\, \varepsilon_0 w_0^2}\,. \tag{12.4}$$

Using $V(0,0,0) = h\nu$ and taking into account that the polarizabilities of the ground state $\alpha_{5S_{1/2}}$ and the excited state $\alpha_{5P_{1/2}}$ are responsible for the transition frequency leads to

$$\nu_0 = \frac{2(\alpha_{5P_{1/2}} - \alpha_{5S_{1/2}})}{h\pi c\,\varepsilon_0 w_0^2}\,P\,. \tag{12.5}$$

Plotting this shift versus the total laser power $2P$, this yields a straight line $\nu_0 = m2P + b$ with a slope

$$m = \frac{2(\alpha_{5P1/2} - \alpha_{5S1/2})}{h\pi c\,\varepsilon_0 w_0^2}\,. \tag{12.6}$$

With our laser locking technique (see section 7.1 and reference [PFL+03]), the absolute value of the probe laser frequency is only known within several MHz. This can result in a possible offset b. Furthermore, the offset corresponds to the natural line width of rubidium and the additional Doppler shift, which are about $-4.3\,\mathrm{MHz}$ (see chapter 12). In figure 12.5, the shift and the fitted line are plotted versus the total laser power.

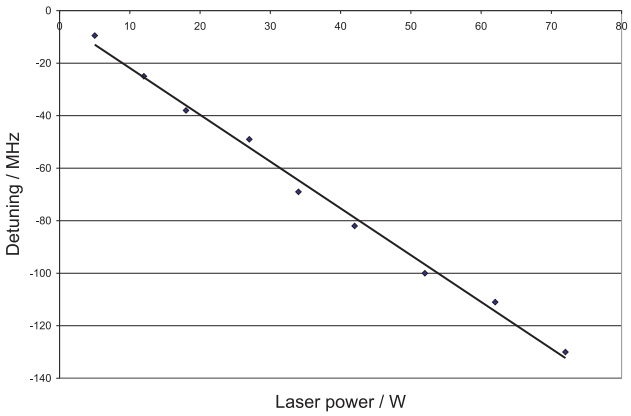

Fig. 12.5: Maximum ac Stark shift on the atomic levels in the crossed beam dipole trap versus the total CO_2-laser power.

Using $\alpha_{5P_{1/2}} - \alpha_{5S_{1/2}} = h \cdot 0.122306\,\mathrm{Hz/(V/cm)^2}$ [Ste02], the fit of the line finally yields $m = 1.78 \pm 0.08\,\mathrm{MHz/W}$ and a realistic offset of $-4\,\mathrm{MHz}$. Together with equation 12.6, this yields the waist of the dipole laser beams

$$w_0 = 28.7 \pm 0.7\,\mu\mathrm{m}\,. \tag{12.7}$$

As a waist of $35\,\mu$m was initially assumed (calculated via the beam diameter, the focussing length of the lens and Gaussian optics), this is a very encouraging result.

At a laser power of $42\,\mathrm{W}$ in each beam, this yields a trap depth of (equation 12.4)

$$|V(x=0,\,y=0,\,z=0)| = 4.4\mathrm{mK}\,. \tag{12.8}$$

12.2 Magnetic offset field

A magnetic offset field can be used to address magnetic substates individually. It can be seen in figure 12.4 that the absorption spectrum in the dipole trap is $\sim$ 40 MHz wide. Therefore, the transitions should be separated by at least 50 MHz. The σ^+-polarized probe laser couples the $|\mathrm{F} = 2\rangle$ ground state to the excited $|5\mathrm{P}_{1/2}, \mathrm{F} = 2\rangle$ state. Figure 12.6 shows an absorption spectrum with an offset field of 118.7 G.

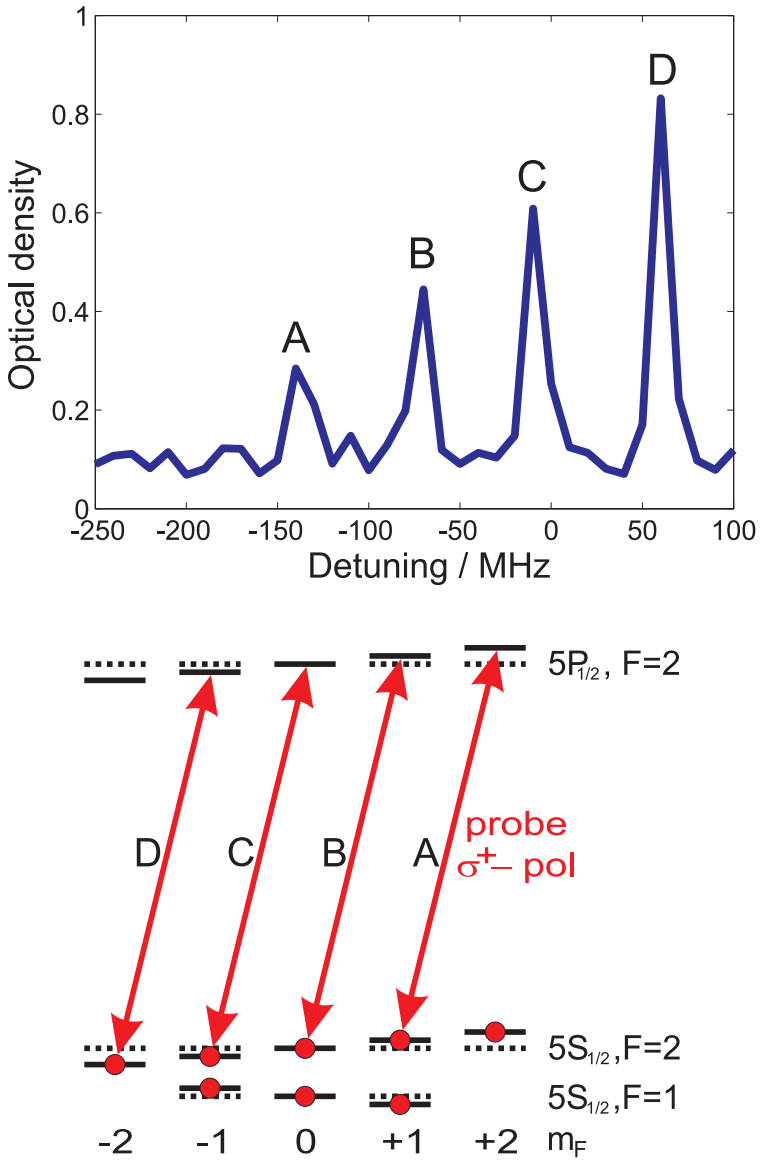

Fig. 12.6: Absorption spectrum of optically trapped atoms at an offset field of 118.7 G. Four addressed substates can be seen. The indicated absorption peaks correspond to the likewise indicated transitions in the figure below. The transition peaks increase from A to D as the atoms are unequally pumped in the respective ground states during prior optical pumping. The offset in the optical density of $\sim$ 0.1 corresponds to noise.

As peak C has been used for the EIT measurements, figure 12.7 shows a scan of

this peak at higher resolution.

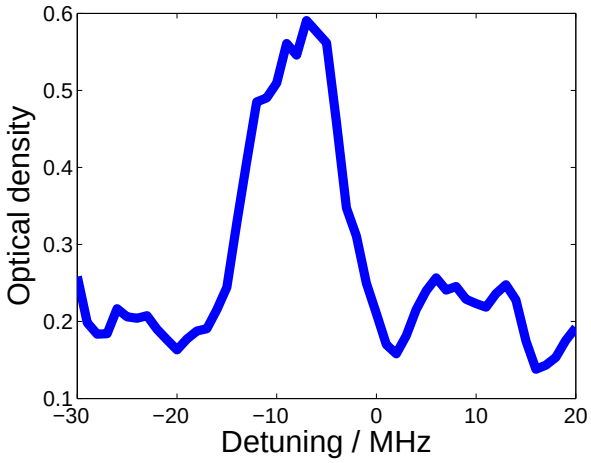

Fig. 12.7: Scan of the $|5S_{1/2}, F = 2, m_F = -1\rangle$–$|5P_{1/2}, F = 2, m_F = 0\rangle$ transition at an offset field of 118.7 G. The peak is centered around $\Delta_p \approx -7$ MHz, which corresponds to the differential quadratic Zeeman shift between the ground states $|5S_{1/2}, F = 2, m_F = -1\rangle$ and $|5S_{1/2}, F = 1, m_F = +1\rangle$. Due to the frequency lock of the Raman laser system, the probe laser detuning refers to the latter state. Here, the background noise in the optical density is ~ 0.2.

13. Electromagnetically Induced Transparency

After measuring the absorption spectrum, the peak on the $|5S_{1/2}, F = 2, m_F = -1\rangle$–$|5P_{1/2}, F = 2, m_F = 0\rangle$ transition was used to measure electromagnetically induced transparency in an optically trapped cloud.

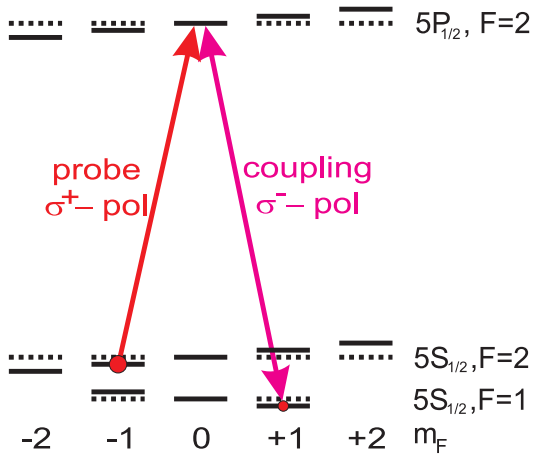

Fig. 13.1: Level scheme for the EIT-measurement. The coupling laser induces transparency on the $|5S_{1/2}, F = 2, m_F = -1\rangle$–$|5P_{1/2}, F = 2, m_F = 0\rangle$ transition. The ground states have been chosen because of their equal linear Zeeman shift.

At the high magnetic offset field of 118.7 G, the two involved ground states shift unequal because of the quadratic Zeeman shift. At this field, the differential shift is ~ -7 MHz.
Between the absorption measurements and the EIT measurements the locking point of the probe and the coupling laser had slightly shifted. With the new lock, the magnetic field had to be increased to 129.7 G ($\widehat{=}129\,A$ current) because then the maximum of the absorption peak was around -7 MHz.

So far, the results of the absorption measurement have been presented as optical density OD, but from now on the transmission T itself will be used, as in the theoretical part. They can be transformed into each other via $T = 10^{-OD}$.

We have measured the EIT-resonance spectrum for three different lengths of the probe pulse: $\tau = 5\mu$s, $\tau = 20\mu$s and $\tau = 100\mu$s. Figure 13.2 shows the data of one measurement with a pulse length of 20 μs and a coupling laser Rabi-frequency of 1.2 MHz. In this measurement, it can be seen, that the signal contains an absorptive (the peak itself) as well as a dispersive part (the asymmetry).

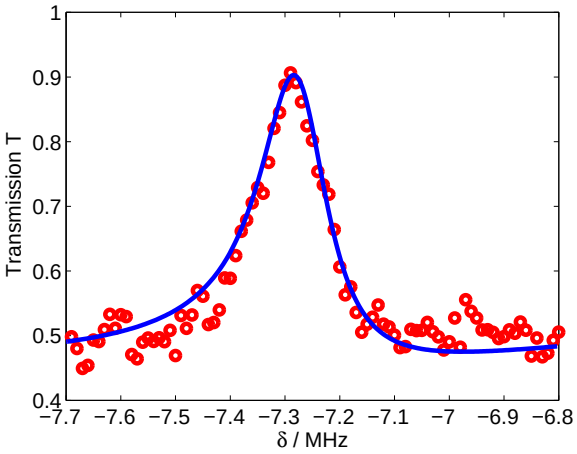

Fig. 13.2: Transmission spectrum of a 20 μs pulse at a coupling laser Rabi-frequency of 1.2 MHz. The absorptive and dispersive parts in the signal can be seen. The frequency offset of $\delta_0 = -7.27$ MHz corresponds to the differential quadratic Zeeman shift between the two ground state levels. This offset does not depend on the lasers and can thus be used to calibrate the magnetic offset field. From the fitted blue line we obtained $B = 129.7$ G, which verified the numerical simulation of the magnetic coils. For the fit we used equation 4.34 as an approximation.

The value for the phase $\phi = 4.95$ was obtained from the fits of all measurements. The curve was fitted with equation 4.34 and yielded a bandwidth of $\sigma = 100$ kHz, a ground state decay rate $\gamma = 8$ kHz and $\delta_0 = -7.27$ MHz for the frequency offset due to the quadratic Zeeman shift. The ground state decay rate γ usually corresponds to collisions between the atoms as well as collisions with the background gas. The collision rate can usually be neglected, especially in case of large coupling laser Rabi-frequencies. But it can also correspond to a transient effect: for low coupling laser Rabi-frequencies, a steady state in the atomic population cannot be reached within the time of a short probe pulse. Thus, photons can be absorbed without being re-emitted, which shows the same empiric behavior as the collisional loss of polaritons and leads to non-negligible values of γ.
The data in figures 13.3 and 13.4 show the results of the measurements with the 5 μs and the 20 μs pulses, respectively. For large coupling laser Rabi-frequencies,

the coupling laser broadens the line width, while for lower Rabi-frequencies, the pulse length is the limiting factor.

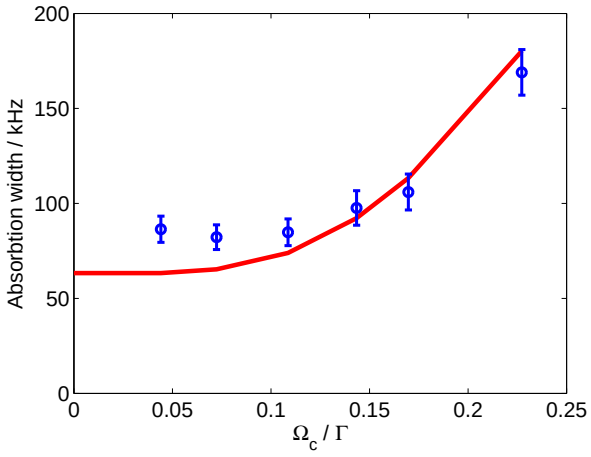

Fig. 13.3: Theory curve and EIT measurement with 5 μs pulses. The figure shows the transparency width (Gaussian $1/e$-radius of the symmetric part) depending on the Rabi-frequency of the coupling laser. The probe pulses contain $3 \cdot 10^5$ photons within the size of the cloud, which correspond to a maximum Rabi-frequency of 190 kHz. The error bars reflect the uncertainty in the phase ϕ.

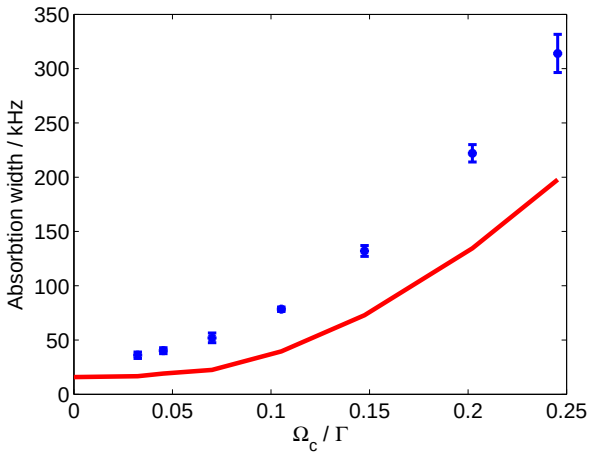

Fig. 13.4: Theory curve and EIT measurement with 20 μs pulses. The figure shows the transparency width (Gaussian $1/e$-radius of the symmetric part) depending on the Rabi-frequency of the coupling laser. The pulses contain $2 \cdot 10^6$ photons within the size of the cloud, which correspond to a maximum Rabi-frequency of 220 kHz. The width is much narrower than the one of the 5 μs pulses.

The solid curves show the line width that should in theory be obtainable with our achieved cloud parameters. For 5 μs probe pulses with large Rabi-frequencies, the measurements are in good accordance with the theory. For all others, the measured line widths are broader than the theory for an optical density of 0.76 predicts. We attribute these small discrepancies to a decrease in the optical density of the trapped cloud during the experimental measurements. Smaller optical densities can be caused by a reduced number of optically trapped atoms, which is typically observed in the course of the day, and lead to broader theoretically expected line widths. The theory curve is plotted for an optical density of 0.76.
The lack of sufficient coupling light results in an incomplete transparency and limits the relative hight of the EIT peak in the signal. This can be seen in figure 13.5.

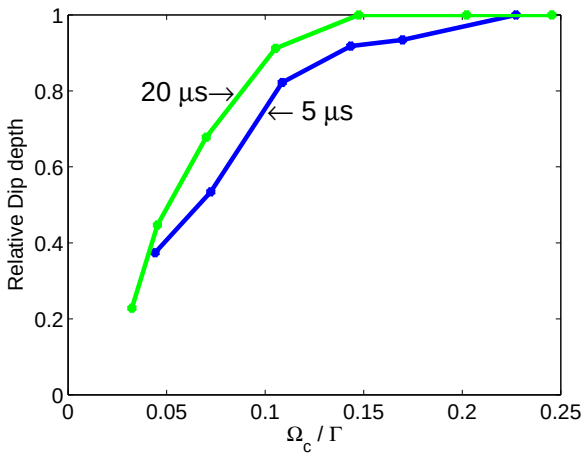

Fig. 13.5: EIT measurement with 5 μs and the 20 μs pulses. The figure shows the relative hight of the EIT peak depending on the Rabi-frequency of the coupling laser. The decrease for small Rabi-frequencies corresponds to the transient effect that a steady state cannot be reached here within the time of a short probe pulse.

To obtain a very narrow line width, a measurement was made with 100 μs long pulses, containing $3.9 \cdot 10^6$ photons within the size of the cloud, which corresponds to a maximum Rabi-frequency of 360 kHz. Figure 13.6 shows the result for a coupling laser Rabi-frequency of 590 kHz. For lower values, the induced transparency was too low.
Due to inefficient EIT, the absorptive part is so low that it is not visible anymore. Instead, due to a large phase shift, the dispersive part of the signal gets enhanced, compared to the measurements shown before.

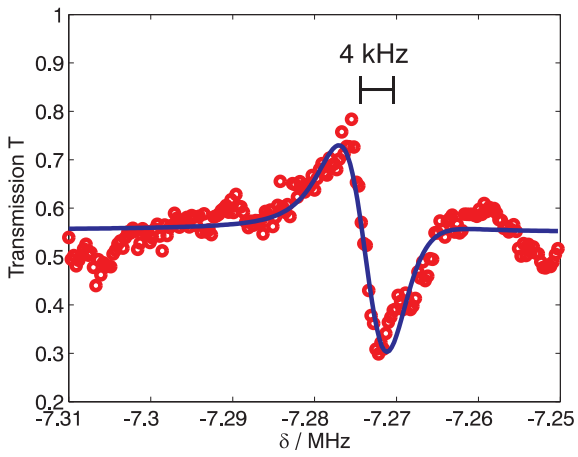

Fig. 13.6: EIT measurement with a 100 μs pulse: the line width was reduced to 4 kHz. The transparency is so low that only the dispersive part of the signal can be seen.

To enhance the dispersive effect, the σ^--intensity admixture a^2 was increased to 25 %, which also resulted in a different differential phase shift $\phi = 4.1$. With a Gaussian $1/e$-half width of 4 kHz, this is the narrowest EIT signal measured in ultracold atoms [HHDB99, BBG+04]. A similar method of measurement has recently been demonstrated with a vapor cell in a Sagnac interferometer [PAH06, XLJGB95].
Narrower signals of ~ 30 Hz have been measured in buffer gas cells, where one is not limited by pulse lengths [BNWM97, ENH00].

Now we can finally use equation 4.30 to calculate the velocity of light inside the atomic medium. Using the values from the narrowest measurement, $\Omega_c = 590$ kHz, $\sigma_p = 4$ kHz and $l = 2 \cdot 126\,\mu$m$= 252\,\mu$m, we get

$$v_{gr} = \frac{c}{1 + \frac{c\,\Omega_c^2}{4\,l\,\sigma_p^2\,\Gamma}} = \frac{c}{1.8 \cdot 10^8} = 1.7\,\frac{\mathrm{m}}{\mathrm{s}}\,. \tag{13.1}$$

Also, first measurements were made on light storage in the atomic cloud. But as the density was far too low (see appendix D), the results remain questionable and will not be presented here.

14. Summary and Outlook

In this thesis, I have shown the design of an experiment that provides the feasibility to detect and count single photons with near unity efficiency. Furthermore, this experiment has been used to measure electromagnetically induced transparency in optically trapped rubidium atoms with very narrow linewidths.

Experimental Setup

In this experiment, atoms are first captured magneto-optically in a vacuum chamber before they are transferred into an optical dipole trap, which is operated in a crossed beam geometry. The laser system for operating the MOT consists of three diode lasers and a tapered amplifier, while the laser system for the optical dipole trap consists of one CO_2-laser. For generating the single photons, a Raman laser system has been set up. It consists of three diode lasers and has been used to measure electromagnetically induced transparency in optically trapped rubidium atoms.

Calculations

The feasibility to detect and count single photons has been shown theoretically with extensive calculations. They yielded a probability of detecting a single photon of

$$\eta_{1pd} = 99.9\,\% \; . \tag{14.1}$$

The other important quantity is the probability of not detecting a single photon when none arrives, which is

$$\eta_{0pd} = 99.3\,\% \; . \tag{14.2}$$

Furthermore, calculations on electromagnetically induced transparency and photon storage have been performed. These showed that very narrow EIT linewidths and long photon storage times can be achieved in sufficiently dense optically trapped rubidium clouds.

Experimental Results

The experiment has been used to capture up to $\sim 1.7 \cdot 10^9$ atoms at temperatures of $\sim 400\,\mu$K in the MOT.
Subsequently, a dark MOT phase was applied. There, the atom number was reduced to $9.3 \cdot 10^8$ and the density was $n_0 = 1.4 \cdot 10^{12}\,\mathrm{cm}^{-3}$. The temperature of the ensemble was reduced to $T_x = 40\,\mu$K and $T_z = 37\,\mu$K and the measured size of the cloud was $\sigma_x = 400\,\mu$m and $\sigma_z = 260\,\mu$m.
These atoms have been transferred into a single beam dipole trap as well as into a crossed beam dipole trap.

In the crossed beam trap, up to $3.4 \cdot 10^7$ atoms could be captured at a density of $n_0 = 2.3 \cdot 10^{11}\,\mathrm{cm}^{-3}$. The temperatures were $T_x = 200\,\mu$K and $T_z = 80\,\mu$K, which shows that the cloud is not in thermal equilibrium.
The cold sample has been used to perform absorption measurements, which have been used to characterize the dipole trap. Furthermore, absorption measurements have been made with an applied homogeneous offset field. This has been used to address the magnetic substates individually.
Finally, the setup has been used to measure electromagnetically induced transparency in pure optically trapped rubidium atoms for the first time. With a linewidth of 4 kHz, these measurements showed the narrowest EIT-based linewidth that has been measured in ultracold atoms. From this linewidth, a reduction of the group velocity of light to 1.7 m/s was deduced.

Outlook

The optical density achieved in this experiment is comparable to other experiments [CRGW03]. Since it has to be higher for efficient single photon detection, the next step will be to increase it. This can be done by forced evaporation of the atomic cloud. So far, this is not efficiently possible, as the atomic density in the dipole trap is too low, while the pressure in the chamber is too high.
Thus, the transfer of the atoms from the dark MOT into the dipole trap has to be optimized for getting a higher density. Additionally, the elliptical windows have to be sealed in a different way in order to decrease the leaking rate through them, which will result in a lower pressure and thus a longer lifetime.
With these conditions, the detection of single photons can be performed.

Part V

Appendices

Appendix A

Constants

A.1 The element rubidium

All relevant information on rubidium-87 can be obtained from [Ste02]. Here I will briefly summarize the most important magnitudes:

Symbol	**Denotation**	**Value [Ste02]**
λ_{D2}	Wavelength D2-transition	$780.246291629(11)\,\mathrm{nm}$
λ_{D1}	Wavelength D1-transition	$794.9788509(8)\,\mathrm{nm}$
α_0	Ground state polarizability	$h \cdot 0.0794(16)\,\mathrm{Hz/(V/cm)^2}$
$I_{sat,\,D2}$	Resonant saturation intensity D2	$1.669(2)\,\mathrm{mW/cm^2}$
$I_{sat,\,D1}$	Resonant saturation intensity D1	$4.484(5)\,\mathrm{mW/cm^2}$
$\langle \mathrm{g}\vert\vec{d}\vert\mathrm{e}\rangle_{D2}$	Transition matrix element D2	$3.584(4) \cdot 10^{-29}\,\mathrm{C{\cdot}m}$
$\langle \mathrm{g}\vert\vec{d}\vert\mathrm{e}\rangle_{D1}$	Transition matrix element D1	$2.537(3) \cdot 10^{-29}\,\mathrm{C{\cdot}m}$
d_{D2}	Effective far-detuned dipole moment D2	$2.069(2) \cdot 10^{-29}\,\mathrm{C{\cdot}m}$
d_{D1}	Effective far-detuned dipole moment D1	$1.4646(15) \cdot 10^{-29}\,\mathrm{C{\cdot}m}$

Symbol	**Denotation**	**Value [Ste02]**
T_M	Melting point	39.3 °C
T_B	Boiling point	688°C
I	Nuclear Spin	3/2
$\eta(^{87}\mathrm{Rb})$	Natural abundance	27.8 %

A.2 General constants

Symbol	**Denotation**	**Value [NIST07]**
k_B	Boltzmann's constant	$1.3806505 \cdot 10^{-23}$ J/K
$\hbar$	Planck's constant	$1.05457168\,10^{-34}$ Js
c	Light speed	$2.99792458 \cdot 10^{8}$ m/s
u	Atomic mass unit	$1.66053886 \cdot 10^{-27}$ kg
μ_B	Bohr magneton	$9.27400949 \cdot 10^{-24}$ Am^2
a_0	Bohr radius	$0.5291772108 \cdot 10^{-10}$ m
ε_0	Electric constant	$8.854187817 \cdot 10^{-12}$F/m

Appendix B

Crossed beam dipole trap

In this experiment it is advantageous to use a dipole trap that is created by two laser beams in a crossed geometry (see chapter 5.1). The two laser beams meet under an angle of $2\,\varphi$. We continue to denote the virtual axes of the two laser beams with the greek characters (ξ_1, υ_1, ζ_1) and (ξ_2, υ_2, ζ_2) to distinguish between them and the real axes of the laboratory system, denoted in latin characters (x, y, z), as shown in figure B.1).

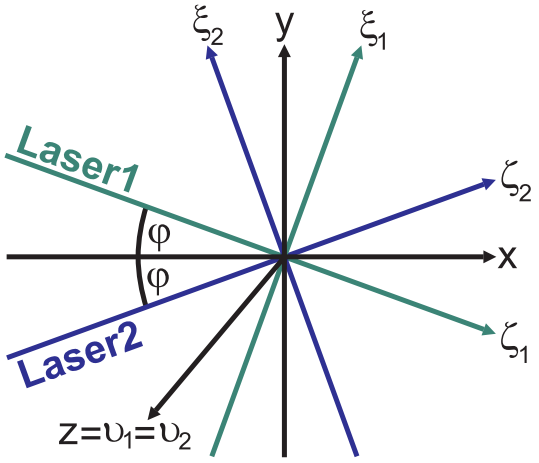

Fig. B.1: The coordinate systems of the two dipole lasers (blue and green) and the one of the laboratory (black).

We assume that both beams have the same power P as well as the same waist and can transform the total potential

$$\begin{aligned} V = & - \frac{\alpha P}{c\,\varepsilon_0 \pi w_0^2} \frac{1}{(1+\frac{\zeta_1^2\lambda^2}{\pi^2 w_0^4})} \exp\left(-\frac{2\rho_1^2}{w_0^2(1+\frac{\zeta_1^2\lambda^2}{\pi^2 w_0^4})}\right) \\ & - \frac{\alpha P}{c\,\varepsilon_0 \pi w_0^2} \frac{1}{(1+\frac{\zeta_2^2\lambda^2}{\pi^2 w_0^4})} \exp\left(-\frac{2\rho_2^2}{w_0^2(1+\frac{\zeta_2^2\lambda^2}{\pi^2 w_0^4})}\right) \end{aligned} \tag{B.1}$$

via the substitutions

$$\rho_1 = \sqrt{\xi_1^2 + \upsilon_1^2} \tag{B.2}$$

$$\rho_2 = \sqrt{\xi_2^2 + \upsilon_2^2} \tag{B.3}$$

and the coordinate transformations

$$\begin{pmatrix} \xi_1 \\ \upsilon_1 \\ \zeta_1 \end{pmatrix} = \begin{pmatrix} \sin\varphi & \cos\varphi & 0 \\ 0 & 0 & 1 \\ \cos\varphi & -\sin\varphi & 0 \end{pmatrix} \begin{pmatrix} x \\ y \\ z \end{pmatrix}$$

$$\begin{pmatrix} \xi_2 \\ \upsilon_2 \\ \zeta_2 \end{pmatrix} = \begin{pmatrix} -\sin\varphi & \cos\varphi & 0 \\ 0 & 0 & 1 \\ \cos\varphi & \sin\varphi & 0 \end{pmatrix} \begin{pmatrix} x \\ y \\ z \end{pmatrix} \tag{B.4}$$

into the lab frame:

$$\begin{aligned} V = & - \frac{\alpha P}{c\,\varepsilon_0 \pi w_0^2} \frac{1}{\left(1 + \frac{(\cos\varphi\, x - \sin\varphi\, y)^2 \lambda^2}{\pi^2 w_0^4}\right)} \exp\left(-\frac{2((\sin\varphi\, x + \cos\varphi\, y)^2 + z^2)}{w_0^2 \left(1 + \frac{(\cos\varphi\, x - \sin\varphi\, y)^2 \lambda^2}{\pi^2 w_0^4}\right)}\right) \\ & - \frac{\alpha P}{c\,\varepsilon_0 \pi w_0^2} \frac{1}{\left(1 + \frac{(\cos\varphi\, x + \sin\varphi\, y)^2 \lambda^2}{\pi^2 w_0^4}\right)} \exp\left(-\frac{2((\cos\varphi\, y - \sin\varphi\, x)^2 + z^2)}{w_0^2 \left(1 + \frac{(\cos\varphi\, x + \sin\varphi\, y)^2 \lambda^2}{\pi^2 w_0^4}\right)}\right) \end{aligned} \tag{B.5}$$

Now we can analogous to section 2.3 derive the potential to the three axes and compare it with the harmonic oscillator:

$$\begin{aligned} V_x(y=0,\, z=0) &= -\frac{2\alpha P}{\pi c\,\varepsilon_0 w_0^2} \frac{1}{(1 + \frac{\cos^2\varphi\, x^2 \lambda^2}{\pi^2 w_0^4})} \exp\left(-\frac{2\sin^2\varphi\, x^2}{w_0^2 (1 + \frac{\cos^2\varphi\, x^2 \lambda^2}{\pi^2 w_0^4})}\right) \\ &\approx \frac{2\alpha P}{\pi c\,\varepsilon_0 w_0^4} \left(2\sin^2\varphi + \frac{\cos^2\varphi\, \lambda^2}{\pi^2 w_0^2}\right) x^2 \end{aligned} \tag{B.6}$$

$$\begin{aligned} V_y(x=0,\, z=0) &= -\frac{2\alpha P}{\pi c\,\varepsilon_0 w_0^2} \frac{1}{(1 + \frac{\sin^2\varphi\, y^2 \lambda^2}{\pi^2 w_0^4})} \exp\left(-\frac{2\cos^2\varphi\, y^2}{w_0^2 (1 + \frac{\sin^2\varphi\, y^2 \lambda^2}{\pi^2 w_0^4})}\right) \\ &\approx \frac{2\alpha P}{\pi c\,\varepsilon_0 w_0^4} \left(2\cos^2\varphi + \frac{\sin^2\varphi\, \lambda^2}{\pi^2 w_0^2}\right) y^2 \end{aligned} \tag{B.7}$$

$$\begin{aligned} V_z(x=0,\, y=0) &= -\frac{2\alpha P}{\pi c\,\varepsilon_0 w_0^2} e^{-\frac{2z^2}{w_0^2}} \\ &\approx \frac{4\alpha P}{\pi c\,\varepsilon_0 w_0^4} z^2 \end{aligned} \tag{B.8}$$

This leads to the trapping frequencies:

$$\omega_{x,\,y=0,\,z=0} = \frac{2}{w_0^2}\sqrt{\frac{\alpha P}{m\,\pi\,c\,\varepsilon_0}\left(2\sin^2\varphi + \frac{\cos^2\varphi\,\lambda^2}{\pi^2 w_0^2}\right)} \tag{B.9}$$

$$\omega_{y,\,x=0,\,z=0} = \frac{2}{w_0^2}\sqrt{\frac{\alpha P}{m\,\pi\,c\,\varepsilon_0}\left(2\cos^2\varphi + \frac{\sin^2\varphi\,\lambda^2}{\pi^2 w_0^2}\right)} \tag{B.10}$$

$$\omega_{z,\,x=0,\,y=0} = \frac{2}{w_0^2}\sqrt{\frac{2\,\alpha P}{m\,\pi\,c\,\varepsilon_0}} \tag{B.11}$$

Because the situation is not circular anymore, there are now three different trap frequencies instead of two (equations 2.14 and 2.15).

The trap depth of a red detuned laser is given by the potential at the origin

$$|V(x=0,\,y=0,\,z=0)| = \frac{2\alpha P}{\pi c\,\varepsilon_0 w_0^2}\,. \tag{B.12}$$

For pulling unwanted atoms out of the dipole trap, a magnetic field gradient will be applied. This gradient is parallel to the y-axis (see figure B.1) and must be higher than the maximum gradient of the dipole trap along the same direction. The gradient for the dipole trap is given by the derivative of the exact term of equation B.7

$$\frac{dV_y(x=0,\,z=0)}{dy} = \dots\,, \tag{B.13}$$

which yields a quite long expression. The maximum gradient of the trap is found at a distance y given by

$$\frac{d^2V_y(x=0,\,z=0)}{dy^2} \stackrel{!}{=} 0\,, \tag{B.14}$$

which has unfortunately no analytic solution. Thus, the gradient has to be determined numerically, as it has been done in section 8.1.

Appendix C

The 3-level-Λ-system in second quantization

Another extension of the three-level-atom occurs, when light fields with only few photons are used. Then, the so far classical light fields must be quantized as well, which is called the second quantization [Sch01]. We assume to have a classical coupling laser and a quantized probe laser field (as it is the case for single photon detection). Then, every atomic state corresponds to a photon number state in the probe field. When the atom is in state $|\mathrm{a}\rangle$, there shall be $m+1$ photons in the probe beam. When the atom absorbs one photon and gets into state $|\mathrm{b}\rangle$ or $|\mathrm{c}\rangle$, there will be m photons left.

$$|a, m+1\rangle = \begin{pmatrix} 0 \\ 0 \\ 1 \end{pmatrix}; \qquad |b, m\rangle = \begin{pmatrix} 0 \\ 1 \\ 0 \end{pmatrix}; \qquad |c, m\rangle = \begin{pmatrix} 1 \\ 0 \\ 0 \end{pmatrix} \tag{C.1}$$

The coupled atomic-photonic state is then given by

$$|\psi\rangle = c_{|a\rangle}|a, m+1\rangle + c_{|b\rangle}|b, m\rangle + c_{|c\rangle}|c, m\rangle = \begin{pmatrix} c_c \\ c_b \\ c_a \end{pmatrix}, \tag{C.2}$$

where $c_{|a\rangle}$, $c_{|b\rangle}$ and $c_{|c\rangle}$ denote the populations in the indicated states. Analogous to section 4.1, this leads to the Hamiltonian

$$\begin{aligned} \frac{\hat{H}}{\hbar} &= \omega_{|a\rangle}\ |a, m+1\rangle\langle a, m+1|\ + \omega_{|b\rangle}\ |b, m\rangle\langle b, m|\ + \omega_{|c\rangle}\ |c, m\rangle\langle c, m| \\ &+ g_p \cos(\omega_p t)\sqrt{m+1}\ |a, m+1\rangle\langle c, m| \\ &+ g_p^\star \cos(\omega_p t)\sqrt{m+1}\ |c, m\rangle\langle a, m+1| \\ &+ \Omega_c \cos(\omega_c t)\ |b, m\rangle\langle c, m| \\ &+ \Omega_c^\star \cos(\omega_c t)\ |c, m\rangle\langle b, m| \end{aligned} \tag{C.3}$$

and via the rotating wave approximation and the Liouville equation to the density matrix elements

$$\begin{aligned}
\dot{\rho}_{cc} &= -\Gamma\rho_{cc} - \frac{i}{2}(\Omega_c\rho_{cb} - \Omega_c^\star\rho_{bc}) - \frac{i}{2}\sqrt{m+1}\,(g_p\rho_{ca} - g_p^\star\rho_{ac}) \\
\dot{\rho}_{bb} &= +\frac{i}{2}(\Omega_c\rho_{cb} - \Omega_c^\star\rho_{bc}) \\
\dot{\rho}_{aa} &= +\frac{i}{2}\sqrt{m+1}\,(g_p\rho_{ca} - g_p^\star\rho_{ac}) \\
\dot{\rho}_{cb} &= (-\frac{\Gamma}{2} + i\Delta_c)\rho_{cb} - \frac{i}{2}\Omega_c^\star(\rho_{bb} - \rho_{cc}) - \frac{i}{2}\sqrt{m+1}\,g_p^\star\rho_{ab} \\
\dot{\rho}_{bc} &= (-\frac{\Gamma}{2} - i\Delta_c)\rho_{bc} + \frac{i}{2}\Omega_c(\rho_{bb} - \rho_{cc}) + \frac{i}{2}\sqrt{m+1}\,g_p\rho_{ba} \\
\dot{\rho}_{ca} &= (-\frac{\Gamma}{2} + i\Delta_p)\rho_{ca} - \frac{i}{2}\sqrt{m+1}\,g_p^\star(\rho_{aa} - \rho_{cc}) - \frac{i}{2}\Omega_c^\star\rho_{ba} \\
\dot{\rho}_{ac} &= (-\frac{\Gamma}{2} - i\Delta_p)\rho_{ac} + \frac{i}{2}\sqrt{m+1}\,g_p(\rho_{aa} - \rho_{cc}) + \frac{i}{2}\Omega_c\rho_{ab} \\
\dot{\rho}_{ba} &= (i\Delta_p - i\Delta_c)\rho_{ba} - \frac{i}{2}(\Omega_c\rho_{ca} - \sqrt{m+1}\,g_p^\star\rho_{ac}) \\
\dot{\rho}_{ab} &= (i\Delta_c - i\Delta_p)\rho_{ab} + \frac{i}{2}(\Omega_c^\star\rho_{ac} - \sqrt{m+1}\,g_p\rho_{cb})\,. \qquad \text{(C.4)}
\end{aligned}$$

Here, the Rabi-frequency of the probe laser Ω_p has been replaced with the vacuum Rabi-frequency g_p [Sch01]. The vacuum Rabi-frequency is identical to the single photon Rabi-frequency described in section 3.1. It can be seen that the equations above are identical to the equations in section 4.2. This shows that the Rabi-frequency of single photons described in section 3.1 is identical to the second quantization.
The equations above have been used to calculated the transition probabilities of the single photon detection scheme.

Appendix D

Stimulated Raman Adiabatic Passage

In this chapter, I will briefly describe the main condition for storing light in an atomic medium: the stored pulse must spatially fit into the atomic cloud. If not, only a part of it will be stored and the other part will be transmitted due to EIT. The length of the stored pulse is given by its velocity v_{gr} and its total duration T_p, which must match the length l of the cloud. They are connected via

$$v_{gr} = \frac{l}{T_p} \,. \tag{D.1}$$

Combining this with equation 4.28, we get the required Rabi-frequency

$$\Omega_c = \sqrt{4\Gamma\,\sigma_p^2\,(T_p - l/c)} \,. \tag{D.2}$$

Using the measured cloud length of $l = 2\cdot\sigma_y = 2\cdot 126\,\mu\text{m} = 252\,\mu\text{m}$, the minimum used total pulse length $T_p = 20\,\mu\text{s}$ and the minimum possible EIT width $\sigma_p = 63\,\text{kHz}$ at this pulse length (see chapter 13), we get

$$\Omega_c = 2\pi\,3.2\cdot 10^6\,\text{s}^{-1} \,. \tag{D.3}$$

Then, we can use equation 4.26 to achieve the minimum required atomic density

$$n_0 = \frac{\Omega_c^4 \varepsilon_0 \hbar}{8\sigma_p^2 \Gamma |\mu_{ac}|^2 k l} = 3\cdot 10^{12}\text{cm}^{-3} \,. \tag{D.4}$$

As the achieved density in the dipole trap was a factor 20 lower (see chapter 11), the density will have to be increased before a meaningful measurement on photon storage can be performed.

Appendix E

Photon statistics

To perform the single photon detection, it would be desirable to use single photons from a deterministic source. As deterministic high efficiency narrow bandwidth single photon sources are not yet available, classical light pulses have to be used instead. Therefore, I will briefly discuss the behavior of such pulses in this chapter.

Even if the parameters for classical light pulses are identical, the photon number within a pulse varies due to quantum theory from pulse to pulse [Sch01]. When we denote the average number of photons within a pulse with α, the average pulse energy is given by

$$E_{pulse} = \hbar\omega\alpha. \tag{E.1}$$

The probability to find m photons within this pulse is given by the Poisson distribution

$$W_m = \frac{\alpha^2}{m!}\, e^{-|\alpha|}. \tag{E.2}$$

The normalization of this equation is given by

$$\sum_{l=0}^{\infty} W_l = 1, \tag{E.3}$$

which leads to

$$\sum_{l=0}^{\infty} W_l\, l = \alpha. \tag{E.4}$$

This photon number distribution is obtained from any classical pulse and complicates the single photon detection: if one puts in average one photon into a pulse, it is not known how many photons have been in each pulse. Therefore, only a statistical result can be obtained.
This problem can be circumvented by the use of a deterministic single photon

source, that creates single photon Fock states instead of the coherent states described above.
As these photon sources are not yet available, another possibility to circumvent this problem is the use of parametric down-conversion. Here, always an even number of photons is created from one pulse. One photon is used as a reference photon and detected by a classical photo detector, the other one goes to the single photon detector, which yields a correlation measurement.

Appendix F

Deutsche Zusammenfassung

Im Rahmen dieser Arbeit wurde ein Experiment zur Kühlung von Rubidiumatomen bis in den μK-Bereich aufgebaut. Das Ziel dieses Experiments ist die Verwendung dieser ultrakalten Atomwolke zur Detektion von Einzelphotonen. Dieser Detektor stellt einen wichtigen Bestandteil eines Quantencomputers dar, der Einzelphotonen als Informationsträger nutzt [KLM01]. Der Aufbau wurde genutzt um Messungen zur elektromagnetisch induzierten Transparenz, einem Effekt der lichtundurchlässige Materie transparent macht, durchzuführen. Dieser Effekt kann genutzt werden, um die Gruppengeschwindigkeit von Licht zu reduzieren.
Die Hauptbestandteile des Experiments sind eine Vakuumkammer, Magnetspulen und verschiedene Lasersysteme: die Vakuumkammer besteht aus einer Hauptkammer, in der die Atome zuerst von Rubidiumdispensern verdampft, dann magneto-optisch und anschließend in einer optischen Dipolfalle gefangen werden, und einem Pumpkreuz, wo das Ultrahochvakuum erzeugt wird. Mehrere Magnetspulen befinden sich an der Kammer um die erforderlichen Magnetfelder zu erzeugen.

Schema des Experiments

Sobald die Atomwolke die idealen Parameter in Temperatur, Dichte und Atomzahl erreicht, werden die Einzelphotonen in die Wolke geschossen, wo sie den Zustand eines Atoms pro eintreffendem Photon verändern. Ein sogenannter Koppellaser wird zusammen mit den Einzelphotonen auf die Wolke geschossen. Dieser sichert eine effiziente Veränderung des atomaren Zustands. Diese Veränderung wird anschließend durch Fluoreszenz detektiert. Weil dieses Schema sehr empfindlich auf die Polarisation der Einzelphotonen ist, wird eine wohl definierte Magnetisierungsachse benötigt. Diese kann nur von einem hohen

und homogenen Magnetfeld erzeugt werden. Die einzige Atomfalle, die bei so einem Magnetfeld effizient betrieben werden kann ist eine Dipolfalle, die deshalb in diesem Experiment benutzt wird.

Da die Atome, welche nicht durch Einzelphotonen in einen anderen Zustand transferriert wurden, ebenfalls Licht streuen und damit den Detektionsprozess stören, müssen sie vor der Detektion der transferierten Atome aus der Falle gebracht werden. Dies kann mit einem starken magnetischen Gradienten erzielt werden: dieser zieht alle Atome, welche in einem magnetischen Unterzustand gesammelt wurden, aus der Falle, während die in einen magnetisch neutralen Zustand transferierten Atome in der Falle zur Detektion zurückbleiben.

Damit sieht der komplette Detektionsprozess folgendermaßen aus:

1. Kühlung der Atome
Zuerst werden ultrakalte Rubidiumatome in einer Ultrahochvakuumkammer gefangen. Dabei werden sie zunächst in einer magneto-optischen Falle (MOT) eingeschlossen und gekühlt, bevor sie anschließend in eine optische Dipolfalle transferiert werden. In dieser werden sie weiter gekühlt und in einem definierten Unterzustand präpariert.

2. Adiabatischer Transfer
Anschließend werden die Einzelphotonen zusammen mit einem Koppellaser in die Wolke geschickt. Dieser stellt sicher, dass jedes Photon ein Atom in einen definierten Zustand transferiert. Dabei durchlaufen die Laserintensitäten eine STIRAP-Sequenz.

3. Entfernen der unerwünschten Atome
Nach diesem Transfer müssen die Atome, welche nicht transferiert wurden, mit einem starken Magnetfeldgradienten aus der Falle gezogen werden.

4. Der Detektionsprozess.
Nun werden die transferierten Atome durch Fluoreszenzdetektion gezählt.

Die Idee

Im Unterschied zu dem oben beschriebenen Schema besteht die ursprüngliche Idee [Ima02] darin, die ultrakalten Atome in einer Magnetfalle zu fangen. Wie in den nächsten Abschnitten gezeigt wird ist der Einzelphotonentransfer sehr empfindlich auf die Polarisationen der Einzelphotonen und des Koppellasers und eine falsche Polarisation würde eine Verringerung der Detektionseffizienz bedeuten.

Die Reinheit der Polarisation, die mit polarisierenden Strahlteilerwürfeln und λ-Platten erreicht werden kann, liegt in der Größenordnung von 1 ‰ [BHN07], welche für das vorgeschlagene Schema ausreichend ist. Aber gleichzeitig muss die Quantisierungsachse, welche durch das Magnetfeld vorgegeben wird, sehr homogen sein. Weil das Feld in einer Magnetfalle nicht homogen ist gibt es keine Quantisierungsachse, die über die ganze Wolke parallel zum Lichtvektor ist. Deswegen kann diese Art von Falle nicht benutzt werden.
Außerdem existieren immer Streufelder, welche von Tag zu Tag variieren und deshalb niemals vollständig kompensiert werden können. Deswegen ist ein hohes Offsetfeld notwendig, weil dadurch der Einfluss der Streufelder auf das Gesamtfeld verringert wird. Dieses hohe Offsetfeld ist ein weiterer Grund, warum eine Magnetfalle nicht benutzt werden kann. Es existieren zwar Magnetfallen mit hohem Offsetfeld, aber der Aufwand für die hierbei verwendeten supraleitenden Spulen ist nicht gerechtfertigt.

Kühlung der Atome

Die Lösung besteht nun darin, nach der MOT-Ladephase eine optische Dipolfalle zu benutzen. Diese Falle erzeugt den Einschluss der Atome und ein zusätzliches hohes magnetisches Offsetfeld erzeugt bezüglich des Lichtvektors eine gut definierte Richtung der Quantisierungsachse.
In dieser Falle werden die Atome evaporativ bis auf $\sim 750\,\mathrm{nK}$ gekühlt. Zu diesem Zeitpunkt sind die Dichte und Temperatur nur knapp oberhalb der kritischen Parameter zum Erreichen eine Bose-Einstein-Kondensats (BEC).
Dipolfallen können bei Wellenlängen um 1064 nm relativ einfach realisiert werden, weil dieses Licht die üblichen optischen Fenster von Vakuumkammern durchdringt. Dieses Licht ist sowohl gegenüber dem D1 als auch dem D2 Übergang in Rubidium stark verstimmt, weshalb die Streuung dieses Lichts stark unterdrückt ist. Trotzdem sind Streuprozesse möglich, wenn die Intensität des Lichts entsprechend erhöht wird. Dies führt zum Übergang von Atomen von dem anfänglichen Grundzustand in einen unerwünschten Grundzustand. Weil bereits ein einzelnes Atom in einem unerwünschten Zustand den kompletten Detektionsprozess zerstören würde (ein Photon würde gezählt obwohl keines vorhanden war) wird in diesem Experiment ein CO_2-laser eingesetzt. Dessen Licht im fernen Infrarot ist gegenüber der D1 als auch der D2 Linie so stark verstimmt, dass Streuprozesse auf weniger als 1 Photon pro Sekunde unterdrückt sind [CRGW03]. Der Nachteil ist, dass dieses Licht nicht durch gewöhnliche Glasfenster geschickt werden kann und stattdessen Zinkselenid (ZnSe) Fenster benutzt werden müssen.
Um die optische Dichte der Wolke zu erhöhen wird diese in länglicher Form präpariert. Obwohl eine Einstrahlfalle dafür ideal wäre kann diese nicht benutzt

werden, weil die Einzelphotonen mit dem CO_2-Laser nicht überlagert werden können, da die ZnSe-Fenster die Einzelphotonen absorbieren würden. Als Lösung wurde nun eine gekreuzte Dipolfalle gewählt. Die Strahlen der Dipolfalle treffen sich unter einem Winkel von 60° und erzeugen eine leicht verlängerte Wolke. Die Einzelphotonen werden dann entlang der langen Achse in die Wolke geschickt.

Da es nicht möglich ist alle Atome effektiv in den Zustand $|a\rangle$ zu pumpen, werden die Atome zuerst in den Zustand $|m\rangle$ gepumpt und dann mit einem Mikrowellen-π-Puls in den Zustand $|a\rangle$ transferiert. Das komplette Detektionsschema ist in Abbildung F.1 zu sehen.

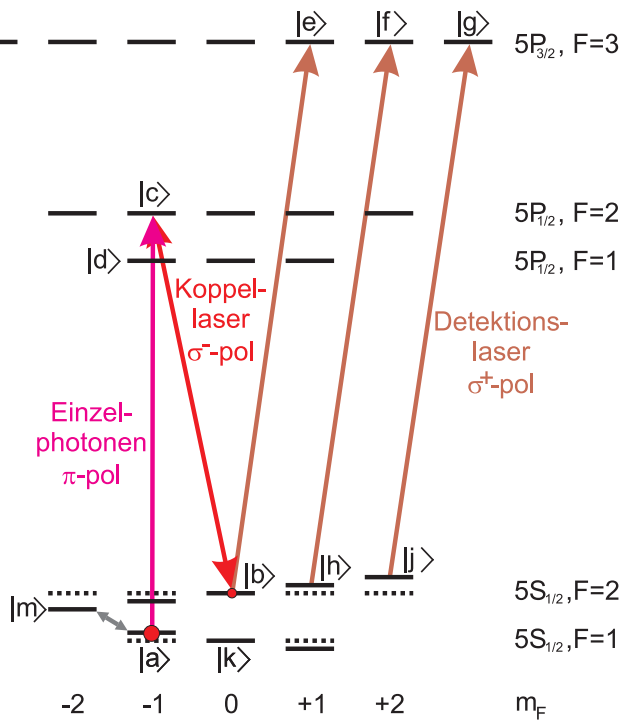

Abb. F.1: Niveauschema von ^{87}Rb, welches benutzt wird um die Einzelphotonen zu detektieren. Alle relevanten Zustände werden gezeigt, inklusive der Laser, welche die Zustände während dem Einzelphotonentransfer und der anschließenden Detektion miteinander koppeln. Des weiteren wird der Mikrowellenübergang, welcher am Ende des optischen Pumpens benutzt wird, als grauer Pfeil gezeigt. Die D1 Linie wird für den Einzelphotonenübergang benutzt und die D2 Linie für den Detektionsprozess.

Adiabatischer Übergang

Dann werden die Einzelphotonen, welche auf dem $|a\rangle$–$|c\rangle$-Übergang resonant sind, zusammen mit einem Koppellaser in die Wolke geschickt. Der Koppellaser, welcher auf dem $|b\rangle$–$|c\rangle$-Übergang resonant ist, sorgt dafür, dass die Atome

in dem definierten Zustand $|b\rangle$ enden. Um einen effizienten Übergang zu erhalten werden die Intensitäten gemäß einer stimulierten adiabatischen Ramanpassage (STIRAP) moduliert [BTS98]. Mit dieser ist es möglich, eine 100 %ige Transfereffizienz zu erreichen [GRSB90]. Sie wird in Abbildung F.2 gezeigt.

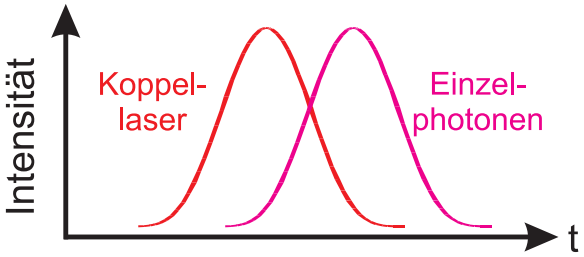

Abb. F.2: Pulssequenz des Koppel- und des Einzelphotonenlasers.

Bei dieser Sequenz wird der Koppellaser noch ehe die Einzelphotonen ankommen hochgefahren um eine Quanteninterferenz zwischen zwei Zuständen (z.B. $|b\rangle$ and $|c\rangle$) zu erzeugen. Dann wird er langsam heruntergefahren, während der Probelaser (hier die Einzelphotonen) langsam hochgefahren (und anschließend wieder heruntergefahren) wird.
Die Polarisationen der Ramanlaser sind so eingestellt, dass sie die Zustände $|a\rangle$, $|c\rangle$ and $|b\rangle$ mit den in Abbildung 1.1 gezeigten Polarisationen koppeln. In dieser Konfiguration sind die Einzelphotonen π-polarisiert, weil der Clebsch-Gordan-Koeffizient des $|a\rangle$–$|c\rangle$-Übergangs höher ist als der Clebsch-Gordan-Koeffizient des $|a\rangle$–$|d\rangle$-Übergangs, was in einer höheren optischen Dichte für die Einzelphotonen resultiert.

Entfernen der unerwünschten Atome

Der ursprüngliche Vorschlag gibt noch ein weiteres Problem auf: ein detektierbares Atom streut etwa 10^4 Photonen pro ms. Aufgrund des Raumwinkels ($\sim$ 1 %) und der Detektionseffizienz ($\sim$ 70 %) werden etwa 70 gestreute Photonen detektiert. Aber die Atome, welche im Zustand $|a\rangle$ bleiben streuen ebenfalls das für sie nichtresonante Fluoreszenzlicht. Aufgrund der hohen Verstimmung (6.8 GHz) ist die Streurate um einen Faktor 10^6 unterdrückt. Bei angenommenen 10^6 Atomen in diesem Zustand addiert dies einen Offset in der Größenordnung von 1 zum Detektionssignal. Dies stellt soweit kein Problem dar, weil dieser Offset wegen der hohen Atomzahl sehr konstant ist. Aber aufgrund des atomaren Zerfalls endet im Schnitt nach zwei Streuprozessen ein Atom in einem $|F = 2\rangle$ Grundzustand, in dem es von den Atomen, welche durch Einzelphotonen transferiert wurden, nicht mehr unterscheidbar ist. Somit nimmt das Fluoreszenzlicht exponentiell zu und eine Einzelphotonendetektion ist nicht mehr möglich. Deshalb müssen alle Atome im Zustand $|a\rangle$ vor dem Detektionsprozess entfernt werden.

Dies kann durch Anlegen eines starken magnetischen Feldgradienten parallel zum Offsetfeld erreicht werden. Bei dieser Konfiguration bleibt die magnetische Feldrichtung erhalten und der Gradient kann leichter erzeugt werden. Dieser Gradient zieht nun alle Atome, die sich nicht in den magnetisch neutralen Zuständen $|k\rangle$ und $|b\rangle$ befinden, aus der Dipolfalle.
Dafür muss die Dipolfalle flach genug sein und wird deshalb vor der STIRAP-Sequenz heruntergefahren.

Der Detektionsprozess

Die transferierten Atome werden nun durch Fluoreszenz detektiert. Nach einige Übergängen zwischen den Zuständen $|b\rangle$, $|e\rangle$, $|h\rangle$ und $|f\rangle$ werden die Atome im Zustand $|j\rangle$ enden und Licht auf dem geschlossenen $|j\rangle$–$|g\rangle$-Übergang streuen. Dieses Licht wird dann mit einer hocheffizienten Em-CCD-Kamera detektiert [MSK$^+$03, DAK$^+$05, WVS$^+$06].
Die Intensität des gestreuten Lichts ist dann proportional zur Anzahl der Atome im Zustand $|j\rangle$, welche selbst proportional zur Anzahl der ankommenden Einzelphotonen ist.

Über diese Arbeit

Im Rahmen dieser Arbeit wurde das Experiment entworfen und aufgebaut. Um die optimalen Parameter zu bestimmen wurden Rechnungen durchgeführt. Die Rubidiumatome wurden in der MOT und anschließenend sowohl in einer Einstrahl-Dipolfalle als auch in der gekreuzten Dipolfalle gefangen. Diese optisch gefangen Atome wurden letztendlich verwendet um mit dem Ramanlasersystem elektromagnetisch induzierte Transparenz zu messen.
Der Entwurf, der Aufbau und die Messungen sind der Inhalt dieser Arbeit.

Experimenteller Aufbau

Wie in den vorherigen Abschnitten erwähnt, wurde eine gekreuzte Dipolfalle unter einem Winkel von 60° verwendet. Da die ZnSe-Linsen aufgrund der großen Wellenlänge des CO_2-Lasers sehr nah an das Kammerzentrum gebracht werden müssen, blockieren sie einen Großteil des optischen Zugangs zur Kammer, welche in Abbildung F.3 dargestellt ist.

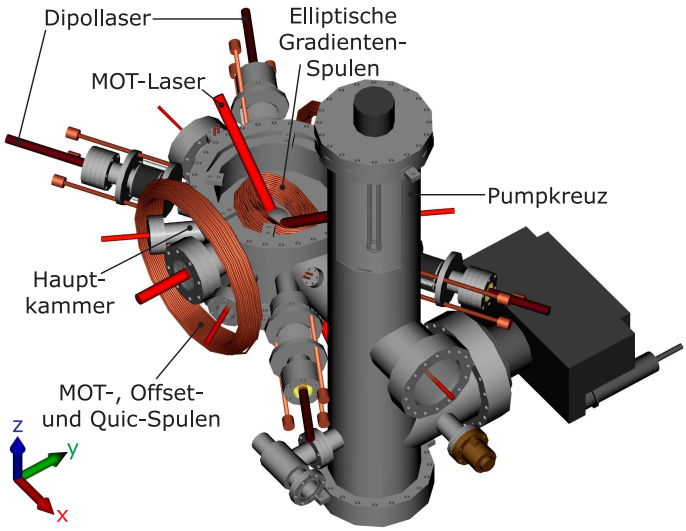

Abb. F.3: Eine CAD-Simulation der Vakuumkammer. Links auf dem Bild befindet sich die Hauptkammer, in der die Experimente stattfinden. Das Pumpkreuz mit den daran befestigten Pumpen dient zur Erzeugung des Ultrahochvakuums.

Deshalb müssen vier der sechs MOT-Strahlen aus der Hauptebene (x–y) herausgenommen werden (normalerweise nur zwei). Deshalb werden bei den optischen Zugängen ober- und unterhalb der Kammer große Fenster entlang der x-Achse benötigt. Gleichzeitig müssen an diesen Fenstern die Spulen zur Erzeugung des magnetischen Gradienten angebracht werden. Da diese Spulen entlang der y-Achse ziehen, müssen sie sich in dieser Richtung nah am Kammerzentrum befinden. Deshalb wurden elliptische Spulen gewickelt und an den elliptischen Fenstern angebracht.

Berechnungen

Es wurden Berechnungen zur Einzelphotonendetektion und zur elektromagnetisch induzierten Transparenz durchgeführt. Die Rechnungen zur Einzelphotonendektion zeigten, dass die Detektionseffizienz von Einzelphotonen bei über 99.9 % liegt. Wenn kein Photon ankommt liegt die Wahrscheinlichkeit auch keines zu detektieren bei 99.3 %.

Die Rechnungen zur elektromangetisch induzierten Transparenz zeigten, dass es theoretisch möglich ist, Linienbreiten von 25.5 Hz zu messen. Allerdings benötigt man dazu eine Atomwolke, deren Dichte die bisher erzeugte übersteigt.

Experimentelle Ergebnisse

Magneto-optische Falle und dunkle MOT

Für die die magneto-optische Falle wurden Laserstrahlen mit einer Leistung von 20 mW auf dem MOT-Übergang und 1 mW auf dem Rückpumpübergang verwendet. Dabei wurde ein magnetischer Gradient mit $\sim 11.9\,\mathrm{G/cm}$ angelegt und es konnten bis zu $1.7 \cdot 10^9$ Atome bei Temperaturen um $400\,\mu\mathrm{K}$ gefangen werden.

Da die Atome in der MOT zu heiß waren, um in die Dipolfalle umgeladen zu werden, wurden sie mit einer dunklen MOT weiter gekühlt. Dabei werden die MOT-Laser für eine Dauer von 17 ms 100 MHz rot verstimmt und die Leistung des Rückpumpers auf 1 % reduziert. Dadurch streuen die Atome weniger Licht und kühlen ab, wobei allerdings auch ein Großteil der Atome verloren geht. Um diesen Verlust zu reduzieren wurde der Magnetfeldgradient auf 16.9 G/cm erhöht.

Die Atomzahl reduzierte sich auf $9.3 \cdot 10^8$ und die Dichte auf $n_0 = 1.4 \cdot 10^{12}\,\mathrm{cm}^{-3}$. Die Temperatur wurde dabei auf $T_x = 40\,\mu\mathrm{K}$ bzw. $T_z = 37\,\mu\mathrm{K}$ reduziert, wobei die gemessene Ausdehnung der Wolke $\sigma_x = 400\,\mu\mathrm{m}$ und $\sigma_z = 260\,\mu\mathrm{m}$ betrug.

Dipolfalle

Die Daten über die Dipolfalle wurden mit Fluoreszenzmessungen gewonnen. Hierbei wurden $3.4 \cdot 10^7$ Atome detektiert. Da in beiden Richtungen unterschiedliche Temperaturen von $T_x = 200\,\mu\mathrm{K}$ und $T_z = 80\,\mu\mathrm{K}$ gemessen wurden, befindet sich die Dipolfalle aufgrund zu weniger Stöße nach der Thermalasierungszeit von 30 ms nicht im thermischen Gleichgewicht. Die gemessene Dichte betrug $n_0 = 2.3 \cdot 10^{11}\,\mathrm{cm}^{-3}$ und die Ausdehnung $\sigma_x = 272\,\mu\mathrm{m}$ bzw. $\sigma_z = 126\,\mu\mathrm{m}$.
Dabei wurden Lebensdauern von $\tau_B = 630\,\mathrm{ms}$ in der Einstrahlfalle und $\tau_{CB} = 770\,\mathrm{ms}$ in der Zweistrahlfalle gemessen. Eine Fluoreszenzaufnahme der Dipolfalle ist in Abbildung 11.2 dargestellt.

Absorbtionsmessungen

Bei den Absorbtionsmessungen wird der Probelaser durch die Wolke geschossen und dahinter mit einer Kamera detektiert. Dabei wird gemessen, wie viel Licht

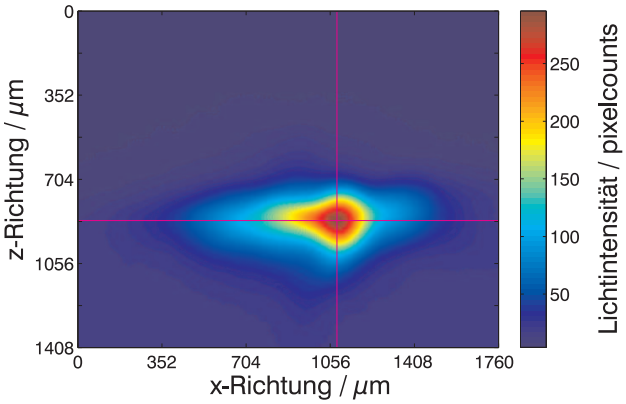

Abb. F.4: Fluoreszenzaufnahme der Wolke mit $1.7 \cdot 10^7$ Atomen in der Dipolfalle.

die Wolke aus dem Strahl absorbiert hat.
Mit dieser Methode wurde die Starkverschiebung durch die Dipolfalle gemessen: durch den ac-Starkeffekt verschiebt sich die Resonanz der Atome in der Dipolfalle in Abhängigkeit von Laserleistung. Damit konnte der Radius des Dipollasers im Fokus zu $w_0 = 28.7 \pm 0.7\,\mu$m bestimmt werden. Da urspünglich mit einem Radius von $35\,\mu$m geplant wurde, übertrifft dieses Ergebnis die Erwartungen.

Mit dem magnetischen Offsetfeld von 118.7 G wurden die Resonanzen der einzelnen Übergänge verschoben, so dass die Atome eines einzelnen Unterzustandes angesprochen werden können. Abbildung F.5 zeigt diese Messung.

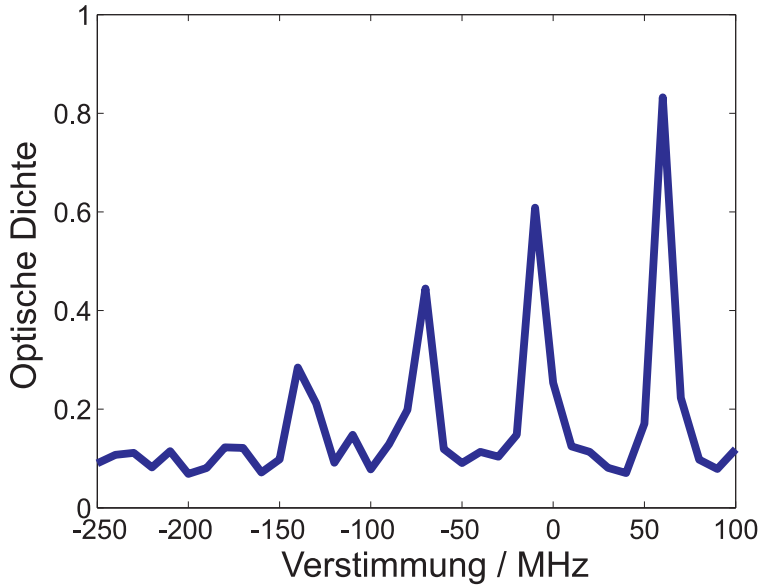

Abb. F.5: Absorbtionsspektrum von optisch gefangenen Atomen bei einem Offsetfeld von 118.7 G. Vier adressierte Unterzustände können erkannt werden.

Elektromagnetisch induzierte Transparenz

Der Peak um $-20\,\mathrm{MHz}$, welcher dem $|5S_{1/2}, F = 2, m_F = -1\rangle$–$|5P_{1/2}, F = 2, m_F = 0\rangle$-Übergang entspricht, wurde nun für die Messungen zur elektromagnetisch induzierten Transparenz verwendet. Hierbei wurde das Magnetfeld leicht auf 129.7 G erhöht.
Die Messungen wurden mit $\tau = 5\mu$s, $\tau = 20\mu$s und $\tau = 100\mu$s langen (annähernd gaussförmigen) Pulsen durchgeführt. Um sowohl die absorbtiven als auch die dispersiven Eigenschaften der Wolke gleichzeitg zu messen wurde dem σ^+-polarisierten Probestrahl ein kleiner Anteil σ^--polarisiertes Licht beigemischt. Abbildung F.6 zeigt den EIT-peak einer Messung mit $20\,\mu$s Pulslänge und einer Koppellaser-Rabifrequenz von 1200 kHz. Bei dieser Messung kann erkannt werden, dass das Signal sowohl über absorbtive (der Peak selbst) also auch dispersive (die Asymmetrie) Komponenten verfügt.

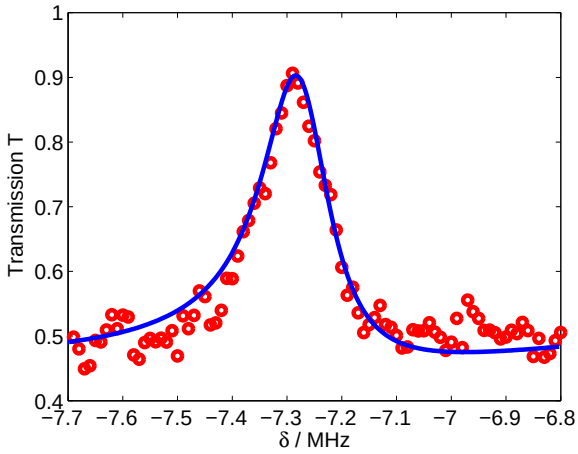

Abb. F.6: Transmissionsspektrum eines $20\,\mu$s Pulses bei einer Koppellaser-Rabifrequenz von 1200 kHz. Sowohl der absorbtive als auch der dispersive Anteil können erkannt werden. Der Frequenzoffset von $\delta_0 = -7.27\,\mathrm{MHz}$ entspricht der differentiellen Zeemanverschiebung durch das Magnetfeld. Da dieser Offset nur vom Magnetfeld abhängt kann er benutzt werden um es zu kalibirieren.

Die schmalste Linie konnte mit einem $100\,\mu$s-Puls gemessen werden. Hierbei wurde eine Koppellaser-Rabifrequenz von 360 kHz verwendet. Hierbei ist die Transparenz so niedrig, dass der absorbtive Teil nicht mehr erkannt werden kann. Diese Messung ist in Abbildung F.7 dargestellt.

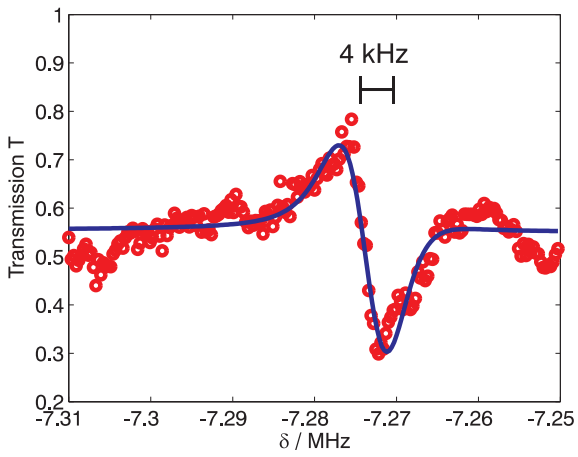

Abb. F.7: EIT Messung mit einem 100 μs Puls: die Linienbreite wurde auf 4 kHz reduziert. Die Transparenz ist so gering, dass nur der dispersive Anteil des Signals erkannt werden kann.

Mit einer gaussförmigen $1/e$-Breite von 4 kHz ist das die bisher schmalste Linie, die bislang in ultrakalten Atomen gemessen wurde. Die damit verbundene Lichtgeschwindigkeit wurde zu $v_{gr} = 1.7\,\mathrm{m/s}$ bestimmt.

Bibliography

[Ada06] Charles Adams. private communication, 2006.

[ADR82] Alain Aspect, Jean Dalibard, and Gérard Roger. Experimental Test of Bell's Inequalities Using Time- Varying Analyzers. *Phys. Rev. Lett.*, **49**(25), 1804–1807, Dec 1982.

[AT55] S. H. Autler and C. H. Townes. Stark Effect in Rapidly Varying Fields. *Physical Review*, **100**(2), 703–722, Oct 1955.

[BBG+04] Danielle A. Braje, Vlatko Balic, Sunil Goda, G. Y. Yin, and S. E. Harris. Frequency Mixing Using Electromagnetically Induced Transparency in Cold Atoms. *Physical Review Letters*, **93**(18), 183601, 2004.

[BEKW02] A. Beige, B.-G. Englert, C. Kurtsiefer, and H. Weinfurter. Secure communication with single-photon two-qubit states. *Journal of Physics A*, **35**(28), L407–L413, Jul 2002.

[BHN07] Bernhard Halle Nachfolger. Optische Werkstätten, Berlin, http://www.b-halle.de, 2007.

[BJL+02] Keith Burnett, Paul S. Julienne, Paul D. Lett, Eite Tiesinga, and Carl J. Williams. Quantum encouters of the cold kind. *Nature*, **416**, 225–232, Mar 2002.

[BMV96] H. M. J. M. Boesten, A. J. Moerdijk, and B. J. Verhaar. Dipolar decay in two recent Bose-Einstein condensation experiments. *Physical Review A*, **54**(1), R29–R32, Jul 1996.

[BNWM97] S. Brandt, A. Nagel, R. Wynands, and D. Meschede. Buffer-gas-induced linewidth reduction of coherent dark resonances to below 50 Hz. *Physical Review A*, **56**(2), R1063–R1066, Aug 1997.

[BR31] G. Breit and I. I. Rabi. Measurement of Nuclear Spin. *Physical Review*, **38**(11), 2082–2083, Dec 1931.

[BTS98] K. Bergmann, H. Theuer, and B. W. Shore. Coherent population transfer among quantum states of atoms and molecules. *Review of Modern Physics*, **70**(3), 1003–1025, Jul 1998.

[CAB+68] J. P. Carrico, A. Adler, M. R. Baker, S. Legowski, E. Lipworth, P. G. H. Sandars, T. S. Stein, and M. C. Weisskopf. Atomic-Beam Resonance Measurement of the Differential Polarizability between Zeeman Substates in the Ground State of the Cesium Atom. *Physical Review*, **170**(1), 64–76, Jun 1968.

[CBAC86] Steven Chu, J. E. Bjorkholm, A. Ashkin, and A. Cable. Experimental Observation of Optically Trapped Atoms. *Physical Review Letters*, **57**(3), 314–317, Jul 1986.

[CMJ+06] T. Chaneliere, D. N. Matsukevich, S. D. Jenkins, T. A. B. Kennedy, M. S. Chapman, and A. Kuzmich. Quantum Telecommunication Based on Atomic Cascade Transitions. *Physical Review Letters*, **96**(9), 093604, 2006.

[CRGW03] G. Cennini, G. Ritt, C. Geckeler, and M. Weitz. Bose-Einstein condensation in a CO_2-laser optical dipole trap. *Applied Physics B*, **77**, 773–779, Nov 2003.

[DAK+05] I. Dotsenko, W. Alt, M. Khudaverdyan, S. Kuhr, D. Meschede, Y. Miroshnychenko, D. Schrader, and A. Rauschenbeutel. Submicrometer Position Control of Single Trapped Neutral Atoms. *Physical Review Letters*, **95**(3), 033002, 2005.

[Dic54] R. H. Dicke. Coherence in Spontaneous Radiation Processes. *Physical Review*, **93**(1), 99, Jan 1954.

[EBH98] Tilman Esslinger, Immanuel Bloch, and Theodor W. Hänsch. Bose-Einstein condensation in a quadrupole-Ioffe-configuration trap. *Physical Review A*, **58**(4), R2664–R2667, Oct 1998.

[ENH00] Michael Erhard, Stefan Nußmann, and Hanspeter Helm. Power broadening and Doppler effects of coherent dark resonances in Rb. *Physical Review A*, **62**(6), 061802, Nov 2000.

[FGHZ98] J. Fortagh, A. Grossmann, T. W. Hansch, and C. Zimmermann. Fast loading of a magneto-optical trap from a pulsed thermal source. *Journal of Applied Physics*, **84**(12), 6499–6501, 1998.

[FIM05] Michael Fleischhauer, Atac Imamoglu, and Jonathan P. Marangos. Electromagnetically induced transparency: Optics in coherent media. *Review of Modern Physics*, **77**(2), 633–673, Jul 2005.

[FL00] M. Fleischhauer and M. D. Lukin. Dark State Polaritons in Electromagnetically Induced Transparency. *Physical Review Letters*, **84**(22), 5094–5097, May 2000.

[FL02] M. Fleischhauer and M. D. Lukin. Quantum memory for photons: Dark-state polaritons. *Physical Review A*, **65**(2), 022314, Jan 2002.

[FSB97] M. P. Fewell, B. W. Shore, and K. Bergmann. Coherent Population Transfer among Three States: Full Algebraic Solutions and the Relevance of Non Adiabatic Processes to Transfer by Delayed Pulses. *Australian Journal of Physics*, **50**, 281–308, November 1997.

[FYL00] M. Fleischhauer, S. F. Yelin, and M. D. Lukin. How to trap photons? Storing single-photon quantum states in collective atomic excitations. *Optics Communications*, **179**, 395–410, May 2000.

[GP03] A. Grabowski and T. Pfau. A lattice of magneto-optical and magnetic traps for cold atoms. *The European Physical Journal D*, **22**, 347–354, 2003.

[GRSB90] U. Gaubatz, P. Rudecki, S. Schiemann, and K. Bergmann. Population transfer between molecular vibrational levels by stimulated Raman scattering with partially overlapping laser fields. A new concept and experimental results. *The Journal of Chemical Physics*, **92**(9), 5363–5376, 1990.

[GWO00] Rudolf Grimm, Matthias Weidemüller, and Yurii B. Ovchinnikov. Optical dipole traps for neutral atoms. *Advances in Atomic, Molecular and Optical Physics*, **42**, 95–170, 2000.

[Hen04] Carsten Henkel. private communication, 2004.

[HFI90] S. E. Harris, J. E. Field, and A. Imamoglu. Nonlinear optical processes using electromagnetically induced transparency. *Physical Review Letters*, **64**(10), 1107–1110, Mar 1990.

[HHDB99] L. V. Hau, S. E. Harris, Z. Dutton, and C. H. Behroozi. Light speed reduction to 17 metres per second in an ultracold atomic gas. *Nature*, **397**, 594–598, Feb 1999.

[Ima02] A. Imamoglu. High Efficiency Photon Counting Using Stored Light. *Physical Review Letters*, **89**(16), 163602, Sep 2002.

[JK02] Daniel F. V. James and Paul G. Kwiat. Atomic-Vapor-Based High Efficiency Optical Detectors with Photon Number Resolution. *Physical Review Letters*, **89**(18), 183601, Oct 2002.

[KC92] Mark Kasevich and Steven Chu. Laser cooling below a photon recoil with three-level atoms. *Physical Review Letters*, **69**(12), 1741–1744, Sep 1992.

[KDSK99] W. Ketterle, D.S. Durfee, and D.M. Stamper-Kurn. Making, probing and understanding Bose-Einstein condensates. *In Bose-Einstein condensation in atomic gases, Proceedings of the International School of Physics "Enrico Fermi", Course CXL, edited by M. Inguscio, S. Stringari and C.E. Wieman*, , 67–176, 1999.

[KGHB89] J. R. Kuklinski, U. Gaubatz, F. T. Hioe, and K. Bergmann. Adiabatic population transfer in a three-level system driven by delayed laser pulses. *Physical Review A*, **40**(11), 6741–6744, Dec 1989.

[KHBR99] A. Kuhn, M. Hennrich, T. Bondo, and G. Rempe. Controlled generation of single photons from a strongly coupled atom-cavity system. *Applied Physics B*, **69**, 373–377, Oct 1999.

[KLM01] E. Knill, R. Laflamme, and G. J. Milburn. A scheme for effiecient quantum computation with linear optics. *Nature*, **109**, 46–52, Jan 2001.

[KW06] Leon Karpa and Martin Weitz. A Stern-Gerlach experiment for slow light. *Nature Physics*, **2**, 332–335, May 2006.

[LDBH01] Chien Liu, Zachary Dutton, Cyrus H. Behroozi, and Lene Vestergard Hau. Observation of coherent optical information storage in an atomic medium using halted light pulses. *Nature*, **409**, 490–493, Jan 2001.

[LRW96] O. J. Luiten, M. W. Reynolds, and J. T. M. Walraven. Kinetic theory of the evaporative cooling of a trapped gas. *Physical Review A*, **53**(1), 381–389, Jan 1996.

[LS64] E. Lipworth and P. G. H. Sandars. Removal of Zeeman-Level Degeneracy in alkali atoms by an electric field. *Physical Review Letters*, **13**(24), 716–717, Dec 1964.

[Mar03] Andreas Marte. Feshbach-Resonanzen bei Stößen ultrakalter Rubidiumatome. Dissertation, Technische Universität München, Jul 2003.

[MAvD+96] M.-O. Mewes, M. R. Andrews, N. J. van Druten, D. M. Kurn, D. S. Durfee, and W. Ketterle. Bose-Einstein Condensation in a Tightly Confining dc Magnetic Trap. *Physical Review Letters*, **77**(3), 416–419, Jul 1996.

[MKB+00] P. Michler, A. Kiraz, C. Becher, W. V. Schoenfeld, P. M. Petroff, Lidong Zhang, E. Hu, and A. Imamoglu. A Quantum Dot Single-Photon Turnstile Device. *Science*, **290**, 2282–2285, Dec 2000.

[Mow72] J. Richard Mowat. Stark Effect in Alkali-Metal Ground-State Hyperfine Structure. *Physical Review A*, **5**(3), 1059–1062, Mar 1972.

[MSK+03] Y. Miroshnychenko, D. Schrader, S. Kuhr, W. Alt, I. Dotsenko, M. Khudaverdyan, A. Rauschenbeutel, and D. Meschede. Continued imaging of the transport of a single neutral atom. *Optics Express*, **11**(25), 3498–3502, Dec 2003.

[MvdS99] Harold J. Metcalf and Peter van der Straten. *Laser Cooling and Trapping*. Springer, 1999.

[NIST07] NIST, National Institute of Standarts and Technology. http://www.physics.nist.gov/cuu/Constants/index.html, 2007.

[NK94] A. Noble and M. Kasevich. UHV optical window seal to conflat knife edge. *Review of Scientific Instruments*, **65**(9), 3042–3043, 1994.

[OGGT01] K. M. O'Hara, M. E. Gehm, S. R. Granade, and J. E. Thomas. Scaling laws for evaporative cooling in time-dependent optical traps. *Physical Review A*, **64**(5), 051403, Oct 2001.

[OHE84] J. Oreg, F. T. Hioe, and J. H. Eberly. Adiabatic following in multilevel systems. *Physical Review A*, **29**(2), 690–697, Feb 1984.

[PAH06] Graham T. Purves, Charles S. Adams, and Ifan G. Hughes. Sagnac interferometry in a slow-light medium. *Physical Review A*, **74**(2), 023805, 2006.

[Pet05] Achim Peters. private communication, 2005.

[PFL+03] T. Petelski, M. Fattori, G. Lamporesi, J. Stuhler, and G.M. Tino. Doppler-free spectroscopy using magnetically induced dichroism of atomic vapor: a new scheme for laser frequency locking. *European Physics Journal D*, **21**, 279–283, Jan 2003.

[Pri83] David E. Pritchard. Cooling Neutral Atoms in a Magnetic Trap for Precision Spectroscopy. *Physical Review Letters*, **51**(15), 1336–1339, Oct 1983.

[RKLK81] Jan R. Rubbmark, Michael M. Kash, Michael G. Littman, and Daniel Kleppner. Dynamical effects at avoided level crossings: A study of the Landau-Zener effect using Rydberg atoms. *Physical Review A*, **23**(6), 3107–3117, Jun 1981.

[RPC+87] E. L. Raab, M. Prentiss, Alex Cable, Steven Chu, and D. E. Pritchard. Trapping of Neutral Sodium Atoms with Radiation Pressure. *Physical Review Letters*, **59**(23), 2631–2634, Dec 1987.

[San67] P. G. H. Sandars. Differential Polarizability in the ground state of the hydrogen atom. *Proceedings of the Physical Society (London)*, **92**(4), 857–861, Dec 1967.

[Sch01] Wolfgang P. Schleich. *Quantum Optics in Phase Space*. Wiley VCH, 2001.

[SGOD+99] J. Söding, D. Guéry-Odelin, P. Desbiolles, F. Chevy, H. Inamori, and J. Dalibard. Three-body decay of a rubidium Bose-Einstein condensate. *Applied Physics B*, **69**(4), 257–261, Sep 1999.

[Ste02] Daniel A. Steck. Rubidium 87 D Line Data. *published online*, **revision 0.7**, Nov 2002.

[Sut97] Dieter Suter. *The Physics of Laser-Atom Interactions*. Cambridge University Press, 1997.

[SZ97] Marlan O. Scully and Muhammad S. Zubairy. *Quantum Optics*. Cambridge University Press, 1997.

[TIL03] J. M. Taylor, A. Imamoglu, and M. D. Lukin. Controlling a Mesoscopic Spin Environment by Quantum Bit Manipulation. *Physical Review Letters*, **91**(24), 246802, Dec 2003.

[WVS+06] M. Weber, J. Volz, K. Saucke, C. Kurtsiefer, and H. Weinfurter. Analysis of a single-atom dipole trap. *Physical Review A*, **73**, 043406, Apr 2006.

[XLJGB95] Min Xiao, Yong-qing Li, Shao-zheng Jin, and Julio Gea-Banacloche. Measurement of Dispersive Properties of Electromagnetically Induced Transparency in Rubidium Atoms. *Physical Review Letters*, **74**(5), 666–669, Jan 1995.

[Zim05] Claus Zimmermann. Nichtlineare Optik mit Wellen und Teilchen. Scriptum, Jan 2005.

Acknowledgements

Here I want to thank all the people who contributed their part to this thesis:

I want to thank

- Prof. Tilman Pfau for taking me as a PhD student at his chair and giving me the chance to develop and setup this experiment.
- Prof. Dr. Atac Imamoğlu, who had the initial idea for this experiment, for taking me as a PhD student and for always supporting us with his knowledge on theoretical quantum optics.
- Dr. Jürgen Stuhler for sharing his knowledge on atom optics with me, his help on the experimental setup and for proofreading this thesis.
- Harald Kübler for setting up this experiment with me, for solving all electronical problems and for proofreading this thesis.
- Andreas Chromik for setting up this experiment with us.
- Alex Batär for his help on setting up the IGBT board.
- Robert Löw for fruitful discussions on theoretical quantum optics and for proofreading this thesis.
- Tim van Boxtel for ensuring the proper english used in this thesis.
- our Hiwis Stefan Müller, Beni Krauss, Michael Brett and Jorge Jil for their help on setting up this experiment.
- all other group members for their help on the innumerable problems and for the nice ambience.
- Prof. Dr. Günther Wunner for being the chairman of my PhD exam
- our mechanical, electronics and glass workshops for their support
- all my friends for the time they spent with me outside the lab.